High Performance Friction-Type Bearings for Seismic Isolation

Tianye Yang

A dissertation
submitted in partial fulfillment of the
requirements for the degree of

Doctor of Philosophy

University of Washington

2020

Reading Committee:

Paolo M. Calvi, Chair

Richard Wiebe

Jeffrey W. Berman

Marc O. Eberhard

Program Authorized to Offer Degree:
Department of Civil and Environmental Engineering

University of Washington

Abstract

High Performance Friction-Type Bearings for Seismic Isolation

Tianye Yang

Chair of the Supervisory Committee:
Paolo M. Calvi
Civil and Environmental Engineering

Seismic isolation is effective in protecting both structural and non-structural elements during earthquakes. One of the most commonly used base-isolation systems is the friction pendulum system (FPS). It provides excellent re-centering and large energy dissipation capacities. Despite these benefits, FPSs are rarely used in the U.S. for several reasons. Out of many one may identify, the required peer review process and the conservativeness of the existing design guideline make the implementation of the technology somewhat less economically appealing. More critically, it is a well-known dilemma that FPS can only be designed to achieve optimal performance for one level of ground shaking. A possible answer to this challenge is to use "passive-adaptive" devices, including multiple friction pendulum systems and the recently proposed Variable Friction Systems (VFSs). While providing sufficient protection (usually life safety) during a maximum considered earthquake, these systems can still effectively isolate the structure during a service level earthquake, resulting in lower seismic demands on the supported structure and its non-structural components compared to a fixed-based building. However, the development of VFSs is still in early stage, and the performance of structures isolated with such systems is uncertain.

Another recently identified challenge in designing isolation systems is the potential for large magnitude and long period earthquakes, in particular, the magnitude-9 (M9) earthquake in Cascadia Subduction Zone. The results obtained from recent numerical simulations

indicated that this type of earthquake may be particularly detrimental for structures with fundamental periods of vibration of 1.0 second or larger. This finding may be particularly relevant for base-isolated structures, which tend to be characterized by large effective periods. However, such systems have not been included in the studies conducted thus far, and the effect of the simulated M9 earthquake on their performance remains unclear.

To address the aforementioned knowledge gaps that are limiting the implementation of friction-type seismic isolation systems, this dissertation aims to: (i) develop an analysis, modeling, and design framework for structures isolated with VFSs; and (ii) evaluate how ground motions with different characteristics impact the performance and analysis of friction-type seismic isolation systems.

TABLE OF CONTENTS

Page

LIST OF FIGURES

LIST OF TABLES

ACKNOWLEDGMENTS

I would like to express my sincere gratitude to my advisor Professor Paolo Calvi and co-advisor Professor Richard Wiebe for their advice and support through the past four years at the University of Washington. Their enthusiasm and diligence towards research have inspired me since the very beginning. I would also like to thank Professor Jeffrey Berman and Professor Marc Eberhard for providing their advice on the M9 study, and their contributions as members of my dissertation committee.

I appreciate the lab technicians at the Laboratory of EUCENTRE Foundation in Pavia (Italy), who tested the prototypes of Variable Friction Systems.

I would like to pay my special regards to Andrew Sen, who helped me tremendously with OpenSees, and Nasser Marafi, who introduced me to the world of seismology. I would also like to thank my friends and colleagues throughout my Ph.D. program. Thanks for always being there with me. Of the many, I will call out Kristina Tsvetanova, Ashley Heid, Shen Ren, Yujie Zhou, Leikune Aragaw, Kamal Ahmed, Sarah Wichman, Tom Lin, Andrew Winter, Eleonora Bruschi, and Sarah Bergquist.

This research would not have been possible without the financial support from the University of Washington Royalty Research Fund (RRF) and the Seismology and Earthquake Engineering Research Infrastructure Alliance for Europe (SERA).

DEDICATION

To my partner, *Eben*
who has provided immense love and support.

To my grandparents, *Suxian* and *Shukui*
who helped to raise me and gave me a lifetime worth of inspiration.

To my parents, *Yuhong* and *Lei*
who have been the role models of my life.

Chapter 1

INTRODUCTION

1.1 Base Isolation concepts

Seismic isolation protects both structural and non-structural elements during earthquakes. As shown in Figure 1.1, seismic isolators decouple the superstructure from the ground, using flexible devices (i.e., isolators), so that the total energy transmitted from the ground to the superstructure is reduced, leading to reduced interstory drift and force demand in the superstructure.

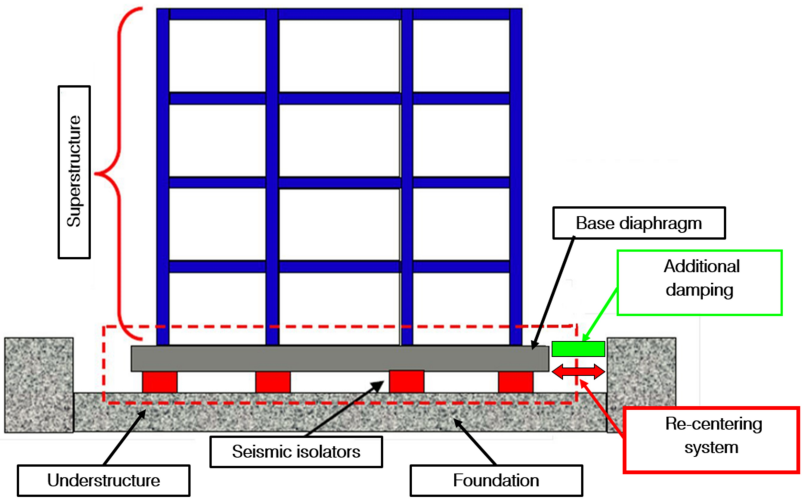

Figure 1.1: Schematic drawing of a base isolated building

First proposed by a commission formed after the severe 1908 earthquake in the Italian region of Messina-Reggio, and first implemented into practice in 1969 for an elementary school in Skopje, Yugoslavia [Kelly, 1986], base isolation has been studied by numerous researchers and has been applied in practice for decades.

There are three basic elements that are common to most seismic isolation systems:

1. A flexible layer between the foundation and the base diaphragm of the superstructure: This shifts the fundamental period of the whole system to longer periods where the acceleration response is reduced. However, this increase in flexibility also increases the displacement demand, mainly concentrated at the isolation layer.

2. Damping: In a seismic isolation system, damping is usually provided by either inherent hysteretic damping from the isolators themselves (for example, lead-rubber bearings and Friction Pendulum Systems), or additional dampers (for example, viscous hydraulic damping). The principles of how the first two basic elements work are illustrated in Figure 1.2, where the blue curves represent the typical 5% damped acceleration and displacement spectra, and the yellow curves represent the acceleration and displacement spectra with additional damping, which either comes from hysteretic damping of the isolation system, or from added damping systems.

3. Large stiffness under service loading: The isolation layer typically incorporates mechanisms to provide rigidity of the building under small horizontal loads, such as wind load. For example, lead-rubber bearings provide the desired rigidity under low loads by their high initial (elastic) stiffness from the lead cores [Buckle and Mayes, 1990], while friction-type bearings do not activate until the friction force threshold is reached.

Another important aspect of seismic isolation is the change of the fundamental mode shape. The closer the fundamental mode shape is to rigid-body motion, the lower the participation of higher modes. As the natural period of the whole isolation system increases relative to the natural period of the superstructure, the participation of higher modes becomes very small and the deformation is concentrated mainly at the isolation layer [Morgan and Mahin, 2011].

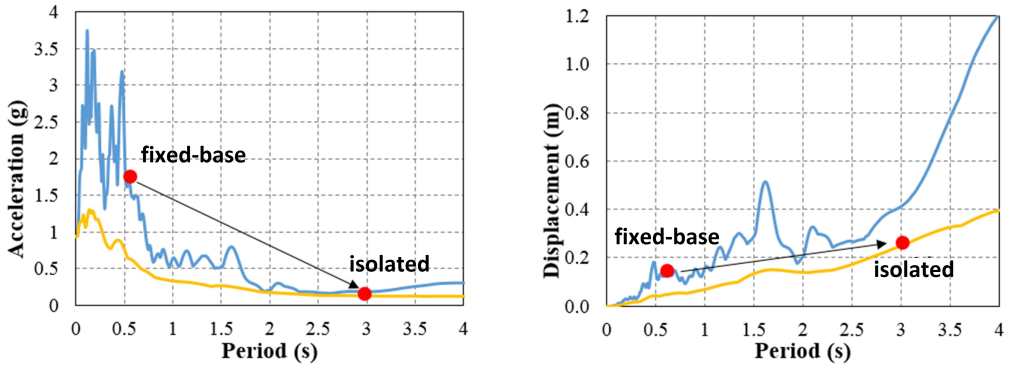

Figure 1.2: Acceleration and displacement spectrum changes from fixed-base buildings to isolated buildings

1.2 Base Isolation Systems

While a variety of seismic isolation systems have been proposed, they are mostly classified into two types [Naeim and Kelly, 1999]: elastomeric bearings and friction-type bearings. Several review articles have outlined the theory, development, and application of seismic isolation. Kelly [1986] provided a thorough review on the historical development of seismic isolation in a chronological manner up to 1986. Buckle and Mayes [1990] provided an exhaustive list of the early applications of such technology around the world up to 1990. Since then, the amount of attention that this technology received has grown exponentially given its superior behavior compared to fixed-base buildings. Warn and Ryan [2012] summarized the current practice and development of modern seismic isolation technology, particularly the ones in the United States. Calvi and Calvi [2018] focused on the progression of friction-based seismic isolation systems. They also provided reviews on recent research efforts focused on addressing the open problems listed in Warn and Ryan [2012], including the response to vertical actions, uplift issues, and residual displacements.

While detailed development and practical implementation of seismic isolation can be found in the review articles listed above, the behavior of the common elastomeric bearings and friction-type bearings are summarized here.

As shown in Figure 1.3, elastomeric bearings typically consist of vulcanization bonding of sheets of rubber pads and steel shims. Both low damping natural or synthetic rubber and high damping rubber have been used in elastomeric bearings. For low damping rubber, supplemental damping devices, such as yielding steel bars, or viscous fluid dampers are usually used to limit the total displacement [Warn and Ryan, 2012]. Oftentimes a lead-plug is placed in the center of the bearing (as shown in Figure 1.3 (b)) to provide additional dissipation and initial stiffness. However, extra damping devices have been found to produce high-frequency response and produce accelerations in the superstructure [Kelly, 1986]. The development of high inherent damping natural rubbers to eliminate the need to use supplemental damping devices was achieved in 1982 [Derham et al., 1985]. One serendipitous advantage of high damping rubber bearing system is that it provides a degree of ambient vibration reduction [Naeim and Kelly, 1999]. In general, for elastomeric bearings to maintain stability under large lateral displacements, relatively large bearing diameters are needed. However, with the increase in the size of the bearing, the stiffness of the bearing also increases, which makes it a less attractive strategy for isolating light structures. In contrast, the behavior of friction-type bearings is independent of axial load.

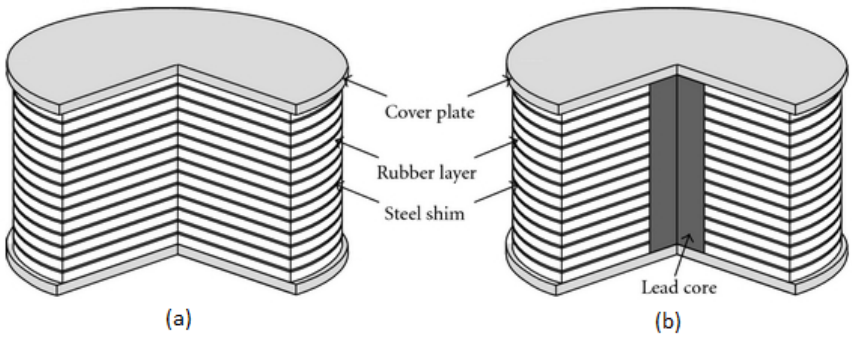

Figure 1.3: Illustration of (a) multilayer elaastomeric bearing; (b) lead-plug rubber bearing. Retrieved from https://www.hindawi.com/archive/2011/861451/fig1/ on Oct. 5th, 2018

Friction-type bearings are categorized into two types: flat sliding bearings and pendulum bearings. Flat sliding bearings are often used in combination with elastomeric bearings due

to the lack of a restoring mechanism. However, it was not until the development of the friction pendulum system (FPS) [Zayas et al., 1987] that friction-type bearings became a competitive alternative to elastomeric bearings. As shown in Figure 1.4, the FPS consists of a articulated slider coated with low friction material (usually derived from polytetrafluoroethylene (PTFE)) supported on a concave sliding surface. Before sliding occurs, the isolation system acts as a rigid link, thus providing high initial stiffness. The friction force between the sliding surface and the slider provides energy dissipation when sliding occurs, while the spherical concave sliding surface provides a restoring force utilizing the gravity of the superstructure itself.

A number of variations of the FPS have been proposed during the past decade in the pursuit of alternative systems capable of achieving advanced multi-performance objectives. Examples of such systems include: multiple friction pendulums, which are double concave friction pendulum system (DCFP) [Fenz and Constantinou, 2006], triple friction pendulum (TFP) [Fenz and Constantinou, 2008d], [Fenz and Constantinou, 2008c], [Becker and Mahin, 2012], and quintuple friction pendulum [Tsai et al., 2010], [Lee and Constantinou, 2016]; variable frequency pendulum isolators (achieved by using a non-spherical sliding surface) [Murnal and Sinha, 2004], [Panchal and Jangid, 2008a]; and uplift restraining systems [Roussis and Constantinou, 2006b], [Roussis and Constantinou, 2006a]. While all the aforementioned systems provide superior behaviors in certain aspects, some are very difficult to manufacture. In practice, the most widely used friction-type bearings are FPS, DCFP, and TFP.

Despite the benefits that friction-type base isolation technologies can offer, they are rarely used in the U.S., for several reasons. Out of many one may identify, the required peer review process and the conservativeness of the existing design guideline make the implementation of the technology less economically appealing. More critically, it is a well-known dilemma that standard friction pendulum systems can only be designed to achieve optimal performance for one level of ground shaking [Fenz and Constantinou, 2008d]. Devices designed for a given seismic event may not be adequate to protect the structure in case of more intense earthquakes, and may suffer catastrophic failures in case the displacement demand that

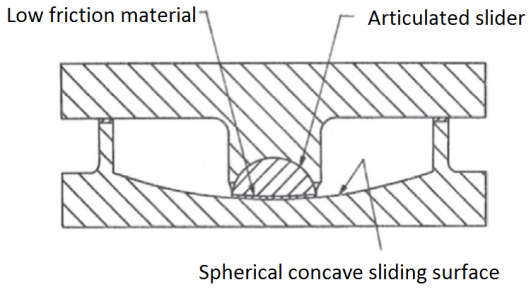

Figure 1.4: Schematic drawing of Friction Pendulum System

exceeds the capacity of the system. Conversely, designing the system for a rare intense event, results in non-optimal performance in low-intensity earthquakes.

A possible answer to this challenge that has been recently identified is to use "passive-adaptive" device. In this context, "passive-adaptive" refers to systems whereby the stiffness, the effective friction, and the damping properties change at designed levels of lateral displacement. The primary benefit of this type of response is that isolation systems can be designed to optimize multiple performance objectives and/or for multiple levels of ground shaking. To this end, most of the current efforts have focused on the use of multiple friction pendulum systems, in which the frictional and geometrical properties of each surface can be controlled independently to achieve the desired multi-stage response. A literature review on the development of multiple friction pendulum systems is provided in Appendix A. The general consensus is that this technology is effective at protecting structures from the effects of earthquakes of different magnitudes. However, the adaptivity increases at the expense of increased complexity in design, fabrication, and modeling. Also, recent experimental findings [Becker et al., 2017] have raised concerns, suggesting that the hardening in the response that characterizes TFP bearings may not be as beneficial as originally believed. Thus, there is a research need to develop new simplified and cost-effective adaptive base isolation systems.

Another recently identified challenge in designing isolation systems is the potential for large magnitude and long period earthquakes, in particular, the magnitude-9 (M9) earth-

quake in Cascadia Subduction Zone [Frankel et al., 2018]. The results obtained from recent numerical simulations indicated that this type of earthquakes may be particularly detrimental for structures characterized by fundamental period of vibration of 1.0 second or larger. This finding may be particularly relevant for base isolated structures, which tend to be characterized by effective period of vibration of 1.0 second or larger. However, this type of systems have not been included in the studies conducted thus far, and the effect of the M9 earthquakes on base isolated structures remain unclear.

1.3 Objectives

To address the aforementioned issues, the research herein focused on the following objectives:

Objective 1: Develop an analysis, modeling, and design framework for structures isolated with Variable Friction Systems (VFSs). This objective includes the following sub-objectives:

Obj. 1.1. Develop a three-dimensional numerical model that is capable of capturing the force-displacement behavior of VFSs.

Obj. 1.2. Implement the three-dimensional model into a structural analysis commercial software (*OpenSees*) so that researchers can further study the behavior of both VFSs and the superstructure considering complex non-linear behavior.

Obj. 1.3. Validate the numerical model with experimental evidence.

Obj. 1.4. Provide design guidelines for VFSs that exhibit adaptive behavior, namely, Adaptive Variable Friction Systems (AVFSs).

Obj. 1.5. Conduct an extensive parametric study on the performance of AVFS-isolated structures aiming to optimize the use of AVFSs as passive-adaptive device.

Obj. 1.6. Extend the application of the Variable Friction element in modeling Curved Surface Slider devices (including FPS and multiple friction pendulum systems) under severe input motions that induce displacements beyond the design displacement.

Objective 2: Evaluate how ground motions with different characteristics impact the performance and analysis of friction-type base isolation systems. This objective includes the following sub-objectives:

Obj. 2.1. Evaluate the performance of friction type base isolation systems, during an M9 earthquake, when designed based on either current code-required design spectra or modified design spectra based on previous studies.

Obj. 2.2. Evaluate the accuracy of analyzing friction type base isolation systems with a simplified method (i.e. equivalent lateral force procedure) provided by ASCE 7 [ASCE, 2017] considering different types of ground motions.

1.4 Organization

This document is organized based on the objectives described in Section 1.3. Part I of the dissertation (Chapter 2 to Chapter 4) focuses on the development, implementation, and performance of Variable Friction Systems. In particular, Chapter 2 focuses on the development and implementation in OpenSees of VFSs (*Obj. 1.1* to *Obj. 1.3*). Chapter 3 provides the design and performance of a special case of VFSs, namely, AVFSs (*Obj. 1.4* and *Obj. 1.5*). Chapter 4 explores the use of the VF element in modeling the dynamic response of Curved Surface Slider devices under severe input motions (*Obj. 1.6*). Part II of the dissertation (Chapter 5 and Chapter 6) focuses on the performance and analysis method of friction type base isolation systems during M9 motions (*Obj. 2.1* and *Obj. 2.2*, respectively). Due to the fact that each chapter focuses on different aspects of friction based isolation systems, additional corresponding background information is presented within each chapter. Conclusions are summarized in Chapter 7.

PART I: DEVELOPMENT, IMPLEMENTATION, AND PERFORMANCE OF VARIABLE FRICTION SYSTEMS

Chapter 2

DEVELOPMENT OF VARIABLE FRICTION SYSTEMS

Note: Part of this chapter is a reproduction of Yang et al. [2019a]

The main goal of this chapter is to summarize the development and implementation into OpenSees of a 3D hysteretic model that is capable of capturing the full behavior of VFSs. The newly implemented element allows researchers to perform accurate analysis and investigate these new systems in OpenSees.

This chapter first extends the background from Chapter 1 with a more detailed description of VFSs. Then it describes the 3D numerical implementation of the Variable Friction element. Thereafter, a demonstrative numerical study is provided in which both 2D and 3D case study structures, isolated by means of VFSs, are analyzed via NLTHA. Finally, some preliminary experimental results are presented in this chapter as an initial comparison to the theoretical model.

2.1 Chapter Introduction

In the context of investigating more efficient solutions, Variable Friction base isolation Systems (VFSs) (initially postulated by Panchal and Jangid [2008b]) was recently revisited by Calvi and Ruggiero [2016], Calvi et al. [2016a]. Although alternative approaches may be undertaken, these systems can be implemented in practice by treating the stainless steel sliding surface of a standard FPS to obtain a series of concentric rings characterized by different roughness values as shown in Figure 2.1 (a). This technique achieves variable friction between the low friction slider and the sliding surface, as a function of the slider's position (see Figure 2.1(b)).

The coexistence of different frictional properties within the same sliding surface, and the use of high performance low-friction materials and a convenient combination of sliding surfaces, open the door to the possibility of achieving new (potentially more advantageous) hysteretic responses. For instance, the properties of a VFS can be selected to obtain devices with a loading hysteresis that retraces that of a standard FPS while providing higher dissipation through unloading phase, and thus further reducing the displacement and acceleration demands. Alternatively, it could provide adaptive response with increasing energy dissipation as the displacement demand increases, without the need for multiple sliding surfaces (see Figure 2.1(c) hysteresis for VFS 2). The adaptive response of VFS allows engineers to design the system to satisfy multiple performance goals under different seismic hazard levels. In addition, the Variable Friction (VF) concept could be implemented into multi-spherical friction bearings to achieve more complex multi-stage behavior.

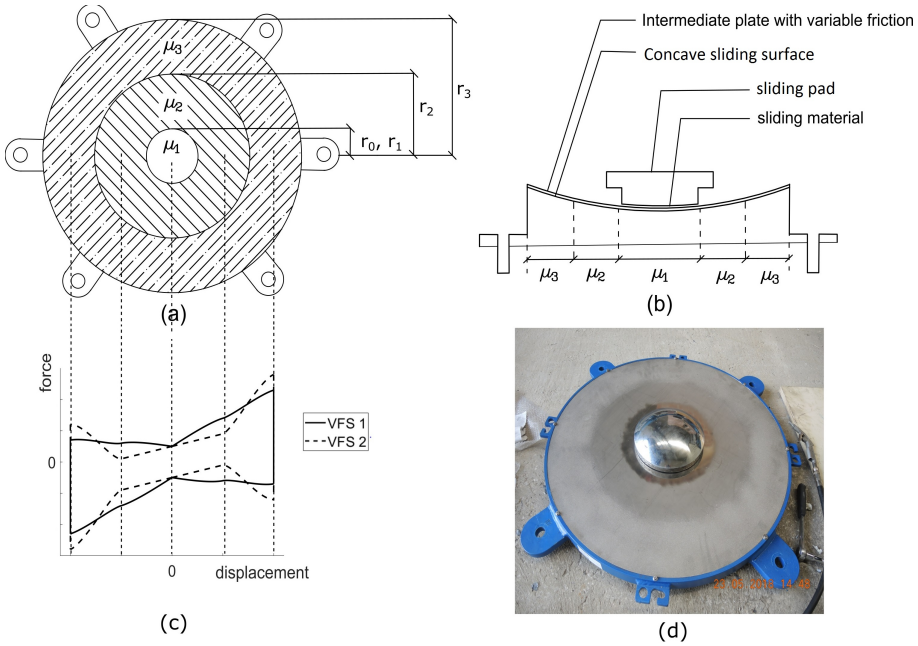

Figure 2.1: (a) Plan view of a VFS device; (b) cross section of a VFS device; (c) example hysteretic response of different VFSs; (d) VFS protocol from a full-scaled experimental test.

2.2 Theoretical Formulation

2.2.1 Analytical Model of Variable Friction System

The detailed theoretical development of the hysteretic behavior of VFSs can be found in Calvi and Ruggiero [2016] and Calvi et al. [2016a]. This section aims to provide a summary of the theoretical behavior of such systems and serve as the basis for the numerical implementation of VFSs into OpenSees software.

As introduced in Chapter 1, VFSs are friction base isolators, in which all, or part of the lateral stiffness variation is provided by means of sliding surfaces with spatially-varying friction coefficients. In brief, as illustrated in Figure 2.2, a VFS can be trated as the combination of a flat device with a variable coefficient of friction (Figure 2.2(b)) and an elastic spring with stiffness, K_2, equals to the borne weight, W, divided by the radius of curvature, R, of the sliding surface. A detailed illustration of the force-displacement responses of a VFS device is shown schematically in Figure 2.3. The qualitative response is sketched for a VFS with a three-ring sliding surface and with the area of the sliding pad equals to the area of the central ring. In the following discussion and in the mathematical formulation, it is assumed that the axial stress is uniformly distributed over the area of the sliding pad. Coulomb friction model is used. The effects of pressure, velocity, and surface temperature on the behavior of VFSs and the structural responses will be discussed in future chapters. Furthermore, no distinction is made between N (which typically represents the force normal to the sliding surface) and the borne weight.

As the lateral load increases from zero (Figure 2.3 (a)), VFSs exhibit a perfectly rigid response until the sliding motion is activated when the shear force equals to the axial force times the coefficient of friction of the central ring. Beyond this point, as the sliding pad slides from the center to the maximum displacement, the lateral resistance comes from both the friction force and the elastic restoring force (due to radius of curvature of the sliding surface) (Figure 2.3 (c) and (d)). When the lateral load is reduced and reversed (Figure 2.3 (e)), the lateral displacement remains unchanged until the lateral load reaches the magnitude of the

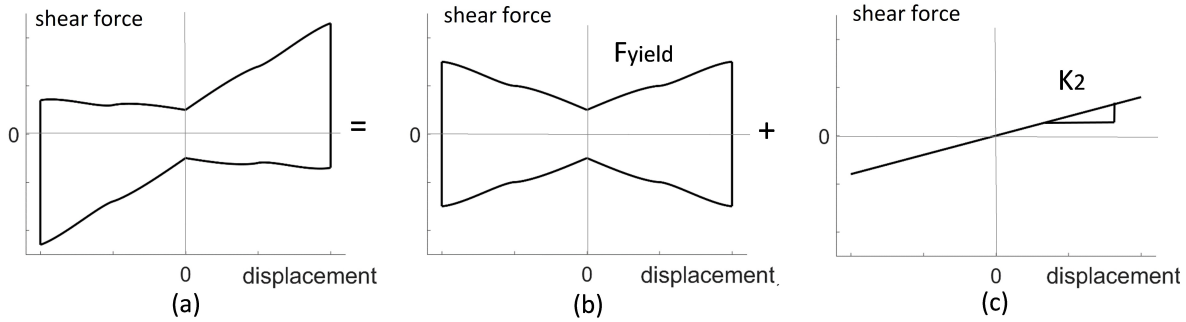

Figure 2.2: Closed form hysteretic behavior of VFSs for motion in radial direction, (a)total behavior; (b)variable friction force; (c)elastic restoring force due to radius of curvature.

resisting frictional force minus the elastic restoring force proportional to radius of curvature. The force-displacement curve then follows a symmetric trend in the reversal direction.

As illustrated in Figure 2.3, the force-displacement curves of VFSs are non-linear and are dependent on the actual geometry of the sliding surface, the size of the rings, and the frictional properties. The mathematical expression for the frictional component of shear force (F_{yield} in Figure 2.2) is shown in Equation (2.1) as derived in Calvi and Ruggiero [2016].

$$F_{yield} = \frac{N}{A} \cdot \sum_{i=1}^{n} (A_i \mu_i) \tag{2.1}$$

In Equation (2.1), N is the total vertical force acting on the bearing (in this formulation, equal to the borne weight, W), n is the number of rings interacting with the sliding pad, A is the area of the sliding pad, and μ_i and A_i represent the coefficient of friction of ring i and the overlapping area between the sliding pad and ring i, respectively. As illustrated in Figure 2.4, the sliding pad can be idealized as a circle with radius r_0, while the sliding surface can be idealized as a series of concentric rings with radii r_1, r_2, r_3 etc. In each ring, the friction coefficient between the sliding pad and sliding surface varies as a function of the surface roughness (e.g. μ_1,μ_2, μ_3 etc.). Thus, the overlapping areas, A_i, can be determined geometrically as the intersections and differences of the relevant areas as given

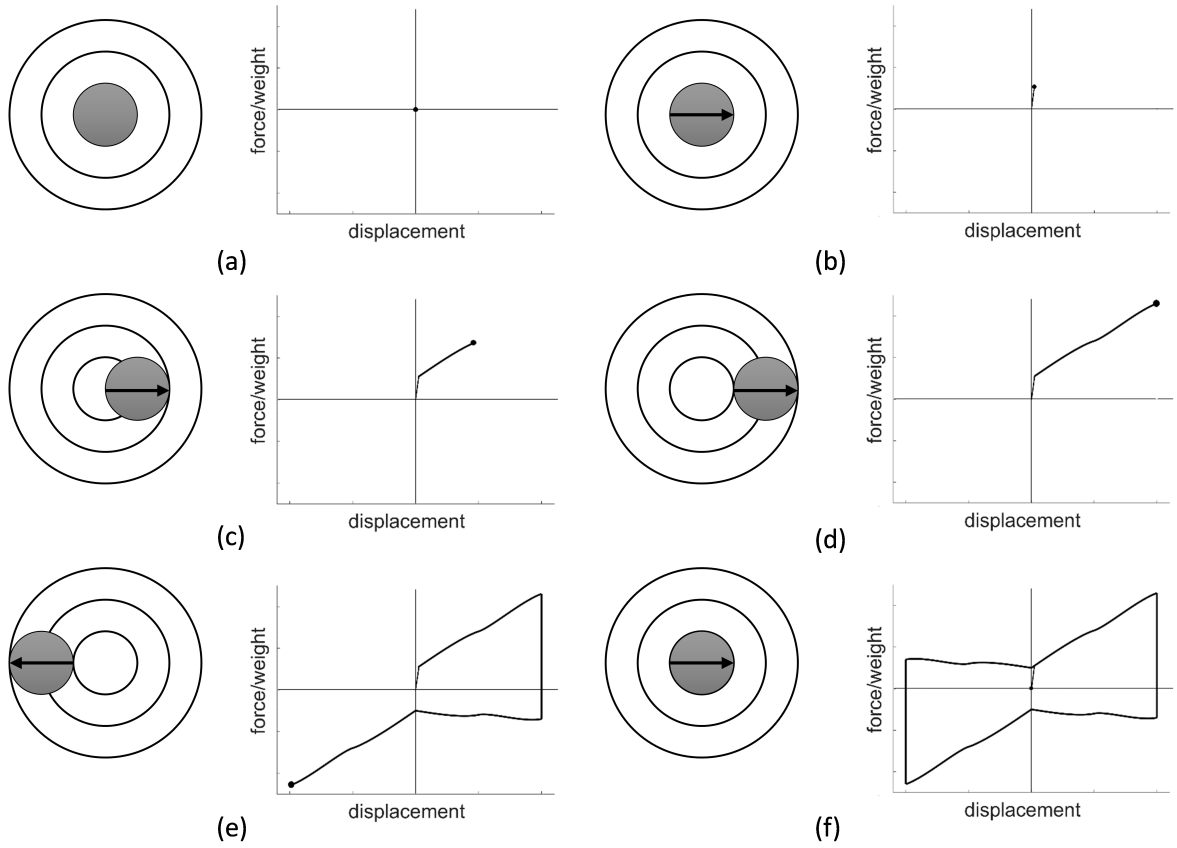

Figure 2.3: Force-displacement response of a BowTie(BT) device and a BowC(BC) device: (a) at rest; (b) pre-activation; (c) post-activation; (d) at maximum displacement; (e) lateral load reversal; (f) at initial position. This figure is modified from Calvi et al. [2016a]

by Equation (2.2):

$$A_i = \begin{cases} A(C_i \cap C_0) & i = 1 \\ A(C_i \cap C_0) - A(C_{i-1} \cap C_0) & i > 1 \end{cases} \tag{2.2}$$

where $A(C_i \cap C_0)$ represents the area of the intersection of two circles C_i and C_0. The area of the intersection of any two circles depends only on their radii and the distance between the two centers. The closed form solution to determine the area of intersection between the sliding pad and the various rings of the sliding surface is shown in Equation (2.3). r_i and r_0

represent the radii of the various rings and the radius of the sliding pad, and r represents the distance between the center of the sliding pad and the center of the sliding surface.

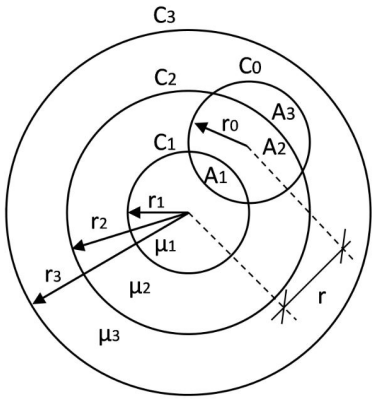

Figure 2.4: Schematic plan view of a three-ring VFS bearing

$$A(C_i \cap C_0) = \begin{cases} \pi \cdot min(r_0, r_i)^2 & r \leq |r_i - r_0| \\ r_i^2 \cos^{-1}\left(\dfrac{r^2 + r_i^2 - r_0^2}{2rr_i}\right) + & \\ r_0^2 \cos^{-1}\left(\dfrac{r^2 + r_0^2 - r_i^2}{2xr_0}\right) - & |r_i - r_0| < r \leq r_i + r_0 \\ 0.5 \cdot (-r + r_i + r_0)^{0.5} \cdot (r + r_i - r_0)^{0.5} \cdot & \\ (r - r_i + r_0)^{0.5} \cdot (r + r_i + r_0)^{0.5} & \\ 0 & r > r_i + r_0 \end{cases} \tag{2.3}$$

Finally, the total 1D shear force, F, accounting for the radius of curvature of the sliding surface, can be expressed as:

$$F = F_{yield} + \left(\frac{N}{R}\right) r \tag{2.4}$$

2.2.2 Numerical Modeling and Implementation of Variable Friction Systems

This section covers the numerical implementation of Variable Friction Systems(VFSs). First, the modified bi-directional plasticity model with circular yield surface is described. Secondly the vertical behavior of the VFSs is presented. Finally, the implementation algorithm of the VF element into OpenSees is summarized.

Bi-Directional Plasticity with Circular Yield Surface

Originated from the one-dimensional plasticity model described by Simo and Hughes [1998], the bi-directional plasticity model with circular yield surface was used by Mosqueda et al. [2004] to model the hysteretic behavior of the single Friction Pendulum bearing. Dao et al. [2013] extended and validated the same model for Double and Triple Friction Pendulum bearings. A brief review of the plasticity model is summarized herein for the single Friction Pendulum bearing.

The elastic force-displacement relationship is given by:

$$\begin{Bmatrix} f_x \\ f_y \end{Bmatrix} = K_e \left(\begin{Bmatrix} u_x \\ u_y \end{Bmatrix} - \begin{Bmatrix} u_x^p \\ u_y^p \end{Bmatrix} \right) \tag{2.5}$$

where f_x and f_y represent the horizontal force components; K_e is the pre-activation elastic stiffness; u_x and u_y represent the horizontal displacement components; u_x^p and u_y^p are the plastic displacement components. The circular yield function is then given by:

$$\Xi = \left\| \begin{matrix} f_x - \frac{N}{R_x}(u_x - u_x^p) \\ f_y - \frac{N}{R_y}(u_y - u_y^p) \end{matrix} \right\| - F_{yield} \leq 0 \tag{2.6}$$

where R_x and R_y represent effective radius of curvature in x and y direction, respectively, and can be calculated as $R_x = \sqrt{R^2 - u_y^2}$, $R_y = \sqrt{R^2 - u_x^2}$.

The associated flow rule is given by:

$$\begin{Bmatrix} \dot{u}_x^p \\ \dot{u}_y^p \end{Bmatrix} = \gamma \,\text{sign} \begin{Bmatrix} f_x \\ f_y \end{Bmatrix} \tag{2.7}$$

where γ is a consistency parameter for slip rate satisfying the Kuhn-Tucker complementary condition and consistency conditions as shown in Equation (2.8) and Equation (2.9).

$$\gamma \geq 0,\ \Xi \leq 0,\ \gamma \cdot \Xi = 0 \tag{2.8}$$

$$\gamma \cdot \dot{\Xi} = 0,\ \text{if}\, \Xi = 0 \tag{2.9}$$

This plasticity model can be adapted and used to implement the response of VFSs. To this end, the term F_{yield} in Equation (2.6) is modified from μN (for a single Friction Pendulum bearing) to the terms shown from Equation (2.1) to Equation (2.3) in order to account for the fact that F_{yield} is a function of the radial position of the sliding pad ($r = \sqrt{u_x^2 + u_y^2}$).

To deal with the bearing response in the horizontal directions, an iterative procedure is implemented for state determination (evaluating shear forces and tangent stiffness matrix given horizontal displacements of the sliding pad). Initial evaluation of the yield strength, F_{yield}, for the circular interaction surface is needed based on the bearing absolute velocity, the force normal to the sliding surface (which depends on the selected friction model), and the position of the sliding pad. A numerical return-mapping algorithm for state determination of a rate independent plasticity model, which is proposed by Simo and Hughes [1998], is also extended and shown as below.

The algorithm consists of the following key steps. First, compute the trial force vector and calculate the yield function, Ξ_{n+1}^{trial}, given a displacement vector at step n+1, $[u_x\ u_y]_{n+1}^T$:

$$\begin{Bmatrix} f_x \\ f_y \end{Bmatrix}_{n+1}^{trial} = K_e \left(\begin{Bmatrix} u_x \\ u_y \end{Bmatrix}_{n+1} - \begin{Bmatrix} u_x^p \\ u_y^p \end{Bmatrix}_{n} \right) \tag{2.10}$$

$$\boldsymbol{\xi}_{n+1}^{trial} = \begin{Bmatrix} \xi_x \\ \xi_y \end{Bmatrix}_{n+1}^{trial} = \begin{Bmatrix} f_x \\ f_y \end{Bmatrix}_{n+1}^{trial} - \begin{Bmatrix} \frac{N_{n+1}}{R_{x,n+1}}(u_{x,n+1} - u_{x,n}^p) \\ \frac{N_{n+1}}{R_{y,n+1}}(u_{y,n+1} - u_{y,n}^p) \end{Bmatrix} \tag{2.11}$$

$$\Xi_{n+1}^{trial} = \left\| \boldsymbol{\xi} \right\|_{n+1}^{trial} - F_{yield} \tag{2.12}$$

Then one can evaluate based on Ξ_{n+1}^{trial} to determine if the system is in elastic or plastic regime. If $\Xi_{n+1}^{trial} \leq 0$, the system is in the elastic regime, the force vector remains the same as the trial force vector, and the tangent stiffness, $\boldsymbol{K}$, corresponds to the elastic stiffness matrix:

$$\begin{Bmatrix} f_x \\ f_y \end{Bmatrix}_{n+1} = \begin{Bmatrix} f_x \\ f_y \end{Bmatrix}_{n+1}^{trial} \tag{2.13}$$

$$\boldsymbol{K} = \begin{bmatrix} K_e & 0 \\ 0 & K_e \end{bmatrix} \tag{2.14}$$

If the system is in the plastic regime (i.e. $\Xi_{n+1}^{trial} > 0$), both force and plastic displacement vectors need to be updated as follows:

$$\begin{Bmatrix} \Delta\gamma_x \\ \Delta\gamma_y \end{Bmatrix} = \begin{Bmatrix} \Xi_{n+1}^{trial}/(K_e - {}^{N}/_{R_x}) \\ \Xi_{n+1}^{trial}/(K_e - {}^{N}/_{R_y}) \end{Bmatrix} \tag{2.15}$$

$$\begin{Bmatrix} f_x \\ f_y \end{Bmatrix}_{n+1} = F_{yield} \frac{\boldsymbol{\xi}_{n+1}^{trial}}{\left\| \boldsymbol{\xi} \right\|_{n+1}^{trial}} + \begin{Bmatrix} \frac{N}{R_x} u_{x,n+1} \\ \frac{N}{R_y} u_{y,n+1} \end{Bmatrix} \tag{2.16}$$

$$\begin{Bmatrix} u_x^p \\ u_y^p \end{Bmatrix}_{n+1} = \begin{Bmatrix} u_x^p \\ u_y^p \end{Bmatrix}_n + \frac{1}{\left\| \boldsymbol{\xi} \right\|_{n+1}^{trial}} \begin{Bmatrix} \Delta\gamma_x \xi_{x,n+1}^{trial} \\ \Delta\gamma_y \xi_{y,n+1}^{trial} \end{Bmatrix} \tag{2.17}$$

The tangent stiffness matrix becomes:

$$\boldsymbol{K} = \begin{bmatrix} K_{xx} & K_{xy} \\ K_{yx} & K_{yy} \end{bmatrix} \tag{2.18}$$

The terms of the tangent stiffness matrix under the plastic regime can be determined as follows:

$$K_{xx} = \left\{\frac{\partial f_x}{\partial u_x}\right\}_{n+1} = \frac{\partial}{\partial u_x}\left[F_{yield}\cdot\frac{\xi_{x,n+1}}{\left\|\boldsymbol{\xi}\right\|_{n+1}^{trial}} + \frac{N}{R_x}\cdot u_{x,n+1}\right] \tag{2.19}$$

$$\frac{\partial}{\partial u_x}F_{yield}(r) = \frac{\partial}{\partial r}F_{yield}(r)\cdot\frac{\partial}{\partial u_x}r(u_x) \tag{2.20}$$

$$\frac{\partial}{\partial u_x}r(u_x) = \frac{\partial}{\partial u_x}\sqrt{u_x^2+u_y^2} = \frac{u_x}{\sqrt{u_x^2+u_y^2}} \tag{2.21}$$

$$K_{VFS} = \frac{\partial}{\partial r}F_{yield} = \frac{N}{A}\cdot\sum_{i=1}^{n}\left(\frac{dA_i}{dr}\mu_i\right) \tag{2.22}$$

where

$$\frac{dA_i}{dr} = \frac{d}{dr}\Big[A(C_i\cap C_0) - A(C_{i-1}\cap C_0)\Big] \tag{2.23}$$

and

$$\frac{d}{dr}A(C_i\cap C_0) = \begin{cases} 0 & r \le r_i - r_0 \\ -\dfrac{\sqrt{(-r+r_0+r_i)(r+r_0-r_i)(r-r_0+r_i)(r+r_0+r_i)}}{r} & r_i - r_0 < r \le r_i + r_0 \\ 0 & r > r_i + r_0 \end{cases} \tag{2.24}$$

$$\frac{\partial}{\partial u_x}\left(\frac{\xi_x}{\left\|\boldsymbol{\xi}\right\|}\right) = \left(K_e - \frac{N}{R_x}\right)\frac{\xi_y^2}{\left\|\boldsymbol{\xi}\right\|^3} \tag{2.25}$$

Substituting Equations 2.20, 2.21, 2.22, and 2.25 into Equation (2.19), the first component, K_{xx}, of the tangent stiffness matrix can be calculated as:

$$K_{xx} = \frac{u_{x,n+1}}{\sqrt{u_{x,n+1}^2+u_{y,n+1}^2}}\cdot K_{VFS}\cdot\frac{\xi_{x,n+1}}{\left\|\boldsymbol{\xi}\right\|}_{n+1} + F_{yield}\left(K_e - \frac{N}{R_x}\right)\frac{\xi_{y,n+1}^2}{\left\|\boldsymbol{\xi}\right\|_{n+1}^3} + \frac{N}{R_x} \tag{2.26}$$

Similarly,

$$K_{xy} = K_{xy} = \frac{u_{x,n+1}}{\sqrt{u_{x,n+1}^2 + u_{y,n+1}^2}} \cdot K_{VFS} \cdot \frac{\xi_{y,n+1}}{\left\|\boldsymbol{\xi}\right\|}_{n+1} - F_{yield}\left(K_e - \frac{N}{R_x}\right)\frac{\xi_{x,n+1}\xi_{y,n+1}}{\left\|\boldsymbol{\xi}\right\|_{n+1}^3} \quad (2.27)$$

$$K_{yy} = \frac{u_{y,n+1}}{\sqrt{u_{x,n+1}^2 + u_{y,n+1}^2}} \cdot K_{VFS} \cdot \frac{\xi_{y,n+1}}{\left\|\boldsymbol{\xi}\right\|}_{n+1} + F_{yield}\left(K_e - \frac{N}{R_y}\right)\frac{\xi_{x,n+1}^2}{\left\|\boldsymbol{\xi}\right\|_{n+1}^3} + \frac{N}{R_y} \quad (2.28)$$

Note that when the sliding surface is curved, the force normal to the sliding surface, N, is not aligned with the z-axis (i.e the vertical direction). To achieve a more accurate representation of the bearing response, this phenomenon should be taken into account. To this end, the relationship between the horizontal displacements u_x and u_y, the vertical load W, the sliding surface radius of curvature R, and the horizontal shear force F_x and F_y, is provided in Equation (2.29):

$$N = -W\frac{\sqrt{R^2 - u_x^2 - u_y^2}}{R} + F_x\frac{u_x}{R_x} + F_y\frac{u_y}{R_y} \quad (2.29)$$

As mentioned in Section 2.2.1, F_{yield} is not only a function of the position of the sliding pad, but it also depends on the force acting on the sliding pad in the direction normal to the sliding surface, which is in turn dependent on the shear forces, as shown in Equation (2.29). Thus, an iterative procedure is required to find the converged shear forces and tangent stiffness matrix for a given displacement vector.

Vertical behavior

As for other sliding base isolators presented in the literature (e.g. Dao et al. [2013]), the vertical force-displacement relationship characterizing a VFS can be modeled as linear elastic, with different stiffness values in tension (K_T) and compression (K_C). Theoretically, VFSs are compression only systems, however, a comparably small tensile stiffness can be assigned to ensure numerical stability of the analysis when uplift occurs. It is worth mentioning that

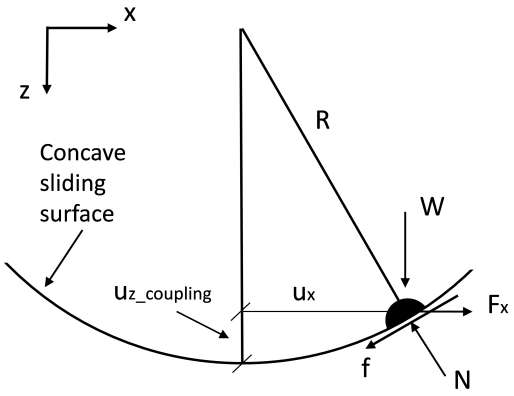

Figure 2.5: Schematic drawing of the forces acting on the sliding pad (adapted from Mosqueda et al. [2004])

this is not necessary so long as the vertical stiffness of the entire system remains non-zero.

Thus, the total force acting on the bearing in the z-direction, F_z, can be calculated as:

$$F_z = (K_C \text{ or } K_T) \cdot (u_z + u_{z,coupling}) \tag{2.30}$$

where u_z is the total vertical displacement and $u_{z,coupling}$ is the coupled vertical displacement of the sliding pad as a function of the horizontal distance traveled, u_x and u_y, and R (as shown in Figure 2.5 for a simple 2D case). In 2D, this term is calculated using Equation (2.31).

$$u_{z,coupling} = R - \sqrt{R^2 - u_x^2} \tag{2.31}$$

In 3D, Equation (2.31) becomes:

$$u_{z,coupling} = R - \sqrt{R^2 - u_x^2 - u_y^2} \tag{2.32}$$

If one wishes to decouple the vertical response from the horizontal response, the $u_{z,coupling}$ term in Equation (2.30) can be neglected.

Implementation Algorithm and OpenSees Command for VFSs

A compact 3D VFS element was developed and implemented based on the framework of the original Single Friction Pendulum Bearing Element that is readily available in *OpenSees*. Figure 2.6 and Figure 2.7 show a schematic view of the VFS element and the implementation algorithm, respectively. These systems are treated as two-node elements, in which one node represents the concave/flat sliding surface and the other represents the sliding pad. The element can have zero length or it can be assigned the actual bearing height by defining the nodal coordinates to corresponding values. The shear deformation properties are described in Section 2.2.1, and the force-deformation behaviors for the remaining directions (two for 2D and four for 3D) can be defined using UniaxialMaterials.

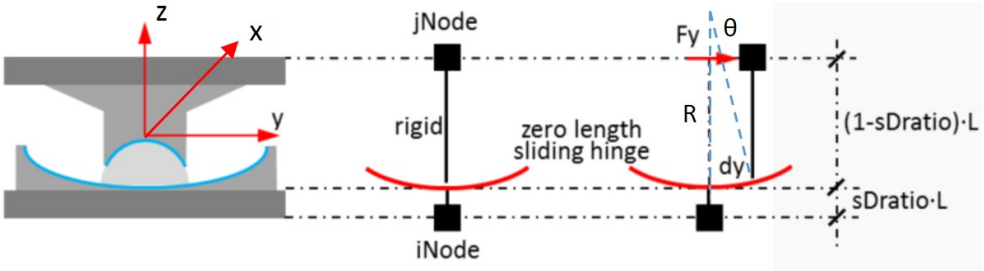

Figure 2.6: Schematic drawing of the Variable Friction element in OpenSees. Retrieved and modified from Schellenberg [2014].

More modeling options are listed and described in Table 2.1, which is retrieved and modified from Schellenberg [2014]. The command line for defining the newly implemented VFS element in OpenSees in both 2D and 3D environments are:

For a 2D problem:

element VFSbearing $eleTag $iNode $jNode $frnMdlTag1 $frnMdlTag2 $frnMdlTag3 $R $kInit $$r_0$$ $$r_1$$ $$r_2$$ $$r_3$$ -P $matTag -Mz $matTag <-orient $$x_1$$ $$x_2$$ $$x_3$$ $$y_1$$ $$y_2$$ $$y_3$$> <-shearDist $sDratio> <-doRayleigh> <-mass $m> <-iter $maxIter $tol>

For a 3D problem:

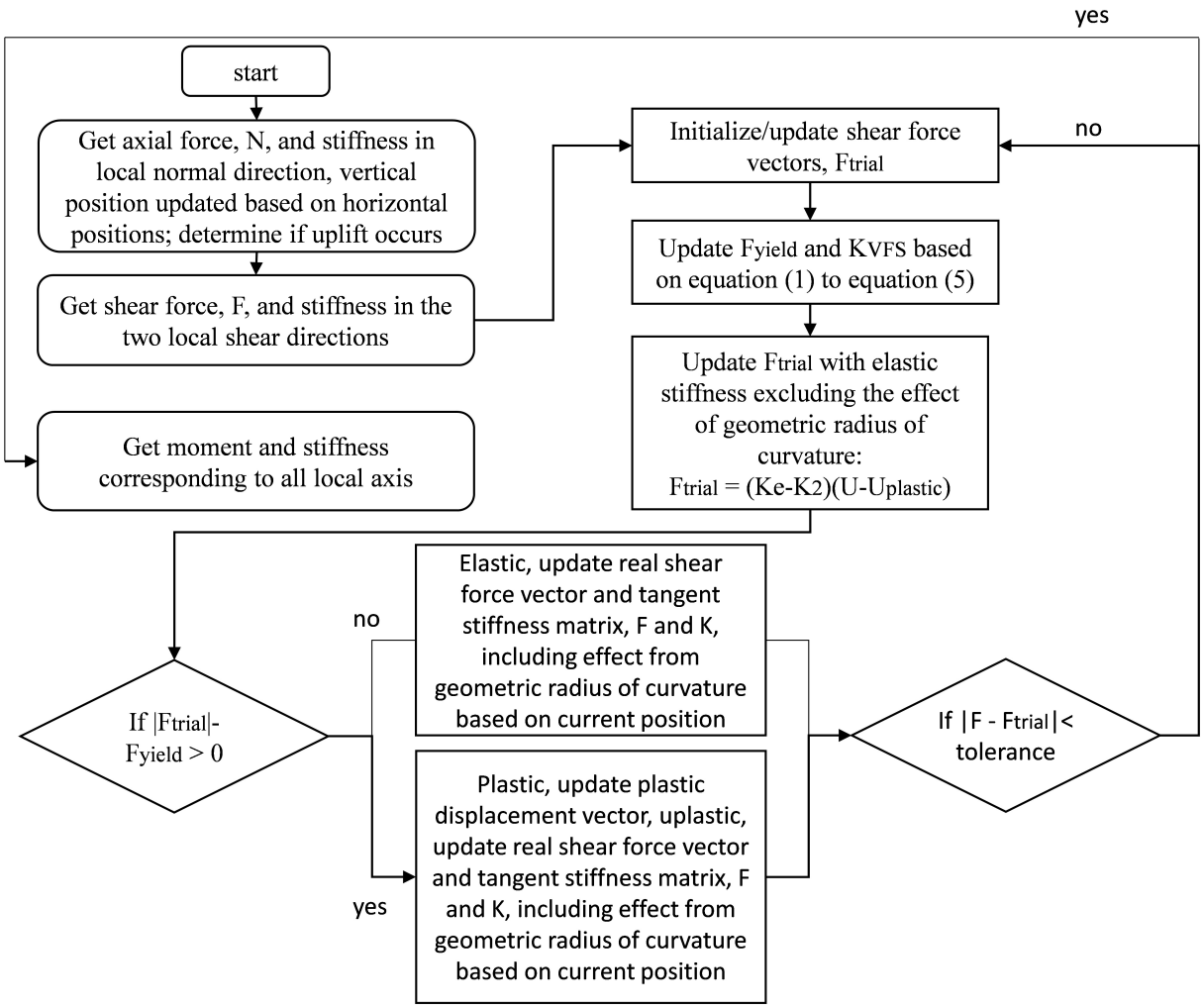

Figure 2.7: Algorithm for VFSs implementation into OpenSees

element VFSbearing $eleTag $iNode $jNode $frnMdlTag1 $frnMdlTag2 $frnMdlTag3 $R $kInit $$r_0$$ $$r_1$$ $$r_2$$ $$r_3$$ -P $matTag -T $matTag -My $matTag -Mz $matTag <-orient $$x_1$$ $$x_2$$ $$x_3$$ $$y_1$$ $$y_2$$ $$y_3$$> <-shearDist $sDratio> <-doRayleigh> <-mass $m> <-iter $maxIter $tol>

Property	Description
$eleTag	unique element object tag
$iNode $jNode	tags of end nodes
$frnMdlTag1 $frnMdlTag2 $frnMdlTag3	tags associated with previously defined friction model for each rings
$R	radius of concave sliding surface
$kInit	initial elastic stiffness in local shear direction
$$r_0$$	radius of the sliding pad
$$r_1$$ $$r_2$$ $$r_3$$	radius of the first to the third ring
-P $matTag	tag associated with previously defined UniaxialMaterial in axial direction
-T $matTag	tag associated with previously defined UniaxialMaterial in torsional direction
-My $matTag	tag associated with previously defined UniaxialMaterial in moment direction around local y-axis
-Mz $matTag	tag associated with previously defined UniaxialMaterial in moment direction around local z-axis
$$x_1$$ $$x_2$$ $$x_3$$	vector components in global coordinates defining x-axis (optional)
$$y_1$$ $$y_2$$ $$y_3$$	vector components in global coordinates defining y-axis (optional)
$sDratio	shear distance from iNode as a fraction of the element length (optional, default = 0.0)
-doRayleigh	to include Rayleigh damping from the bearing(optional, default = no Rayleigh damping contribution)
$m	element mass (optional, default = 0.0)
$maxIter	maximum number of iterations to undertake to satisfy element equilibrium (optional, default = 20)

$tol	convergence tolerance to satisfy element equilibrium (optional, default = 1E-8)

Table 2.1: Description of the input properties of the VFS element in OpenSees

2.3 Numerical Demonstration with a Case Study Structure

The aim of this section is to test the capabilities of the newly implemented element, while providing a demonstration of the behavior of VFSs when used to isolate structures under real ground motions in the context of NLTH analyses.

In the process, one of the key design assumptions proposed for VFSs Calvi and Ruggiero [2016], namely that the hysteretic behavior of VFSs can be simplified as multi-linear, was validated via NLTH analyses. It should be noted that the multi-linear model (referred to in this section as approximate model) is only used at the stage of preliminary design for its simplicity, in particular, when evaluating the effective damping value. The true VFS model was used in the NLTH analyses of the case study structure.

2.3.1 Performance of Simplified VFS Multi-Linear Model

As discussed in Section 2.2.1, the true hysteretic behavior of VFSs is non-linear to an extent which depends on the bearing characteristics. However, for design purpose (especially at a preliminary stage), it is convenient to represent the bearing force-displacement response with simplified multi-linear models (as shown in Figure 2.8, dashed line). A detailed discussion of these aspects can be found in Timsina and Calvi [2018], while a possible design procedure to select appropriate friction values and ring radii, in order to achieve VFSs with a nearly multi-linear hysteretic response is described in Calvi and Ruggiero [2016].

This section aims to utilize the newly developed element in OpenSees and NLTH analyses, to gauge the accuracy of representing the true behavior of VFSs with simplified multi-linear models at the stage of preliminary design.

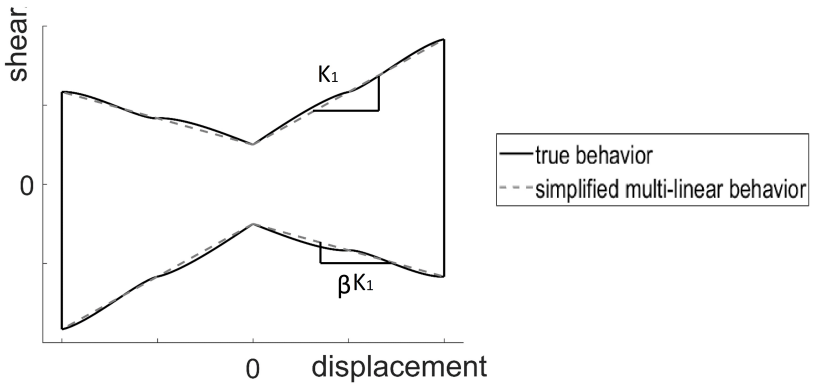

Figure 2.8: Demonstration of k_1 and βk_1, where in the x-xais the displacement of the sliding pad is normalized by the maximum displacement

To allow modeling of the VFS response using the approximate multi-linear behavior, two new parameters were introduced: (i) the post-activation stiffness with increasing displacement, k_1; and (ii) the post-activation stiffness with decreasing displacement, βk_1 (both parameters are outlined in Figure 2.8).

In addition, the VFS algorithm summarized in Figure 2.7 was modified as follows:

The calculation of F_{yield} and $K2$ are derived from Equation (2.33) and Equation (2.34), as the relationship can be observed from Figure 2.2 and Figure 2.8.

$$\mu N(v, N) + K_1 r = F_{yield} + K_2 r \tag{2.33}$$

$$-\mu N(v, N) + \beta K_1 r = -F_{yield} + K_2 r \tag{2.34}$$

where $K1$ equals to N/R_{eff} (with R_{eff} representing the effective radius of curvature), $\mu N(v, N)$ represents the activation friction force when $x = 0$. The friction coefficient may be dependent on velocity, v, or normal force, N, depending on which friction model the user chooses to use. By algebraic manipulation, F_{yield} and K_2 are shown in Equation (2.35) and Equation (2.36) respectively.

Table 2.2: Properties of the true behavior model and the multi-linear model for β equals to zero

Properties	r_0 (m)	r_1 (m)	r_2 (m)	r_3 (m)	μ_1 (%)	μ_2 (%)	μ_3 (%)	R (m)	β
True behavior	0.08	0.08	0.24	0.4	5	7	9	8.33	N/A
Multi-linear	N/A	N/A	N/A	N/A	5	N/A	N/A	4.16	0

$$F_{yield} = \mu N(v, N) + \frac{(1-\beta)N}{2R} r \tag{2.35}$$

$$K_2 = \frac{(1+\beta)N}{2R} \tag{2.36}$$

The case study structures considered in this section consisted of a series of single-degree-of-freedom systems, isolated by means of VFSs characterized by four β values, ranging from -1.0 to 0.5 with an increment of 0.5. Both "true models" and "multi-linear models" were considered for the VFSs. To this end, the systematic properties of the VFSs tested in the two models are summarized in Table 2.2. The structures were analyzed under a set of 10 pairs of real ground motions (described in Section 2.3.2).

For the sake of brevity, only the results pertaining to the VFS with β equals to zero are presented here. Other β values yielded to similar results. Figure 2.9 shows the comparison between both the theoretical hysteretic curves and one example hysteretic curves from numerical results obtained from the two VFS models.

The results of the NLTH analyses showed that the differences in terms of maximum displacement and maximum base shear between the two models were all within 1.5%, with an average difference of 1.1%. Thus, the multi-linear model is considered sufficiently accurate to represent the true behavior of VFSs when appropriate radii and friction values are chosen, and this simplification can be adopted, at least at preliminary design stages.

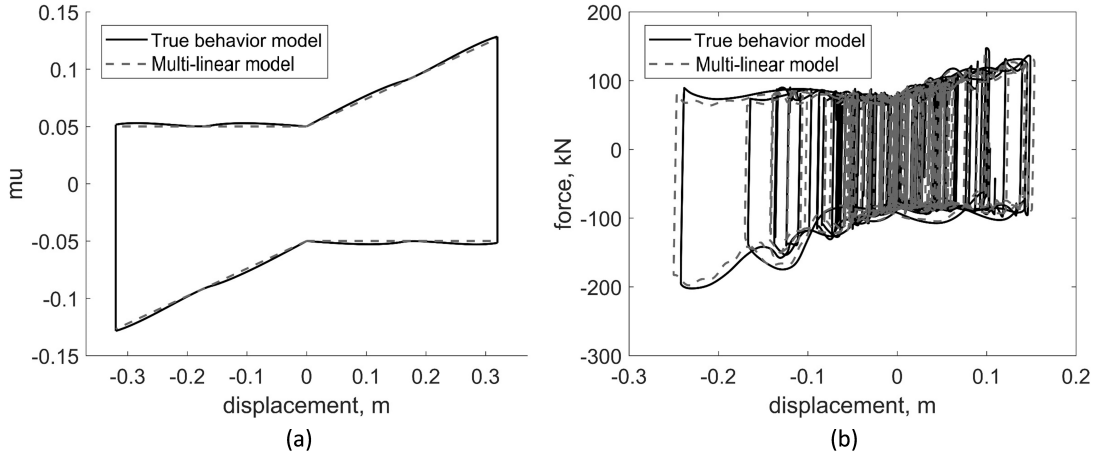

Figure 2.9: Comparison of the (a) theoretical hysteresis and (b) example hysteresis from NLTH analysis of the true behavior model and the simplified multi-linear model.

2.3.2 Non-linear Time History Analysis of Case Study Structures

The case study structures consisted of 2D and 3D steel moment resisting frames with a constant bay width of 12 feet and a constant story height of 12 feet, selected from the OpenSees library. The details of the structures can be found in Schellenberg [2014]. Analyzing FP systems modeled using the new element (with all rings set to have identical friction properties) and the element readily available in OpenSees, served as initial verification of the correct implementation of the algorithm.

The "baseline" case study structures are shown in Figure 2.10 (a) and (b). Base isolation systems consisting of 4 FP systems (i.e. VFSs with $\beta = 1.0$) were designed for the case study structures. A direct displacement based design (DDBD) approach was adopted, following the recommendations of Timsina and Calvi [2018]. The bearing design displacement was selected as 10 inches and the design-to-activation base shear ratio (design parameter α) was selected as 3.0 (which corresponds to an equivalent viscous damping of 21%, as discussed by Timsina and Calvi [2018]). The design spectrum adopted in this study was generated based on the ASCE 7-10 ASCE [2010] for downtown San Francisco (shown in Figure 2.11), with

Table 2.3: Summary of the design properties of VFSs with β equals to 1.0

	W (kips)	μ (%)	R (m)	r_0 (m)	r_s (m)
Exterior column	18	5	120	6	20

soil type C.

The main properties of the base isolators obtained from the design process are summarized in Table 2.3, where r_s represents the radius of the sliding surface. It should be noted that, due to the low weight from the case study structure, the pressure on each slider in the current design is lower than what would be expected in practice. However, this issue would mainly affect the numerical analysis if pressure-dependent friction model is used. In this study, Coulomb friction model is adopted.

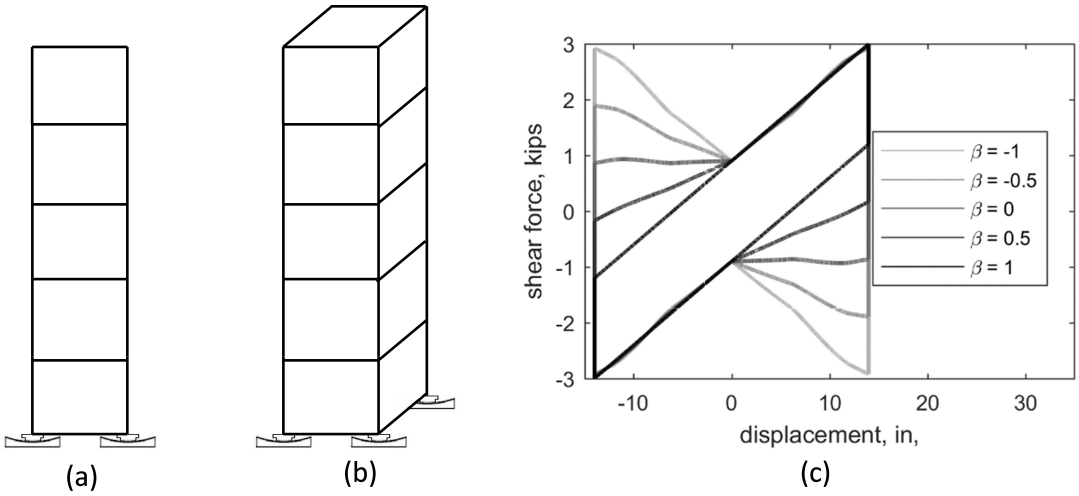

Figure 2.10: (a) 2D, and (b) 3D view of the five-story-one-bay structure in OpenSees Single Friction Pendulum Bearing Element example; (c) theoretical hysteretic behavior of VFSs.

After completing the design of the "baseline" systems, four VFS sets characterized by β values ranging from -1.0 to 0.5 (increment of 0.5) and nearly multi-linear response were designed to match the backbone force-displacement response of the "baseline" isolators summarized in Table 2.3. The design of these bearings was conducted following the recommen-

Table 2.4: Summary of VFSs under each column

β	μ_1 (%)	μ_2 (%)	μ_3 (%)	R (in)	r_0 (in)	r_1 (in)	r_2 (in)	r_3 (in)
-1.0	5	12	18	100000*	6	6	12	20
-0.5	5	11	14	480	6	6	12	20
0	5	9	11	240	6	6	12	20
0.5	5	7	8	160	6	6	12	20

* technically the radius of curvature for a VFS with β equals to -1.0 should be infinite, however, for numerical purposes, a comparably large number is chosen.

dations of Calvi and Ruggiero [2016]. Their main properties are summarized in Table 2.4, while the hysteretic response of all the base isolators considered are outlined in Figure 2.10 (c). No modifications to the superstructure shown in Figure 2.10 (a) and (b) were made.

It should be noted that considering different VFSs with identical backbone response is only one of the many possible response comparisons that can be conducted. For instance, one may design different VFS bearings to undergo the same maximum displacement under earthquake excitations, without constraints on the force-displacement response. To this end, performing an extensive parametric study to gauge advantages and drawbacks of the various systems under a variety of circumstances is certainly an important research need, and should be considered in the future.

It should also be noted that the VFS theoretical development and the numerical element introduced earlier retain a general form, and can be used to model and study the response of generic VFSs with highly non-linear and/or adaptive hysteretic behavior.

Finally, it should be noted that some of the coefficient of friction or radius of curvature values selected may not be realistic (e.g. $\mu = 18\%$). In general, constructability or other practical considerations may limit the freedom in selecting a specific value of friction coefficient or radius of curvature. However, these aspects are beyond the scope of this paper, but remain as important research questions that will be addressed as part of the ongoing investigations.

With this in mind, it is assumed that systems characterized by the properties reported

in Table 2.4 can be achieved, and will be considered in the following of this study.

Numerical models of the case study structures were built in OpenSees and analyzed under a suite of real spectrum compatible ground motions scaled to match the MCE design spectrum. Linear elastic beam and column elements were used for the modeling of the superstructure. A Rayleigh damping of 1% was assigned to the first two modes of the superstructure. This may not represent the most appropriate modeling assumption as the Rayleigh's model tends to produce unrealistically high damping of lower frequencies Petrini et al. [2008] Smyrous et al. [2011], leading to overly optimistic predictions of the performance of base isolated structures Hall [2006] Ryan and Polanco [2008]. However, while alternative damping models may be selected in other circumstances, Rayleigh's damping was considered acceptable at this preliminary stage given that even though the assumed elastic damping had some effect on the computed responses, those effects were similar for all systems and therefore did not affect the comparisons between the different systems.

In addition to the properties listed earlier, the bearings were assigned a compressive stiffness calculated to achieve a vertical period of vibration of the structure of 0.03 seconds Warn and Ryan [2012]. A set of 7 pairs of ground motions and a set of 7 individual ground motions were selected from NGA-WEST2 ground motion database for the 3D and 2D analyses respectively. The acceleration and displacement spectrum associated to the scaled records are plotted in Figure 2.11. The following criteria were adopted for the ground motion selection: (i) magnitude from 6.5 to 8.5; (ii) Joyner-Boore distance from 5 to 30km; and (iii) effective duration of motion from 10 to 60 seconds. Pulse-like ground motions were excluded from the selection. Then each pair of ground motion for the 3D analysis (individual ground motion for 2D analysis) was scaled to have a response spectrum with a minimum norm-2 log-scale error compared to the design spectrum.

The solution algorithm employed within the NLTH analyses consisted of Newmark's method, with constant average acceleration, and the Newton-Raphson method was employed to calculate the VF element secant stiffness within each time step. The analyses showed that the newly implemented VF element is numerically stable. In addition, the new element

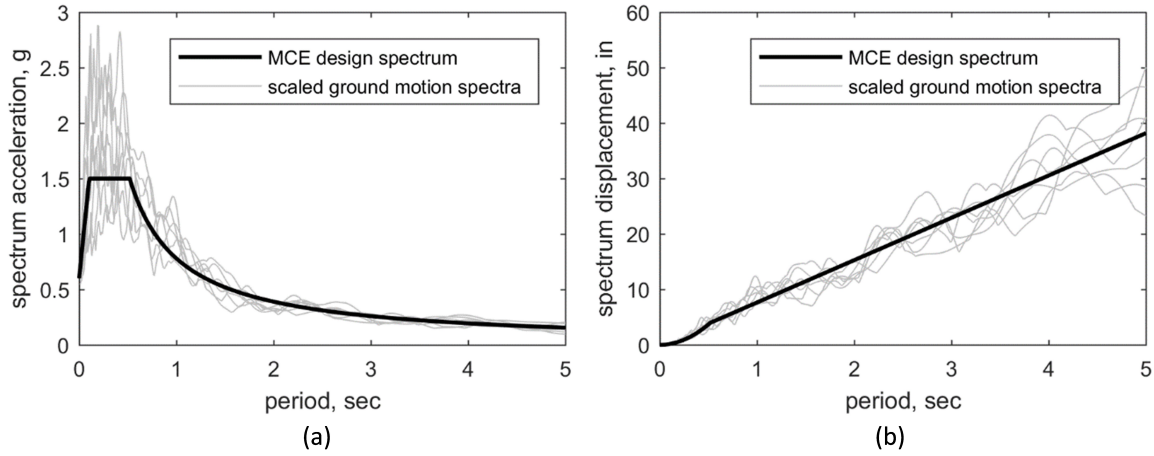

Figure 2.11: Design spectrum and scaled ground motion spectrum comparison for (a) acceleration and (b) displacement.

proved to be numerically efficient, with computational analysis time comparable to that of a traditional FP element.

The key results of the analyses are illustrated in Figure 2.12. Performance comparisons between VFSs with different β values are provided in terms of maximum base shear, maximum displacement, and normalized residual displacement (with respect to the maximum displacement). Theoretically, VFSs exhibit larger energy dissipation capacities when compared to the "baseline" set of friction pendulum bearings (i.e. $\beta = 1.0$), thus would be expected to reduce maximum displacement and maximum base shear transmitted to the superstructure. The results from both 2D and 3D analyses exhibit this expected trend. However, the analyses show that with the decrease in β value, the normalized residual displacement of the system increases nonlinearly (i.e. more rapidly) and is particularly critical for the case of VFSs with $\beta = -1.0$ (i.e. flat sliding surface). This poor performance is due to the fact that a VFS with $\beta = -1.0$ has no inherent systematic restoring force, and it is prone to a non-vibratory response as soon as the sliding pad remains stuck at a certain location along the sliding surface. This tendency may lead the system to experience larger maximum displacement, maximum base shear, and normalized residual displacement

compared to other VFSs.

An example set of displacement history comparisons among different VFSs (with the same ground motion) are shown in Figure 2.13 for the 2D case. A set of trajectories for the 3D case is shown in Figure 2.14. The circles in Figure 2.12 indicate where the maximum displacements occur. The stars and circles in Figure 2.14 indicate where the residual displacements and maximum displacements occur, respectively. In Figure 2.14, the color of the curve changes from light grey to black as an indication of time. Eventually, the curve stops at the star point, which represents the final residual displacement.

The minimum (vertical) axial force in the bearing elements was also checked to ensure that bearing uplift had not occurred in any of the analyses.

Overall, the results collected in this section are consistent with the results reported in Calvi and Timsina [2017], obtained via 1D analysis using less sophisticated bearing elements and building models. Obviously, the results of the analyses presented in this section are very preliminary in nature and they pertain to two specific case study structures, a specific design method, and only one earthquake intensity. Thus, before drawing any conclusions on the performance of the systems analyzed and, more generally of VFSs, more extensive parametric studies should be conducted. With the newly implemented 3D plasticity model that is capable of capturing the full behavior of VFSs, more complex aspects of the structural and bearing response are now ready to be investigated.

2.4 Experimental Program

In addition to the mechanical and numerical formulations, the development and implementation of VFSs require extensive experimental evidence and validation. Thus, a series of full scale VFS prototypes are currently being tested in the EUCENTRE laboratory, as part of the research project.

VFSs characterized by different sizes, frictional properties, radii of curvature of the sliding surface, vertical pressures etc. are being subjected to a series of loading protocols that involve unidirectional displacement controlled harmonic motions and realistic ground motions with

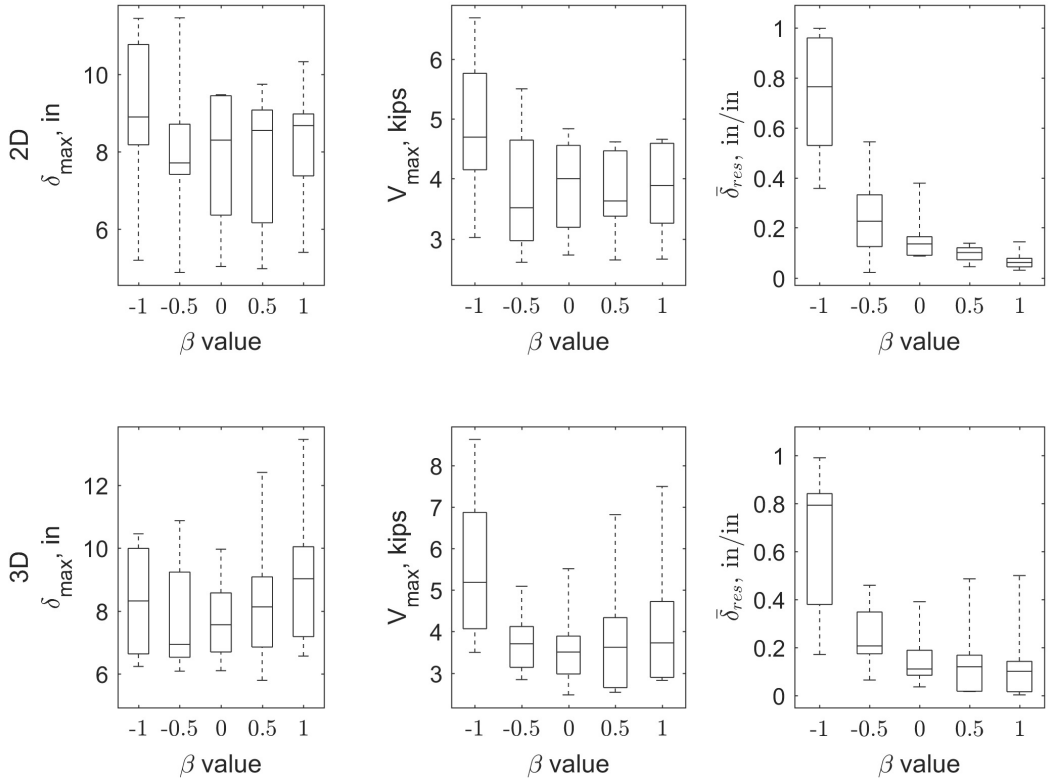

Figure 2.12: Comparison of maximum displacement, δ_{max}, maximum base shear, V_{max}, and normalized residual displacement, δ_{res}, for both 2D and 3D analyses.

different intensities, using the state of the art bearing tester shown in Figure 2.15. More details on the characteristics of this testing apparatus, the testing procedures, the testing protocols, and the data post processing procedures can be found in a preliminary technical report (Appendix A).

While the VFS bearing tests are ongoing, the preliminary results pertaining to two prototype groups are available. The experimental results are presented in this section with the intent of providing some initial validation of the numerical model presented in the previous section.

The main properties of the two prototype groups are summarized in Table 2.5. The prototype bearings consisted of "two-ring" systems, in which the concave stainless steel

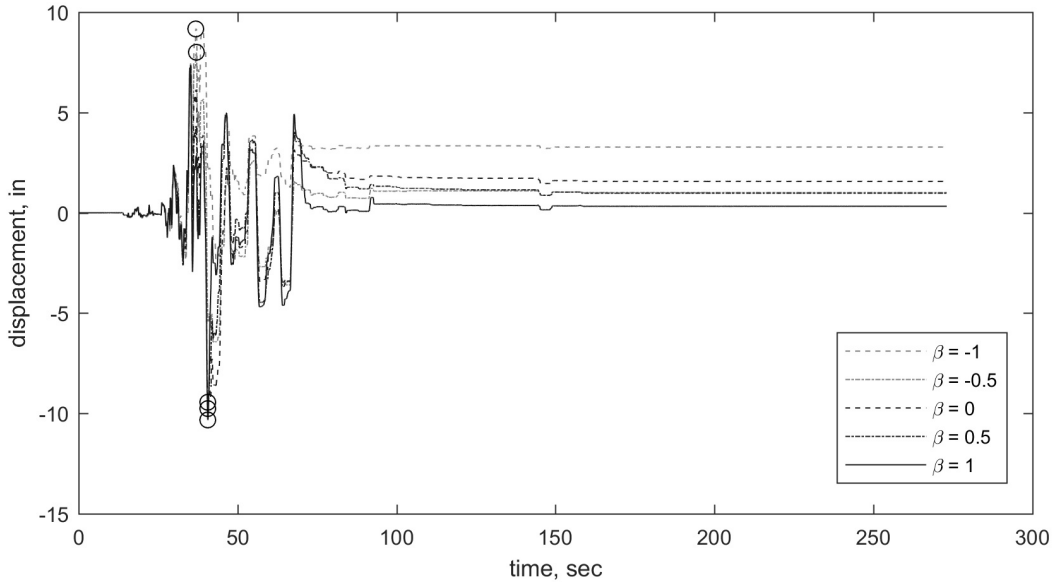

Figure 2.13: Example bearing displacement history comparison from 2D non-linear time history analyses.

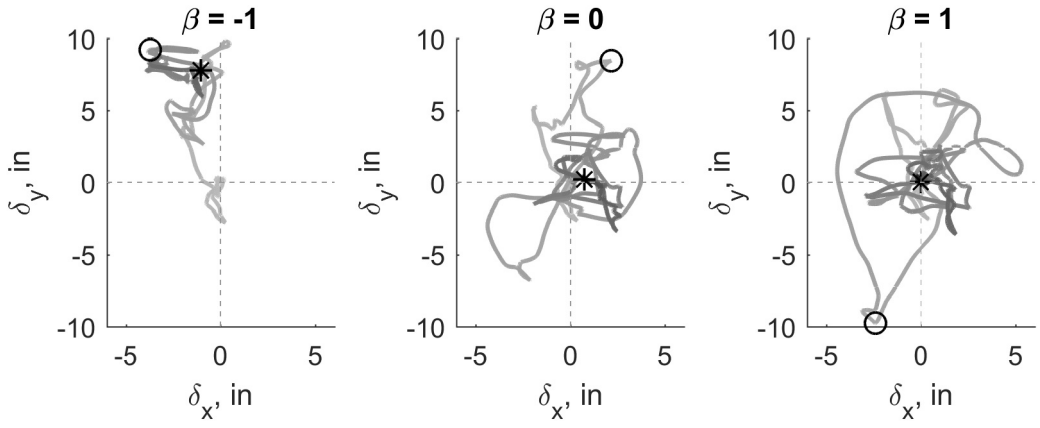

Figure 2.14: Example bearing trajectory comparison from 3D non-linear time history analyses.

sliding surface was treated using different polishing techniques to achieve spatially varying frictional properties. The parameters reported in Table 2.5 represent the radius of the sliding pad (r_0), the radius of the low friction ring (r_1), the radius of the high friction ring (r_2),

Figure 2.15: (a) The EUCENTRE Laboratory bearing tester; (b) Elevation view of the bearing test setup.

the coefficient of friction of the low friction ring (μ_1), the coefficient of friction of the high friction ring (μ_2), and the radius of curvature (R).

The dynamic friction coefficients between the sliding pad and the sliding surface achieved using this approach were equal to 7.0% and 9.2% for the inner and outer rings, respectively. These values were provided by the bearing manufacturer and were validated from friction characterization tests performed in the laboratory, under a vertical pressure with 25 MPa. It is worth noting that achieving different values of friction is extremely difficult, which limited the selection of the friction values. It has been an ongoing effort to test more friction values by the partner institution.

Table 2.5: Properties of the tested VFS prototypes

Group #	Prototype #	r_0 (m)	r_1 (m)	r_2 (m)	μ_1 (%)	μ_2 (%)	R (m)
1	1	0.125	0.15	0.45	7.0	9.2	4.5
	2	0.125	0.225	0.45	7.0	9.2	4.5
2	1	0.100	0.150	0.45	7.0	9.2	4.5

Following the friction characterization tests, the Group 1 VFS prototypes were subjected to 3-cycle unidirectional harmonic displacement histories, with a displacement amplitude of ± 0.3 m. The peak velocity reached was 500 mm/second and 200 mm/second, for prototype 1 and prototype 2, respectively. The Group 2 prototype was subjected to recorded ground motions with different intensities. The slider peak velocity in the two tests reported here reached approximately 950 mm/sec.

The horizontal force-displacement response characterizing the Group 1 VFSs tested is reported in Figure 2.16. The black lines represent the first-cycle response, while the grey lines refer to the second and third loading cycles. It can be seen that the first-cycle response differs quite significantly from that of the subsequent cycles. It can be seen that the first-cycle response differs quite significantly from that of the subsequent cycles. In particular, the effects of the variable friction are clearly visible in the first cycle, but they tend to disappear in the later loops. This undesirable discrepancy was ascribed to the creation of a transfer film of the sliding material on the mating surface, which smoothed the surface and made the sliding behavior more uniform over the two areas with different roughness. At the current stage, this still represents a major challenge and one of the main constraints limiting the possible frictional properties that can be selected for a VFS. Additionally, μ_1 and μ_2 are only marginally different in their initial values, thus the variability of the friction coefficient is low.

However, Figure 2.16 shows that the numerical predictions are in good agreement with the first-cycle experimental response of the systems tested.

Following the cyclic testing of the VFS prototypes in group 1, the manufacturer group

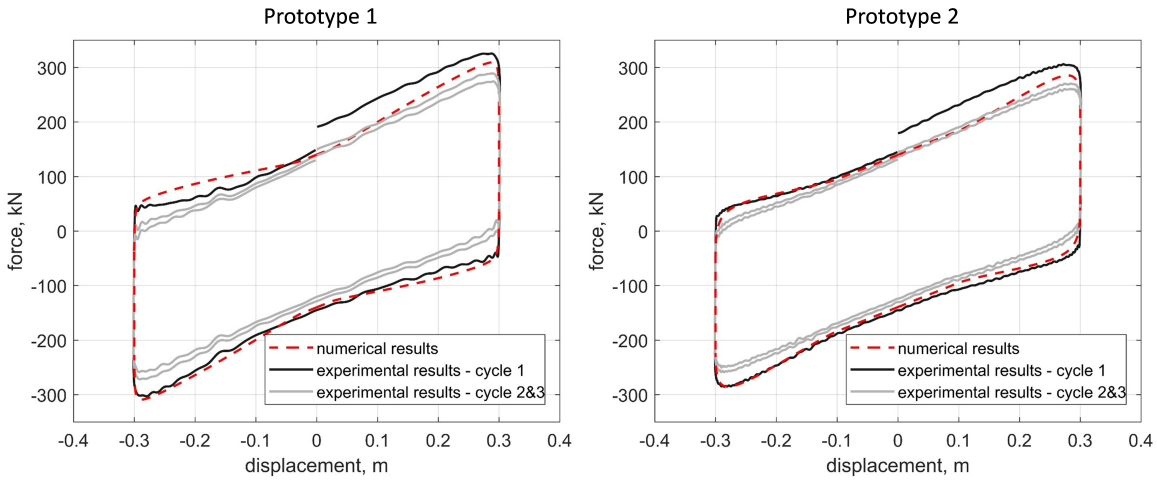

Figure 2.16: Comparison between the hysteretic curves from numerical model and experimental data for group 1 VFS prototypes

addressed the issue of the quality of the low friction material coating, and manufactured the VFS prototype in group 2. The horizontal force-displacement response characterizing the group 2 VFS prototype under realistic ground motions is reported in Figure 2.17. The black dashed lines represent the experimental results, while the grey solid lines represent the numerical prediction. The numerical predictions are in good agreement with the experimental results. This outcome is very promising and suggests that the numerical element implemented captures the mechanics of VFSs adequately, in the context of time history analyses. However, to further validate the numerical element, more experimental evidence (for example, 3-D testing) is needed.

The response predictions outlined in Figure 2.16 and Figure 2.17 were obtained modeling the friction coefficient as velocity-dependent. Pressure-dependency was neglected because the axial force remained approximately constant throughout the tests. The relationship between the sliding velocity and the coefficient of friction can be described by the exponential function proposed by Mokha et al. [1988], shown in Equation (2.37):

$$\mu(v) = \mu_{max} \times [1 - (1 - \tilde{\mu}_v)e^{-\alpha v}] \tag{2.37}$$

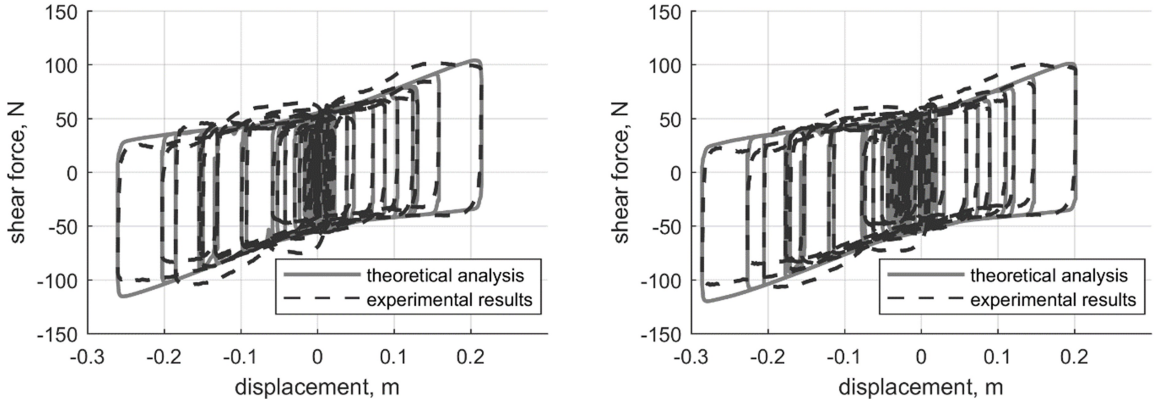

Figure 2.17: Comparison between the hysteretic curves from numerical model and experimental data for group 2 VFS prototype

where $\mu(v)$ represents the coefficient of friction as a function of sliding velocity, μ_{max} is the coefficient of friction at high sliding velocity, $\tilde{\mu}_v$) is the ratio between the coefficient of friction at slow sliding velocity and μ_{max}, and α is a constant describing the transition rate between the coefficient of friction from low to high sliding velocity. Past studies suggest that the value of the coefficient α can range from 20 sec/m to over 100 sec/m depending on the low friction material utilized Constantinou et al. [1999]. In the present work, it was found that setting α equal to 20 sec/m provided the best match between the experimental results and the numerical predictions. The parameter $\tilde{\mu}_v$) was set equal to 0.5, which is consistent with past studies Fenz and Constantinou [2008a].

It should be noted that there are other friction models that users can choose from when modeling VFSs in OpenSees (e.g. the multi-linear friction model for capturing the break-away effect). However, these were not considered in the analyses, a detailed study of the effect of different friction models on the VFSs' behavior and the sensitivity to the corresponding frictional parameters is part of the future work.

2.5 Chapter Conclusions

This Chapter presented the formulation and OpenSees implementation of a 3D VF element that is capable of capturing the full static and dynamic response of VFSs. Initial comparison of the newly developed element was conducted between the results of numerical simulations and the experimental results collected from testing a full-scale VFS prototype under uni-directional shaking. The numerical results showed good agreement with the experimental data. The extension to the 3D model was solely based on principles of mechanics as no 3D experimental evidence is yet available. However, an initial verification of the 3D algorithm was performed analyzing standard FP systems via the new element and the element readily available in OpenSees. The results of these analyses showed perfect match, suggesting that the VFS algorithm was implemented correctly. Nonetheless, without a full (3D) experimental validation, researchers should remain cautious when performing 3D analyses using the newly implemented model.

The results of NLTH analyses were used to verify an important design assumption, which is, if carefully designed, the behavior of a VFS can be simplified using a multi-linear model. This is of great benefit from a preliminary design standpoint, because it is much simpler to perform the bearing design steps referring to a multi-linear than to a highly non-linear hysteretic response.

Preliminary 2D and 3D numerical analyses of a 5-story 1-bay case study building selected from the OpenSees library of examples analyzed under 2D and 3D motions were also performed. The case study buildings were base-isolated using the newly implemented VF element. These analyses served primarily to demonstrate the use of the new element in the context of NLTH analyses, and to confirm the correct implementation of the element into OpenSees.

Furthermore, the results collected showed that, as the design parameter β decreases, the maximum base shear and the maximum displacement at the bearing level tend to decrease, while maintaining the residual displacement within reasonable ranges. This trend held for

all the systems analyzed, with the exception of the VFS with β set equal to -1.0, which showed poor overall performance. While these results are consistent with the findings of simplified VFS studies conducted in the past, extensive numerical parametric investigations and 3-D full-scale bearing and shake table tests, as part of future work, are necessary before any definitive conclusions on the performance of VFSs can be drawn.

Chapter 3

A SPECIAL CASE: ADAPTIVE VARIABLE FRICTION SYSTEM

The previous chapter described the development and implementation of a numerical element that is capable of capturing the hysteretic behavior of VFSs. This chapter focuses on a special case of VFSs, namely, the Adaptive Variable Friction Pendulum System (AVFS). The AVFS is one type of VFSs that provides passive-adaptive behavior.

This chapter first extends the background from Chapter 1 with a more detailed description of the AVFS. Then it provides a simplified procedure of analyzing AVFS-isolated structures. Finally, it presents an extensive parametric study aiming to evaluate how various parameters of the AVFS affect its performance.

3.1 Chapter Introduction

The use of sliding isolation devices, such as Friction Pendulum Systems (FPSs), has been shown to be effective in mitigating seismic effects on both structural and non-structural components. However, it is a well-known dilemma that FPSs can only be designed for one hazard level [Fenz and Constantinou, 2008d]. ASCE [2017] requires that FPSs (and other base isolated systems) should be designed to maximum considered event (MCE). In this case, their performances for more frequent earthquakes (for example, SLE and DBE level earthquakes) cannot be controlled, and are likely to be non-optimal.

A possible answer to this challenge is to use "passive-adaptive" devices. In this context, "passive adaptive" refers to systems in which the stiffness changes at designed levels of lateral displacement. The primary benefit of this type of response is that isolation systems can be designed to optimize multiple performance objectives for multiple levels of ground shaking.

Variable Friction Systems, by changing friction coefficient at designed levels of lateral displacement, can exhibit this type of stiffness change, thus to achieve "passive-adaptive" behavior. In this dissertation, this type of VFSs is referred as Adaptive Variable Friction Systems (AVFSs).

It should be noted that the AVFS is only one of the many possibilities of VFSs. By careful design of the geometric and frictional properties, other types of potentially advantageous hysteretic responses can be obtained.

3.2 Adaptive Variable Friction Systems

An Adaptive Variable Friction System, as illustrated in Figure 3.1(a), consists of a fixed-base stainless steel spherical cap, defined by radius of curvature, R, and an articulated sliding pad. The spherical cap contains two concentric ring-zones that are characterized by different roughnesses, which is typically achieved by different polishing techniques. The slider is made from stainless steel, coated with a low friction material, such as polytetrafluorethylene [Calvi and Calvi, 2018]. The sliding motion between the sliding pad and the spherical cap is characterized by different coefficients of friction, μ_1 and μ_2 ($\mu_1 < \mu_2$).

The theoretical lateral force-displacement relationship for an AVFS is shown in Figure 3.1. This hysteretic curve shown was calculated assuming that the axial stress is uniform over the sliding area, that there is no difference between static and dynamic friction, and that friction is well defined and perfectly stable. The detailed theoretical formulation of the hysteretic behavior of VFSs was presented in Chapter 2.

3.3 Design of Adaptive Variable Friction Systems

The design of AVFSs adopts the Direct Displacement Based Design (DDBD) framework outlined in Priestley et al. [2007]. The details of applying this framework on base isolated systems can be found in Calvi et al. [2016b]. Chapter 2 also presented the application of this framework on the design of VFSs with smooth backbone curves.

In order to apply this method to the design of AVFSs, it is first important to simplify the

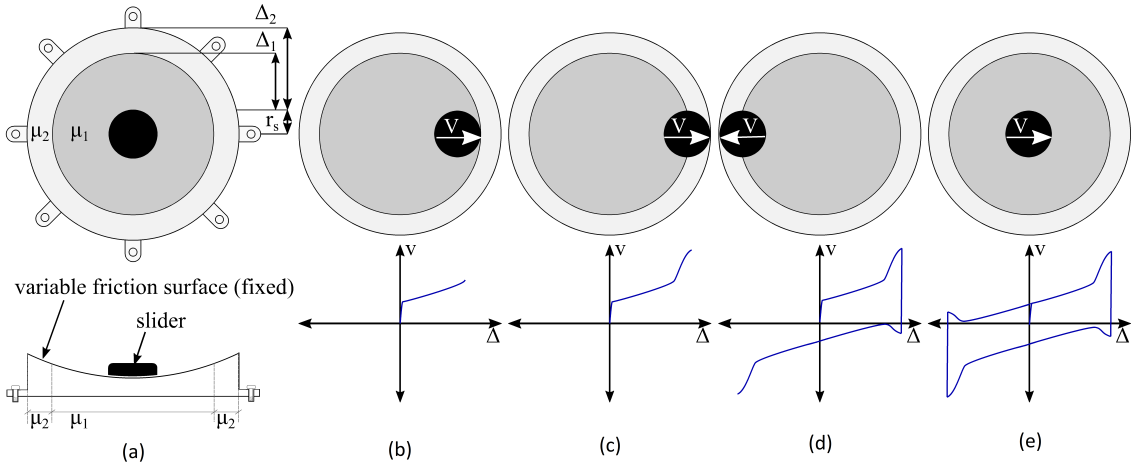

Figure 3.1: (a) Cross-sectional and aerial view of an AVFS device, (b) force-displacement response of AVFSs at post-activation, (c) at maximum displacement, (d) at lateral load reversal, (e) returned to initial position. (Figure modified from Bergquist et al. [2019])

hysteretic response of AVFSs with piece-wise linear curves as shown in Figure 3.2, where Δ_0 represents the bearing activation displacement (usually taken as 0.01 mm, as suggested by Constantinou et al. [1999]), Δ_1 represents the displacement where the sliding pad enters the higher friction zone, Δ_2 represents the design displacement (usually at MCE level), and V_0 to V_2 represent the corresponding shear forces, respectively. Then, it is convenient to define the following design parameters:

$$\begin{aligned} \alpha_1 &= V_1/V_0 \\ \alpha_2 &= V_2/V_0 \\ \gamma &= \Delta_2/\Delta_1 \end{aligned} \tag{3.1}$$

The two essential parameters in the DDBD framework of designing AVFSs, effective natural period, T_n, and effective damping ratio, ζ_{eff}, can then be calculated using Equation (3.2) and Equation (3.3), respectively.

$$T_n = \sqrt{\frac{4W\pi^2\Delta_2}{V_2 g}} \tag{3.2}$$

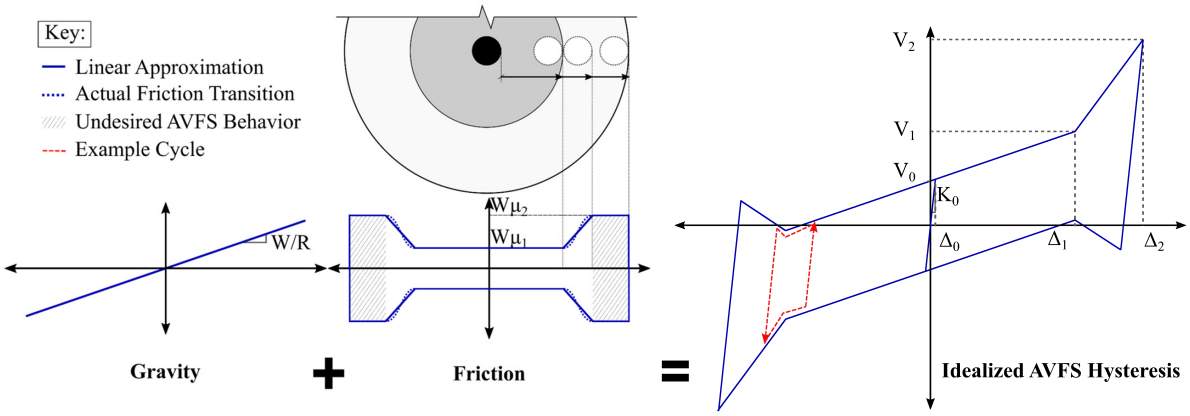

Figure 3.2: Components of hysteresis and idealized hysteretic response of AVFSs used for design (Figure modified from Bergquist et al. [2019])

$$\zeta_{eff} = \frac{\alpha_2 * (\gamma - 1) + \gamma(\gamma + \alpha_1 - \gamma\alpha_1) + 1}{\pi\alpha_2\gamma} \tag{3.3}$$

Given the design parameters from the simplified piece-wise linear model, realistic properties of an AVFS (geometric and frictional) can be calculated using the following equations.

$$\begin{aligned} \mu_1 &= \frac{4\pi^2 W}{\alpha_2 T_n^2 g^2}\Delta_2 \\ R &= \frac{\mu_1 \Delta_1}{\alpha_1 - 1} \\ r_1 &= r_0 + \Delta_1 \\ r_2 &= r_0 + \Delta_2 \end{aligned} \tag{3.4}$$

It should be noted that, as illustrated in Figure 3.2, the stiffening part of the hysteresis is provided by the transition of the sliding pad moving from the low friction ring-zone to the high friction ring-zone. The distance of this transition equals to the diameter of the sliding pad. Thus, its radius, r_0, should be designed to have a lower bound of $\frac{1}{2}(\Delta_2 - \Delta_1)$. The friction coefficient between the sliding pad and the high friction ring-zone, μ_2, can be calibrated using the closed-form force-displacement relationship such that it provides minimum norm-2 error between the nonlinear model and the piece-wise linear model.

It is worth mentioning that, for FPSs and VFSs with smooth backbone curves (as described in Chapter 2), there is only one set of design parameters given a pair of T_n and ζ_{eff} at a targeted level earthquake. Therefore, the performance of the structural system at other hazard levels cannot be controlled. On the contrary, for AVFSs, due to the stiffness change at Δ_1, there are unlimited sets of design parameters (i.e., α_1, α_2, and γ) that could achieve the same pair of T_n and ζ_{eff} at a targeted level earthquake. This versatility allows the structural system to achieve multiple performance goals at various levels of earthquake. To shed light on the effect of these design parameters on the performance of AVFSs and its supported superstructure, the next section presents an extensive parametric study of AVFS-isolated 3-story and 9-story steel braced frame buildings.

3.4 Numerical Simulations

This section aims to investigate how the performance of an AVFS-isolated building is affected by its design parameters. Different sets of AVFSs are designed such that the effective period and effective damping ratio of the isolation systems at the median MCE displacement are equal. Four sets of effective isolation properties are considered in this study: two effective periods (3 and 4 s), with two effective damping ratios (10% and 25%), respectively.

The supported superstructure includes three- and nine-story steel concentrically braced frame structures that are designed to be elastic for the median MCE force level. To evaluate the performance of the superstructure, peak inter-story drift (PISD) and peak floor acceleration (PFA) at each hazard level were recorded, as they are the primary indicators for estimating seismic losses [Morgan and Mahin, 2010].

3.4.1 Ground motions

As the objective of this study is to investigate the performance of AVFS-isolated buildings at different hazard levels, three levels of ground shaking are considered, namely, Service Level Event, SLE (return period of 72 years), Design Basis Event, DBE (return period of 475 years), and Maximum Considered Event, MCE (with a return period of 2475 years),

The ground motion records were selected from the SAC Steel Project, in which a total of 60 records (20 at each hazard level) were assembled for the Los Angeles basin. These ground motion records have a wide range of intensities and frequency content, providing an effective mean of evaluating performance of different isolation systems at various hazard levels. A detailed description of these records is presented in Somerville et al. [1998].

3.4.2 Design of AVFSs

All considered AVFSs are designed to have the same effective isolation properties (T_n and ζ_{eff}) based on the median MCE response spectrum from the considered ground motion set. As described in Section 3.3, to achieve the same isolation properties, there exist unlimited sets of design parameters (α_1, α_2, and γ). Based on Equation (3.2) and Equation (3.3), given a pair of T_n and ζ_{eff} values, two out of three design parameters can effectively determine the design of the isolation system.

In this study, α_2 and γ were selected and assigned a wide range of values. By re-arranging Equation (3.3), given α_2 and γ, α_1 can be calculated as follows:

$$\alpha_1 = \frac{\pi\alpha_2\gamma\zeta_{eff} - \alpha_2(\gamma-1) - \gamma^2 - 1}{\gamma(1-\gamma)} \tag{3.5}$$

It should be noted that, the lower bound of α_2 is determined using Equation (3.6), in which case the isolation system represents a traditional FPS [Calvi et al., 2016b]. Theoretically, there is no upper bound of α_2, as it represents the ratio between maximum base shear and initiation shear force. However, to achieve a larger α_2 value, it requires a smaller μ_1 and a larger μ_2 value. In this study, the results of those that have friction coefficients between 1% and 50% are reported. The upper bound of coefficient of friction was chosen beyond what is currently considered practical. However, as the objective of this study is to investigate the effect of design parameters on the performance of VFS isolated structures, it is deemed appropriate to use a large range of bearing properties. The other design parameter, γ, was assigned to range from 1.3 to 2 with an increment of 0.1. For a constant α_2 value, to

achieve the same T_n and ζ_{eff}, a smaller γ value leads to a larger stiffness change (i.e., larger Variable Friction effect), however, requiring a larger μ_2 value. Thus, the lower bound of γ was chosen to avoid unrealistically high μ_2 values, and the higher bound of γ was chosen to ensure meaningful Variable Friction effects.

$$\alpha_2 = \frac{2}{\pi\zeta_{eff}} \tag{3.6}$$

Finally, knowing the design parameters, the geometric and frictional properties of the isolation systems can be calculated using Equation (3.4).

3.4.3 Design of Superstructure

For each isolation system considered, three- and nine-story steel concentrically braced frame (SCBF) shear-type buildings were designed. The superstructures were designed assuming $R_I = 1$, with targeted elastic behavior based on the median MCE response spectrum. This follows the design provisions of ASCE [2017]. For each superstructure, the floor mass was arbitrarily set to unity. The shear spring between each floor was designed to have a yield inter-story drift ratio, θ_y, of 0.003 rad [Morgan and Mahin, 2011]. These design choices are based on the assumption that, for a particular structural system, the yield displacement is independent of its strength [Priestley, 1998].

The design of story stiffness followed the equivalent lateral force procedure outlined in ASCE [2017]. In brief, the design base shear was calculated from the effective properties of the isolation system considering the MCE median spectrum. This base shear was then converted to a lateral force distribution based on Section 17.5.5 of ASCE [2017]. The resulting story shear forces were considered as the yield shear force, v_{yi}, where i represents the story level. Assuming a story height, h_i, of 144 in, the story stiffness can be calculated using Equation (3.7).

$$k_i = \frac{v_{yi}}{\theta_y h_i} \tag{3.7}$$

Using the story stiffness, the global stiffness matrix of the superstructure was then assembled.

Table 3.1: Summary of the first three natural periods of the three-story building.

Mode	$T_n = 3$ sec		$T_n = 4$ sec	
	$\zeta_{eff} = 10\%$	$\zeta_{eff} = 25\%$	$\zeta_{eff} = 10\%$	$\zeta_{eff} = 25\%$
1	0.53	0.58	0.70	0.77
2	0.22	0.23	0.29	0.29
3	0.14	0.15	0.18	0.19

Table 3.2: Summary of the first three natural periods of the nine-story building.

Mode	$T_n = 3$ sec		$T_n = 4$ sec	
	$\zeta_{eff} = 10\%$	$\zeta_{eff} = 25\%$	$\zeta_{eff} = 10\%$	$\zeta_{eff} = 25\%$
1	0.83	0.94	1.10	1.24
2	0.34	0.35	0.43	0.45
3	0.21	0.22	0.27	0.28

In combination with the global mass matrix, the natural periods of the superstructure were calculated using eigenvalue analysis.

The lateral force distribution equations provided by ASCE [2017] are functions of the superstructure's first period. However, this period value cannot be determined until the assembly of the stiffness matrix. Thus, the above described process becomes iterative. To start this iteration process, an approximation of the superstructure's first period is calculated using Equation (3.8), where H represents the total height of the superstructure, C_t and x are design parameters that depend on the type of the structural system (0.03 and 0.75, respectively, for SCBF) [ASCE, 2017].

$$T_{n,initial} = C_t H^x \tag{3.8}$$

The resulting superstructure properties are summarized in Table 3.1 and Table 3.2.

3.4.4 Numerical modeling

Numerical models of the shear-type case study structures isolated with AVFSs were built in OpenSees. The solution algorithm employed within the NLTHA cosisted of Newmark's method, with constant average acceleration, and the Newton-Raphson iteration scheme.

A two-ring VF element was used to numerically model AVFSs. In addition to the geometric and frictional properties obtained from the design procedure, the bearings were assigned a compressive stiffness calculated to achieve a vertical period of vibration of the structure of 0.03 s [Warn and Ryan, 2012]. The initial stiffness of the bearing was calculated such that the bearing activation displacement was 0.01 mm [Constantinou et al., 1999].

The superstructure was modeled as a traditional stick-mass model. Each story was modeled using linear elastic beam and column element. Stiffness-proportional damping was applied to the superstructure where the damping coefficient was computed from the frequency of the base-isolated structure with the post-elastic stiffness of the isolation system at $\zeta = 1\%$. This was applied based on the recommendation provided by Pant et al. [2013]. While alternative damping models may be selected in other circumstances, the effect of damping on the response was similar for all studied systems and therefore did not affect the comparison between the different systems.

3.4.5 Numerical results

For each analysis, maximum displacement, Δ, peak floor acceleration, PFA, and peak inter-story drift, PISD, were recorded. For brevity, only results pertaining to the three-story structure isolated with AVFSs characterized by T_n equals to 3 sec and ζ_{eff} equals to 10% and 25% are presented, as shown in Figure 3.3 and Figure 3.4. Results for other cases are included in Appendix B, they present similar results as the two cases presented in this section.

The results are reported as mean EDPs at each hazard level with respect to α_2 and γ. These results are normalized to the performance of FPSs (i.e. systems with minimum

considered α_2). The blank space shown in the figures represents systems with properties that do not satisfy the following practical constraints: (i) R is positive; (ii) μ_2 is in between 1% and 50%.

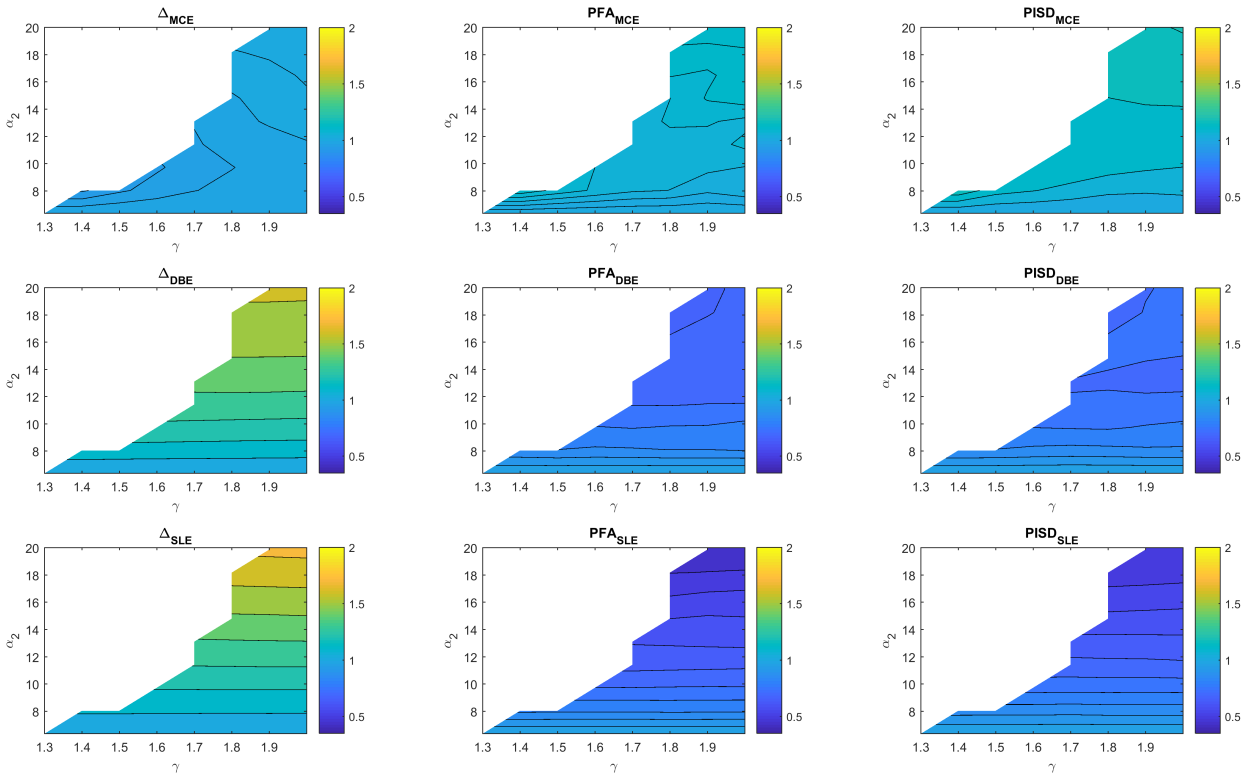

Figure 3.3: Mean demand (of three hazard levels) for Δ_{iso} (left), PFA (center), PISD (right) for three-story isolated buildings with isolation systems that have $T_n = 3$ sec and $\zeta = 10\%$.

The results show that, for both three- and nine-story structures, and for all considered effective isolation system properties, AVFSs are capable of improving the performance of superstructure (i.e. reducing PFA and PISD, by up to 50%) during SLE and DBE, while maintaining approximately the same performance during MCE. However, these improvements are compromised with an increase in the maximum slider displacement (by up to 60%). However, because structural and non-structural damage are mostly correlated to PFA and PISD, and the displacement capacity of the isolation systems is designed to MCE, this trade-off is considered acceptable.

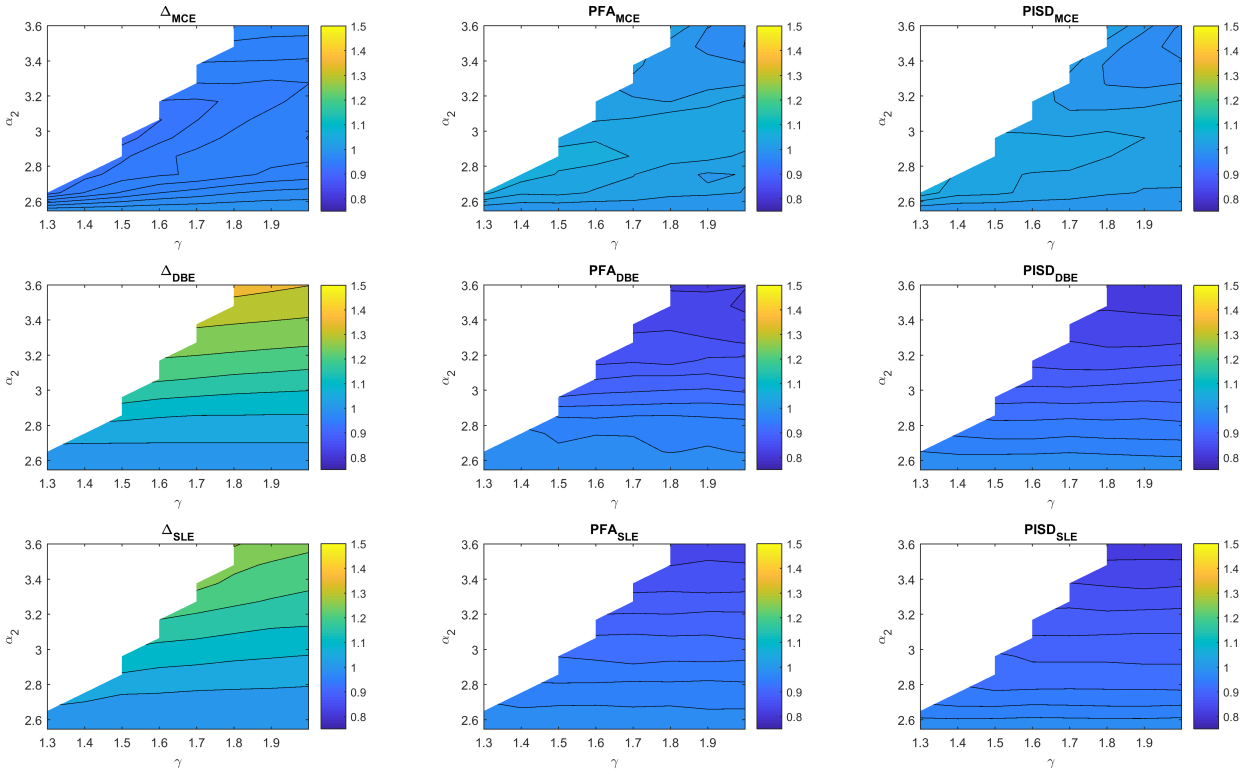

Figure 3.4: Mean demand (of three hazard levels) for Δ_{iso} (left), PFA (center), PISD (right) for three-story isolated buildings with isolation systems that have $T_n = 3$ sec and $\zeta = 25\%$.

It is also shown that, the performance of AVFS-isolated structures is largely affected by α_2, but is lightly affected by γ. As α_2 increases, the reduction of PFA and PISD at SLE and DBE becomes larger, however, it results in a slight increase of PFA and PISD during MCE.

To further illustrate the results, the mean demand hazard curves for each considered EDP are plotted in Figure 3.6 and Figure 3.8, comparing the performance between FPSs and an example AVFS. The theoretical hysteretic responses of the selected FPS and AVFS are shown in Figure 3.5 and Figure 3.7, and the bearing properties are summarized in Table 3.3 and Table 3.4. It should be noted that the value r_2 for AVFSs (equivalent to r_1 for FPSs) was arbitrarily assigned a large value.

The results from these individual cases show that, in comparison to FPSs, AVFSs are capable of improving the performance of the superstructure at more frequent earthquakes,

while maintaining similar performance levels for rare events. In particular, for the three-story isolated buildings with isolation systems that have $T_n = 3$ sec and $\zeta = 10\%$, AVFSs leads to a reduction of 35% for both PISD and PFA in SLE, and a reduction of 27% for both PISD and PFA in DBE. However, it has an increase of 10% for PISD and 7% for PFA at MCE. For the three-story isolated buildings with isolation systems that have $T_n = 3$ sec and $\zeta = 25\%$, while achieving approximately the same performance for MCE, AVFSs have a reduction of approximately 20% in PISD and PFA for both SLE and DBE.

Table 3.3: Bearing properties for example FPS and AVFS for three-story isolated building with isolation systems that have $T_n = 3$ sec and $\zeta = 10\%$.

System	Design properties		Realistic bearing properties					
	α_2	γ	R (in)	r_0 (in)	r_1 (in)	r_2 (in)	μ_1	μ_2
AVFS	13.12	2	147	23.25	38.75	100	0.03	0.37
FPS	6.37	N/A	105	23.25	100	N/A	0.06	N/A

Table 3.4: Bearing properties for example FPS and AVFS for three-story isolated building with isolation systems that have $T_n = 3$ sec and $\zeta = 25\%$.

System	Design properties		Realistic bearing properties					
	α_2	γ	R (in)	r_0 (in)	r_1 (in)	r_2 (in)	μ_1	μ_2
AVFS	3.59	2	331	17.4	29	100	0.09	0.43
FPS	2.55	N/A	145	17.4	100	N/A	0.10	N/A

3.5 Conclusions

This chapter presented AVFSs as passive adaptive devices. It investigated the effect of various design parameters of AVFSs on the demands on the superstructure at different hazard levels through an extensive parametric study.

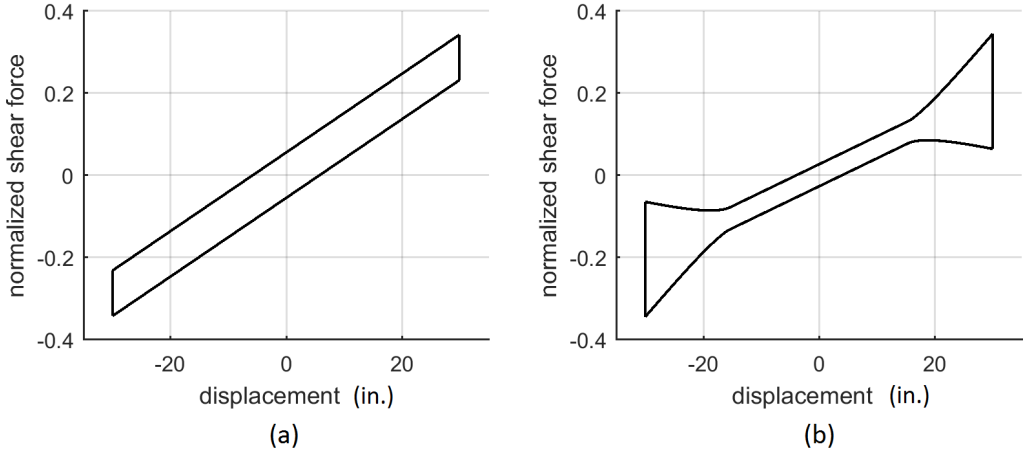

Figure 3.5: An example of the theoretical hysteresis comparison between FPSs and AVFSs for three-story isolated buildings with isolation systems that have $T_n = 3$ sec and $\zeta = 10\%$.

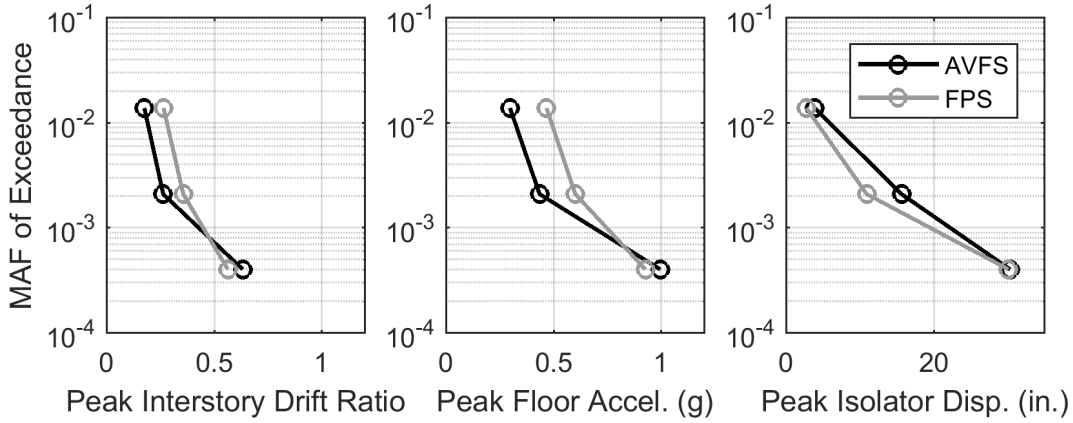

Figure 3.6: An example of the comparison between FPSs and AVFSs of mean demand hazard curves for Δ_{iso} (left), PFA (center), PISD (right) for three-story isolated buildings with isolation systems that have $T_n = 3$ sec and $\zeta = 10\%$.

Both stiff and flexible superstructures (three- and nine-story steel concentrically braced frame building) were considered in this study, each with moderate/long period (3 and 4 s) and high/low damping (25% and 10%) isolation systems.

For all considered cases, the investigated isolation systems were designed to have the

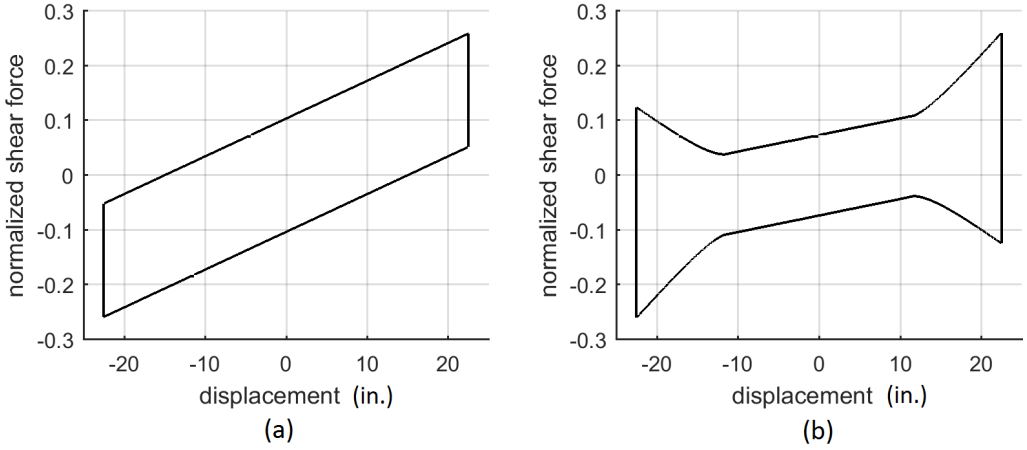

Figure 3.7: An example of the theoretical hysteresis comparison between FPSs and AVFSs for three-story isolated buildings with isolation systems that have $T_n = 3$ sec and $\zeta = 25\%$.

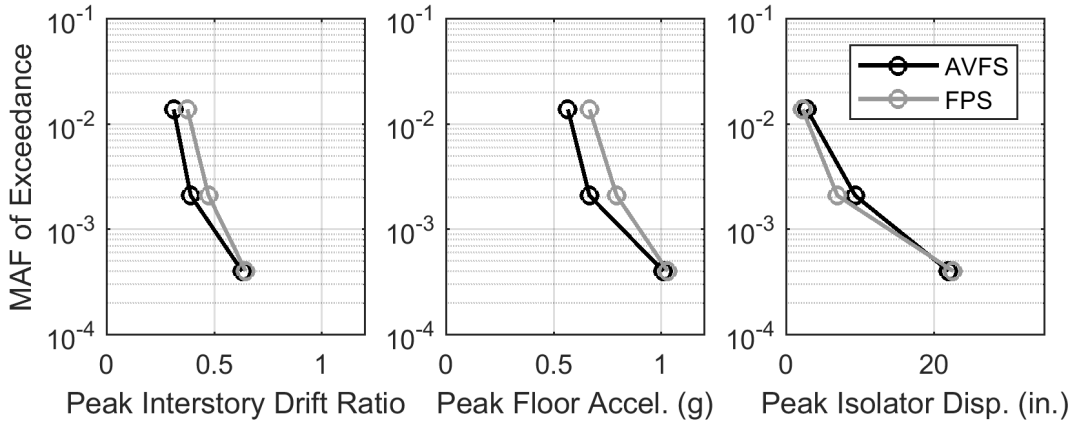

Figure 3.8: An example of the comparison between FPSs and AVFSs of mean demand hazard curves for Δ_{iso} (left), PFA (center), PISD (right) for three-story isolated buildings with isolation systems that have $T_n = 3$ sec and $\zeta = 25\%$.

same effective isolation properties (T_n and ζ_{eff}). In comparison to FPSs, AVFSs are capable of improving the superstructure performances (reducing PISD and PFA) for frequent earthquakes (both SLE and DBE), while maintaining similar performance during rare events (MCE).

For AVFS-isolated structures, when α_2 increases, the PISD and PFA during frequent earthquakes decrease. However, a large α_2 could result in increased PISD and PFA during rare events. The other design parameter, γ, showed little effect on superstructure performance.

While the results demonstrate the capability of AVFSs to improve the demands on the superstructure. There is a trade-off between maximum isolator displacement and superstructure performance (i.e., peak interstory drift and peak floor acceleration) under different hazard levels. In practice, it would be the building owner's choice on a case-by-case basis to evaluate and mitigate the damage in buildings over a wide range of seismic hazard levels. The objective of this study is to provide a base isolation system (AVFS) whose performance can be designed under multiple hazard levels, and to shed light on how the performance are affected by its design parameters.

Chapter 4

USING VARIABLE FRICTION ELEMENT TO MODEL EXTREME BEHAVIOR OF CURVED SURFACE SLIDER DEVICES

Note: This study was conducted in collaboration with the University of Pavia and EU-CENTRE. Part of this chapter is modified based on Furinghetti et al. [2020]

Chapter 2 outlined the development and implementation of the Variable Friction element. Chapter 3 explored the use of VFSs as passive-adaptive devices. This chapter focuses on another application of the Variable Friction element: modeling the extreme behavior of Curved Surface Slider (CSS) devices, particularly when the displacement exceeds the maximum design displacement value (referred to as the extra-stroke behavior in this chapter).

This chapter first extends the background from Chapter 1 with a more detailed description of CSS devices. Then it discusses the Variable Friction nature of the extra-stroke behavior of CSS devices. It also includes experimental tests of CSS devices when subjected to extreme ground motion input. Finally, it presents numerical comparison with experimental results of using VF element to model the extra-stroke behaviors of CSS devices.

4.1 Chapter Introduction

Despite the many advantages base-isolation technology can offer, recent risk assessment studies have shown that, in comparison to fixed-base structures, base-isolated structures may be affected by higher vulnerability [Cardone et al., 2019]. It is believed that this somewhat surprising outcome can be (at least partly) attributed to the strict definition of collapse that is typically adopted for base-isolated structures. Base-isolated structures are assumed to

collapse once the design displacement is reached at the base isolation layer. However, this assumption was proven to be overly conservative by recent experimental programs [Furinghetti et al., 2019]. These tests showed that, CSS devices, both with and without restraining rims, can achieve higher displacement capacity than the design displacement value. The tests also showed that, for CSS devices with restraining rims, when the sliding pad traveled beyond design displacement, it exhibited higher energy dissipation capacity. In fact, the CSS device serendipitously became a Variable Friction System. When the sliding pad traveled across the rim, part of it was travelling on a high-friction ring zone.

In order to investigate the performance and modeling method of CSS devices with extra-stroke behaviors, a recent experimental program was conducted at the EUCENTRE Foundation Laboratory in Pavia (Italy). A series of full-scale CSS devices were tested under several input motions, with peak displacement demands exceeding the design values. These results were then used to evaluate the accuracy of using VF element to model the extra-stroke behaviors of CSS devices.

This study was conducted in collaboration with the University of Pavia and EUCENTRE. The experiments were designed and performed by researchers at the University of Pavia and lab technicians at the EUCENTRE Foundation Laboratory. The numerical analyses were performed by researchers at the University of Washington.

4.2 Test Isolation Devices

The CSS devices tested in this program consist of one (Single) or two (Double) stainless steel spherical surfaces and a slider that is coated with low-friction material, such as Teflon (PTFE) or polyethylene (PE) [Dolce et al., 2005; Fenz and Constantinou, 2006]. The main properties of the tested devices are summarized in Table 4.1.

The tested devices are grouped by type as follows:

- Type #1: the stainless steel sliding surface is installed into a counterbore of the housing plate, thus a gap is originated between the sliding interface and the outer rim of the

plate.

- Type #2: the stainless steel sliding surface is installed by means of a weld bead, so that a unique solid element is created, and no replacement of the sliding interface is generally possible.

Table 4.1: Properties of the tested devices

Device #	Type #	Sliding material	R	μ	# of sliding surfaces
1	1	Filled PTFE	3.0	0.05	2
2	1	ULDPE	3.0	0.03	2
3	1	Vergin PTFE	3.0	0.01	2
1	2	PTFE based material	3.0	0.05	1
2	2	PTFE based material	5.5	0.05	2
3	2	PTFE based material	4.2	0.05	1

The difference between Type #1 and Type #2 devices is schematically outlined in Figure 4.1. In both cases, the sliding pad can travel past the design displacement (i.e. the nominal capacity) of the device. However, some extent of damage to the slider is expected to occur on the loading cycle for Type #1 bearings, and on the returning cycle for Type #2 bearings.

4.3 Test Protocol

Quasi-static and dynamic tests were performed considering triangular and sinusoidal forces, as shown in Figure 4.2. Table 4.2 provides a summary of the test protocols.

It should be noted that Type #2 devices achieved much higher peak velocities. However, its velocity varies harmonically with respect to time, whereas the triangular waveform has constant velocity.

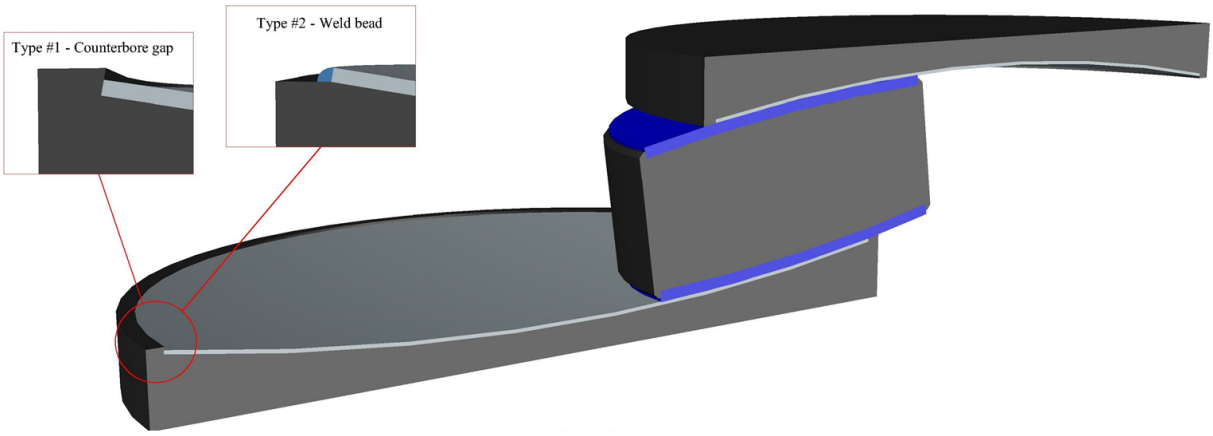

Figure 4.1: Example of tested device typologies.

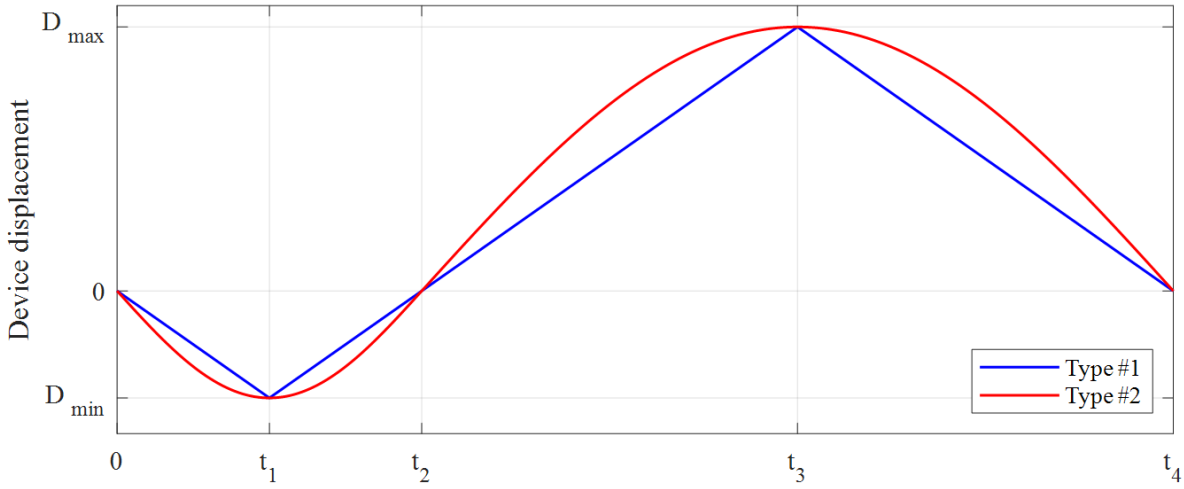

Figure 4.2: General waveforms used for tests.

The maximum displacement demand, D_{max}, of each test was computed considering a displaced configuration of the device with 25% of the inner pad uncovered by the sliding interface for vertical stability. When DCSS devices are used, higher displacement demands can be achieved because two sliding surfaces are engaged.

Table 4.2: Properties of the tested devices

Device #	waveform	D_{max}/D_d	V_{max} (mm/s)
1	triangular	1.52	2.5
2	triangular	1.52	2.5
3	triangular	1.52	2.5
4	Sine	1.28	15.0
5	Sine	1.27	15.0
6	Sine	1.29	15.0

4.4 Experimental Results

The hysteretic responses of all Type #1 devices are reported in Figure 4.3. Both horizontal forces and displacements are normalized with respect to the design values. It can be seen that beyond the nominal capacity, the force-displacement response experiences an initially smooth increase in stiffness (over a short distance), followed by stiffness "stabilization" at a value which is very close to the expected restoring stiffness of the device, computed as the ratio between the applied vertical load and the equivalent radius of curvature.

At the end of all the tests on Type #1 devices, the sliding material presented significant damage, with large portions of the low-friction material detached from the slider (see Figure 4.6).

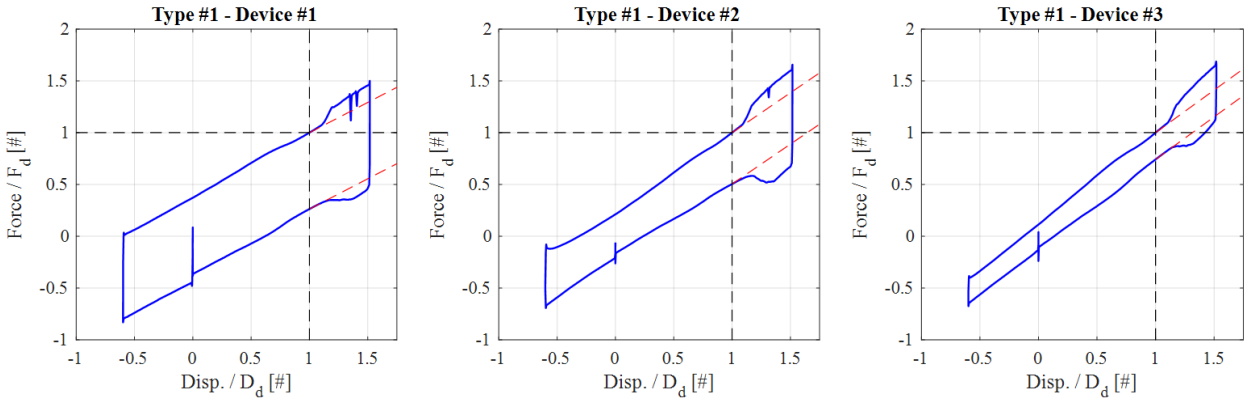

Figure 4.3: Experimental results: Normalized hysteretic loops for Type #1.

The results summarized in Figure 4.3 suggest that exceeding the design displacement of the device leads to an increase of the friction coefficient, if the stainless steel sliding surface is installed into a counterbore gap. In order to better highlight such aspect of the response, the "pure friction" behavior of the devices was isolated, by subtracting the re-centering force (modeled linearly with respect to the applied displacement time series) from the total force of the devices. The normalized response of the devices attributed solely to friction is shown in Figure 4.4. In all cases the responses are approximately symmetric with respect to the displacement-axis, suggesting that the same friction coefficient is mobilized upon loading and unloading. Interestingly, the friction coefficient increased by 33% for Device #1 (nominal value 5%), and by 100% for both Devices #2 and #3 (nominal friction values 3% and 1%, respectively).

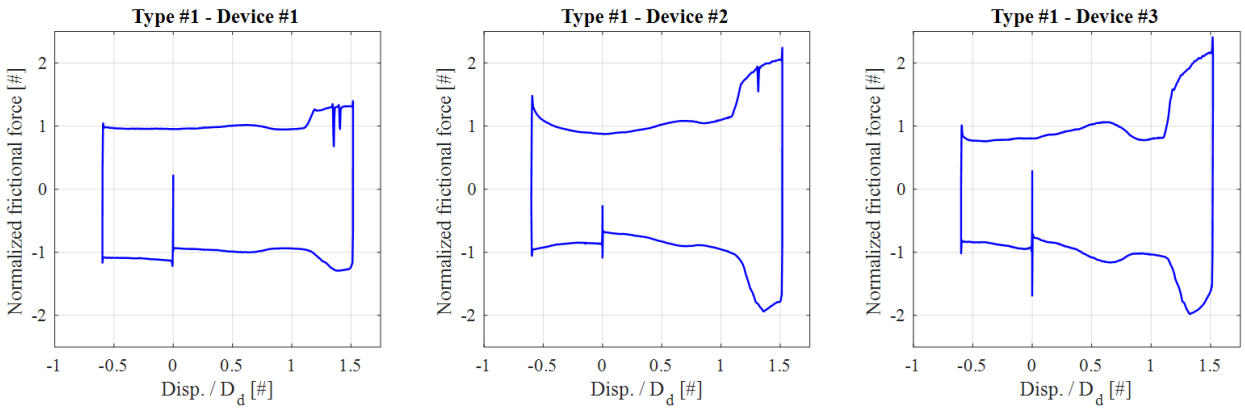

Figure 4.4: Experimental results: Normalized frictional response for Type #1.

The hysteretic responses obtained for all Type #2 devices are presented in Figure 4.5. Unlike what seen for the Type #1 devices, no significant variation in the "post-design" force-displacement response can be detected for devices #4, #5 and #6. To this end, it can be seen that their tangent stiffness remains essentially constant and very close to the elastic stiffness value estimated from the pendulum motion. Hence, it appears that when the inner slider exceeds the nominal displacement capacity of Type #2 devices, "ordinary" response

of the CSS device is to be expected at all displacement levels. This is because the weld bead provides a smooth transition of the sliding motion at the maximum deformation allowance, with negligible damage of the sliding material.

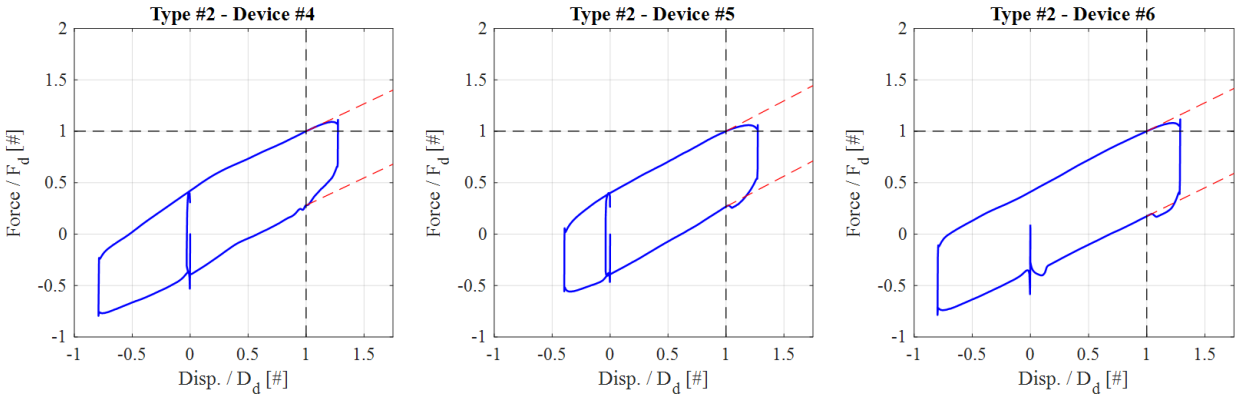

Figure 4.5: Experimental results: Normalized frictional response for Type #2.

Figure 4.6 provides a view of the status of the sliding pads at the end of each test. As anticipated, different extent of damage was detected for Type #1 and Type #2 devices. More specifically, significant damage of the slider can be observed pertaining to all Type #1 devices, whereas the damage is very limited for the Type #2 devices. The greater extent of damage detected for the Type #1 specimens was attributed to the presence of the counterbore gap, which contributed to cutting and slicing portions of the sliding material. However, for both the isolation typologies studied, the overall force-displacement responses appeared stable at all displacement levels.

4.5 Numerical Simulation

As shown in the experimental results, Type #1 devices present a variation in the force-displacement response, which can be associated to an increased value of friction coefficient when the slider moves beyond the design displacement. To model CSS devices with extra-stroke behavior, one can use 3-ring VFSs where μ_1 represents the friction coefficient between the slider and the sliding surface of the CSS devices, μ_2 represents the effective friction

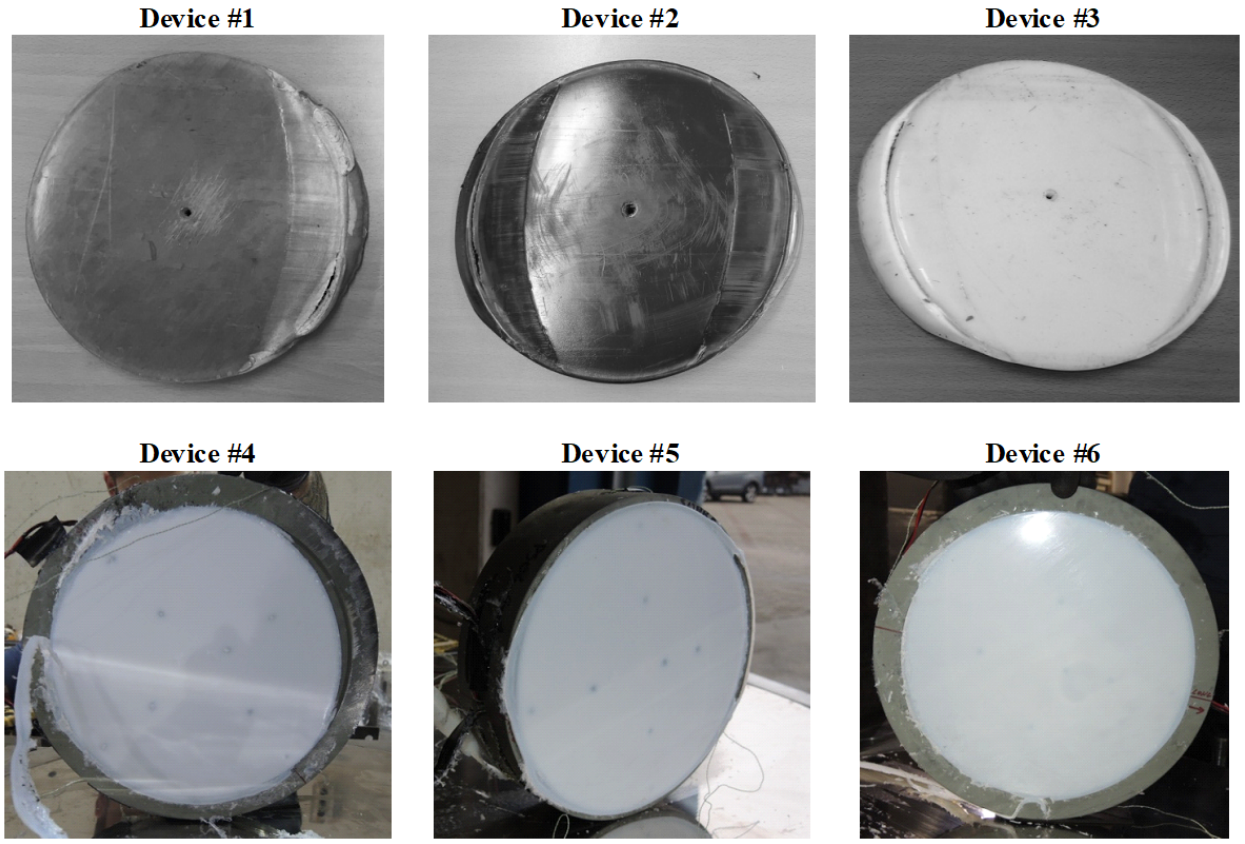

Figure 4.6: Damaged sliding pads.

coefficient between the slider and the edge of the sliding surface as the slider travels beyond the low friction sliding surface, and μ_3 represents the friction coefficient between the slider and air (i.e. approximately zero).

It should be noted that the Type #2 devices considered in this experimental program can be modeled as a traditional Friction Pendulum System or Double Friction Pendulum System, because their response is unaffected by the sliding pad exceeding the nominal displacement capacity.

Table 4.3 shows the key properties of VFSs that were used to numerically model the CSS devices with extra-stroke behavior for all Type #1 devices. The hysteresis comparisons are presented in Figure 4.7. It is shown that the Variable Friction element is capable of capturing

Table 4.3: Properties of the tested devices

Device #	μ_1	μ_2	μ_3	r_0	r_1	r_2	r_3
1	0.05	0.12	0.001	0.13	0.38	0.45	1
2	0.03	0.12	0.001	0.13	0.38	0.45	1
3	0.01	0.07	0.001	0.13	0.38	0.45	1

the extra-stroke behavior of CSS devices.

Theoretically, the value of r_3 is unlimited. Its value is considered appropriate for the numerical model so long as it provides enough displacement capacity for the sliding motion (i.e. $D_{max} < r_3 - r_0$).

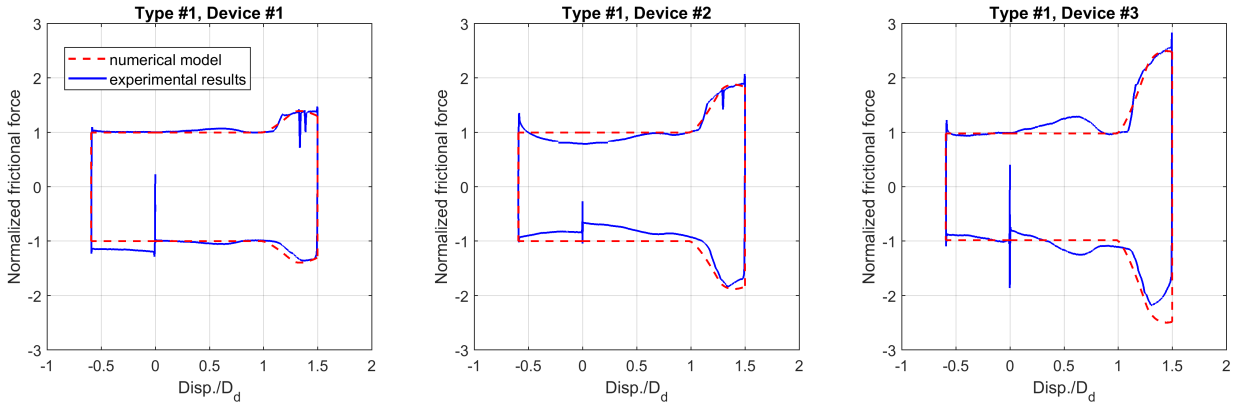

Figure 4.7: Analytical simulation comparison for device Type #1.

4.6 Chapter Conclusions

This chapter summarized the experimental results and numerical modeling of CSS devices under extreme loading conditions. Quasi-static tests and dynamic tests were conducted on several full-scale devices. It is verified that the Variable Friction element is capable of modeling the extra-stroke behavior of CSS devices. The key findings of this chapter is summarized as follows:

- Curved Surface Slider devices without restraining rims can achieve displacements that exceed the design values, without evident negative effects on the force-displacement response and the re-centering properties.

- When the stainless steel sliding surface is installed with a counterbore gap, a force increase (attributed to higher friction) is seen as the sliding pad exceeds the design displacement. However, damage were observed at the end of the tests.

- Reaching design displacement does not represent the failure condition of the isolation devices. Extra displacement capacity may be considered when designing/assessing these devices, depending on both the actual size of the sliding pads and the number of sliding surfaces.

- In case of counterbore gap technology, it is possible to model the extra displacement behavior by using the Variable Friction element described in Chapter 2, which captures the higher friction coefficient that arises when the design displacement is exceeded.

PART II: IMPACT OF CASCADIA SUBDUCTION ZONE MOTIONS ON FRICTION PENDULUM SYSTEMS

Chapter 5

IMPACT OF SIMULATED M9 CASCADIA SUBDUCTION ZONE MOTIONS ON THE PERFORMANCE OF FRICTION TYPE BASE ISOLATED STRUCTURES

Note: This chapter is a reproduction of Yang et al. [2019b]

This Chapter presents the performance of friction type bearings, in particular, Friction Pendulum Systems (FPSs) and Double Concave Friction Pendulum (DCFP) systems with symmetric geometric and frictional properties, subjected to the simulated M9 motions, when designed based on current design spectrum or modified spectra based on previous studies.

5.1 Chapter Introduction

Based on geological evidence, the Cascadia Subduction Zone (CSZ) is capable of generating megathrust earthquakes up to magnitude 9 (M9), such events may severely impact the Pacific Northwest (PNW) of the United States. In addition, many cities in the Pacific Northwest are underlain by a deep sedimentary basin that is known to amplify ground-motion intensity [Frankel et al., 2018].

Results from numerical simulations have indicated that this type of earthquake may be particularly detrimental for structures characterized by fundamental period of vibration of 1.0 second or larger [Marafi et al., 2019]. More specifically, the results of analyses conducted on a large set of single-degree-of-freedom (SDOF) structures with various combinations of strength and ductility subjected to simulated M9 motions, showed that the deformation demands and the collapse likelihood for "flexible" (i.e. long period) structures are significantly larger than those obtained considering a "traditional" risk-targeted maximum considered event (MCE_R) that do not consider the effects of the basin.

This finding may be particularly relevant for base isolated structures. Base isolation systems are often used to control the displacement and acceleration response of the superstructure, and thus mitigate the damage caused by the strong motions. Base isolated structures tend to be characterized by effective periods of vibration larger than 1.0 second. However, such systems have not been included in the studies conducted thus far, and the effects of the M9 earthquake on their performance and vulnerability remain unclear.

To provide insight into the response of base isolated structures to the simulated M9 earthquakes, this chapter presents the results of nonlinear time history analysis (NLTHA) conducted on a large set of SDOF systems that represent the hysteretic behavior of FPSs and DCFP systems characterized for effective periods ranging from 1.5 to 5.0 seconds. These SDOF structures were designed based on either code-required design spectra or modified design spectra for MCE_R hazard level for downtown Seattle area based on previous studies, in particular, the following four spectra were chosen for this study.

- MCE_R design spectrum based on NEHRP 2015 [NEHRP, 2015], denoted as MCE_R, which does not account for the basin.
- Uniform hazard spectrum without any basin amplification factors (computed using the USGS NSHMP Code 2018 [USGS, 2018], denoted as UHS.
- Uniform hazard spectrum with Campbell and Bozorgnia [Campbell and Bozorgnia, 2014] basin amplification factors (calculated assuming $Z_{2.5} = 7$ km), denoted as UHS CB14.
- Uniform hazard spectrum with M9 basin amplification factor [Marafi et al., 2019], denoted at UHS M9 BAF.

Fig. 5.1 shows the response spectra for the four design spectra considered in this study. It should be noted that the basin effects mainly affect spectral accelerations at long periods (> 1 second).

The main goal of this study is to evaluate the performance of the friction type bearings, in particular, FPSs and DCFP systems, during an M9 earthquake, when designed based on the

above four response spectra. Maximum displacement is chosen as the parameter of interest for this study as it is the engineering demand parameter that is most directly related to the failure of base isolation systems and its strong correlation to the maximum base shear.

5.2 Theoretical Study

5.2.1 Design Spectra

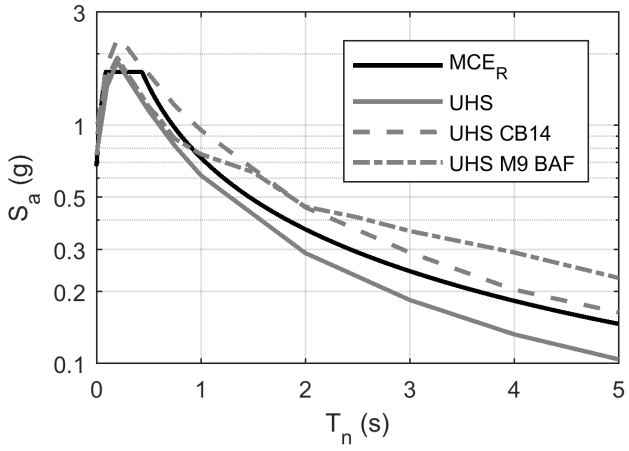

Figure 5.1: The design spectral accelerations with respect to the fundamental period of the structure (T_n) for the risk-adjusted maximum considered earthquakes (MCE_R), uniform hazard spectrum (UHS), uniform hazard spectra with CB14 basin amplification factors (UHS CB14), and uniform hazard spectrum with basin amplification factors derived from the M9 CSZ simulations (UHS M9 BAF).

The risk-targeted maximum considered earthquake spectra (shown as a solid black line in Fig. 5.1) is used to estimate the seismic demands of most structures in the US [NEHRP, 2015]. However, this MCE_R spectra is only an approximation of the uniform hazard spectra (UHS) and only matches the uniform hazard at two periods (0.2 s and 1.0 s). While this approximation is considered sufficient for most structural applications, engineers typically use the uniform hazard spectra (shown as a solid grey line in Fig. 5.1) to design and evaluate base isolation systems.

Additionally, the uniform hazard spectra in areas located on deep basins is under predicted because basin effects are not currently considered in the probabilistic seismic hazard code [USGS, 2018] used to generate the national seismic hazard maps used in ASCE 7-16 [ASCE, 2017]. Engineers in the Seattle region have recognized this deficiency [Chang et al., 2014] in the seismic hazard and have amplified the UHS using basin amplification factors (dashed grey line shown in Fig. 5.1). These basin amplification factors were computed using the Campbell and Bozorgnia [Campbell and Bozorgnia, 2014] ground motion model and were derived from basins in California subjected to crustal earthquakes.

More recently, Marafi et al. [2017] have shown that deep basins in subduction regions have different basin amplification factors than those derived from basin regions with crustal earthquakes. Frankel et al. [2018] used physics-based ground motion simulations to predict amplification factors in the basins surrounding the Puget Sound region during a magnitude-9 subduction earthquake from the Cascadia Subduction zone. These amplification factors (computed in [Marafi et al., 2019]) are also considered here and are shown in Fig. 5.1 (dashed dot-line). This paper designs base isolators which consider each of the four design spectra, separately (shown in Fig. 5.1). The performance of base isolators considering each of the four design spectra variations are later compared.

5.2.2 Numerical Analysis

Ground Motion Selection and Scaling

The performance of the base isolation systems at multiple periods was assessed using motions that were scaled and selected to match the four design spectra variations and later compared to ground-motions from the suite of M9 CSZ scenarios in Seattle. The seismic hazard in the Pacific Northwest is controlled from both crustal and subduction zone earthquakes sources. Therefore, for each design spectra, 60 ground motions were selected from recorded crustal earthquakes in the NGA-West-2 database [PEER, 2010], and another 60 ground motions were selected from recorded subduction zone earthquakes from the KiK-Net/K-Net database

[K-NET and KIK-net, 1996].

For crustal earthquake motions matched to the each design spectrum, 60 ground motions were selected and scaled from the NGA-West-2 strong motion database that were the most spectrally equivalent to the design spectra. In addition, ground motions were selected to have: (1) a unscaled peak ground acceleration of at least 0.05 g, (2) a source-to-site (Joyner-Boore) distance between 5 to 100 km, (3) a significant duration ($D_{s,5-95}$) between 1 to 60 seconds, and (4) did not include any pulse-like characteristics.

To select the most spectrally-equivalent ground motions, each ground motion in the database was scaled to have a minimum 2-norm log-scale error to the design spectrum for periods between 1 to 6 seconds. This period range was chosen because it often characterizes the equivalent natural period of a base isolated system. For each design spectra, 60 ground motions with the least 2-norm log-scale errors were selected with scale factors restricted to be between 0.2 and 5.

A similar ground-motion scaling approach was used for subduction zone earthquakes. However, these records were only selected (1) from either the 2001 M_w 8.3 Tokachi-Oki earthquake, 2011 M_w 9.0 Tohoku earthquake, and 2011 M_w 7.9 Tohoku aftershock earthquakes, and (2) had an unscaled peak ground acceleration of at least 0.05 g. Fig. 5.2 shows the median of the scaled selected ground motion acceleration spectra for crustal and subduction zone ground motions scaled and selected to the four chosen design spectra.

Base Isolation Design

The design of the SDOF structures representing the studied friction pendulum systems follows the DDBD procedure. The procedure of applying DDBD on friction type base isolation systems can be found in [Calvi et al., 2016a]. In [Calvi et al., 2016a], the isolation system and the base shear demand for the superstructure were designed given a designed displacement value and an α value (which equals to the ratio between the maximum designed based shear and the force required to activate the slider). This design procedure was modified in this study such that the isolation system and the base shear demand value were designed given

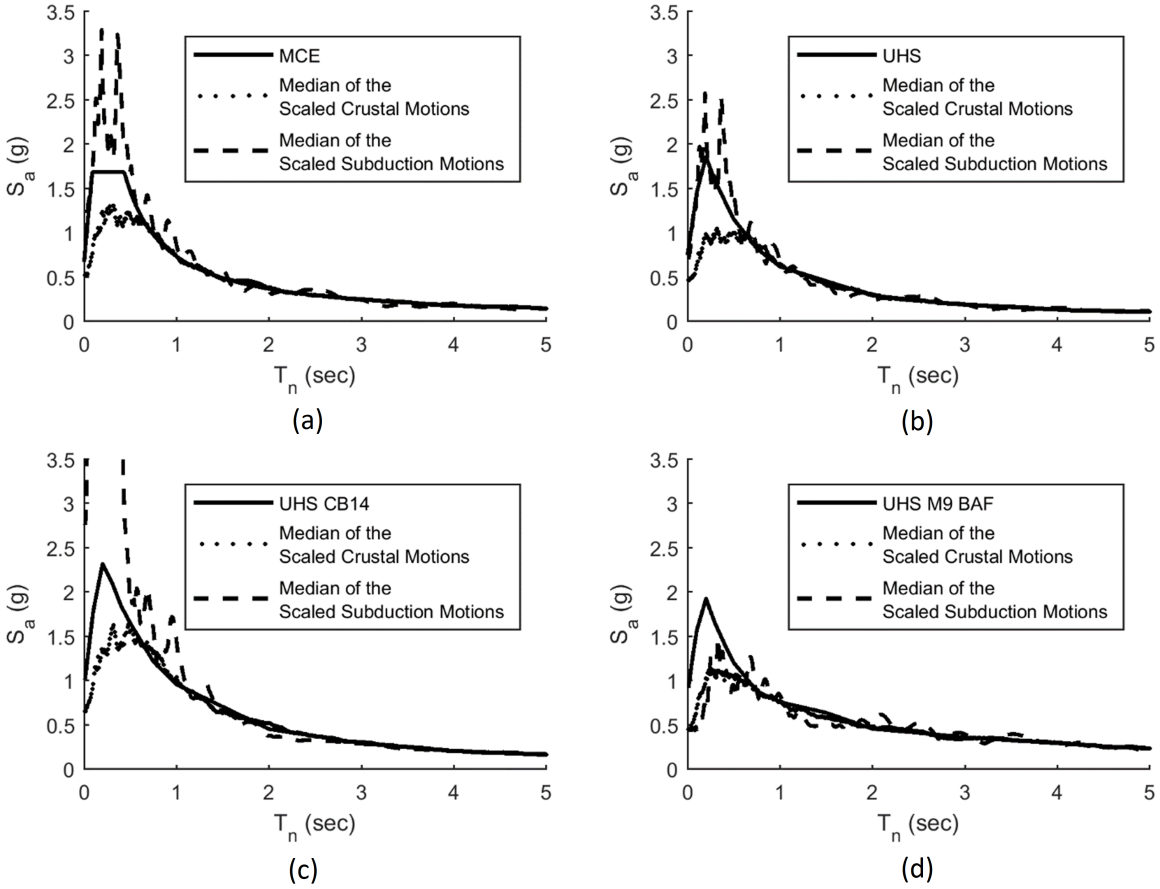

Figure 5.2: Acceleration spectra comparison between (a) MCE; (b) UHS; (c) UHS CB14; (d) UHS M9 BAF and the corresponding scaled ground motions from NGA-WEST2 (crustal) and the subduction zone ground motion database.

a target effective period, T_{eff}, and an α value, which is summarized as follows.

Given an α value, the equivalent damping ratio, ζ, is calculated using Equation (5.1), where the derivation can be found in [Calvi et al., 2016a]. Then a displacement reduction factor, η, calculated using Equation (5.2) [Priestley et al., 2007], is applied to the design displacement spectrum. The displacement demand, Δ_d, of the isolator is obtained from the reduced displacement spectrum with the corresponding designed effective period value.

$$\zeta = \sqrt{\frac{2}{\pi\alpha}} \tag{5.1}$$

$$\eta = \sqrt{\frac{7}{2+\zeta}} \tag{5.2}$$

With the effective period, the effective stiffness, K_{eff}, of the isolation system is calculated using Equation (5.3), where m represents the total mass of the superstructure. Then the base shear demand for the superstructure, V_{max}, is simply obtained using Equation (5.4).

$$K_{eff} = \frac{4\pi^2 m}{T_{eff}^2} \tag{5.3}$$

$$V_{max} = K_{eff} * \Delta_d \tag{5.4}$$

Once the shear demand is calculated, the bearing properties, including the effective radius of curvature, R_{eff}, and the coefficient of friction between the slider and the concave sliding surface, μ, can be determined using Equation (5.5) and Equation (5.6), respectively.

$$\mu = \frac{V_{max}}{\alpha m g} \tag{5.5}$$

$$R_{eff} = \frac{mg\Delta_d}{V_{max} - V_{max}/\alpha} \tag{5.6}$$

The α value used in this design procedure is chosen by the design engineer. For a fixed design effective period, as the α value increases, the effective damping decreases, resulting in a greater displacement reduction factor. Effectively, increasing in α value will increase the displacement demand. Based on Equation (5.4) to Equation (5.6), an increased α value would also decrease both the effective radius of curvature and coefficient of friction.

To achieve practical values for both the effective radius of curvature and coefficient of friction, α values usually range from 2.5 to 4.5. To keep the consistency in this study, an α value of 3 was used throughout the design. The final properties for the FPSs and DCFP systems designed for this study are summarized in Table. 5.1. For each design spectrum,

Table 5.1: Design properties of the FPSs

T_{eff} (sec)	MCE R (m)	MCE μ %	MCE Δ_d (m)	UHS R (m)	UHS μ %	UHS Δ_d (m)	UHS CB14 R (m)	UHS CB14 μ %	UHS CB14 Δ_d (m)	UHS M9 BAF R (m)	UHS M9 BAF μ %	UHS M9 BAF Δ_d (m)
1.5	0.84	9.0	0.15	0.84	8.3	0.14	0.84	12.9	0.22	0.84	11.7	0.20
2.0	1.49	6.7	0.20	1.49	5.3	0.16	1.49	8.3	0.25	1.49	8.4	0.25
2.5	2.33	5.4	0.25	2.33	4.4	0.20	2.33	6.8	0.32	2.33	7.5	0.35
3.0	3.35	4.5	0.30	3.35	3.4	0.23	3.35	5.4	0.36	3.35	6.6	0.45
3.5	4.57	3.8	0.35	4.57	2.9	0.27	4.57	4.6	0.42	4.57	6.0	0.55
4.0	5.96	3.4	0.40	5.96	2.4	0.29	5.96	3.7	0.45	5.96	5.4	0.64
4.5	7.55	3.0	0.45	7.55	2.2	0.33	7.55	3.4	0.51	7.55	4.8	0.72
5.0	9.32	2.7	0.50	9.32	2.0	0.35	9.32	3.0	0.56	9.32	4.2	0.78

base isolators with effective fundamental periods ranging from 1.5 seconds to 5.0 seconds (with an increment of 0.5 seconds) were designed. It is worth mentioning that common DCFP systems have symmetric geometric and frictional properties. Such systems, when having half the effective radius of curvature with the same frictional properties compared to FPSs, it yields almost identical hysteretic behavior as the corresponding FPSs [Fenz and Constantinou, 2006]. Thus only the design properties for the FPSs are listed.

Analysis Procedure

Four groups of NLTHA were performed, each one corresponding to one design spectrum mentioned in Section 5.2.1.

The bearings designed for each spectrum are summarized in Table. 5.1, and their hysteretic behavior were represented using SDOF systems. Nonlinear time history analyses were performed in OpenSees [Schellenberg, 2014], in which the friction pendulums were modeled using the Single Friction Pendulum Bearing Element [Mosqueda et al., 2004].

For each SDOF structure, the following three sets of ground motions were considered for the NLTHA, and the maximum absolute displacements from the analyses were recorded.

- 60 scaled ground motions selected and scaled from NGA-West-2 database.
- 60 scaled ground motions selected and scaled from the subduction zone ground motion database.
- 30 pairs of the simulated M9 motions.

It should be noted that all of the analyses are performed such that the structure was under uni-directional shaking, however, the simulated M9 motions are given in orthogonal pairs. To compare the maximum displacement among each group in a fair manner, the geometric mean of the resulting responses from the paired M9 motions were compared with the maximum displacements from the two other groups.

5.3 Numerical Analysis Results

For each design spectrum, the design displacement versus the effective period were plotted. These values directly come from the reduced displacement spectrum as mentioned in the DDBD procedure. Then the median maximum displacements for each effective period from each NLTHA group were plotted. As mentioned in the introduction section, the return period of the M9 earthquake is approximately 500 years; the 84^{th} percentile of the maximum displacements from the M9 motions would be corresponding to a return period that is approximately 2500 years, which is the return period of the MCE hazard level. To indicate the extreme case from M9 motions, the 100_{th} percentile of the maximum displacements for each effective period was also plotted.

First, as shown in Fig. 5.3, the median maximum displacement responses from both spectrum-matching motions selected from crustal motions and subduction zone motions match well with the design displacement demands. This indicates that the DDBD procedure and the ground motion selection and scaling procedure adopted in this study provided good preliminary approximation on the maximum displacement compared to the NLTHA results.

Secondly, the median response (i.e. 50^{th} percentile M9 as shown in Fig. 5.3) from the simulated M9 motions falls below the design displacement demands by an average value of

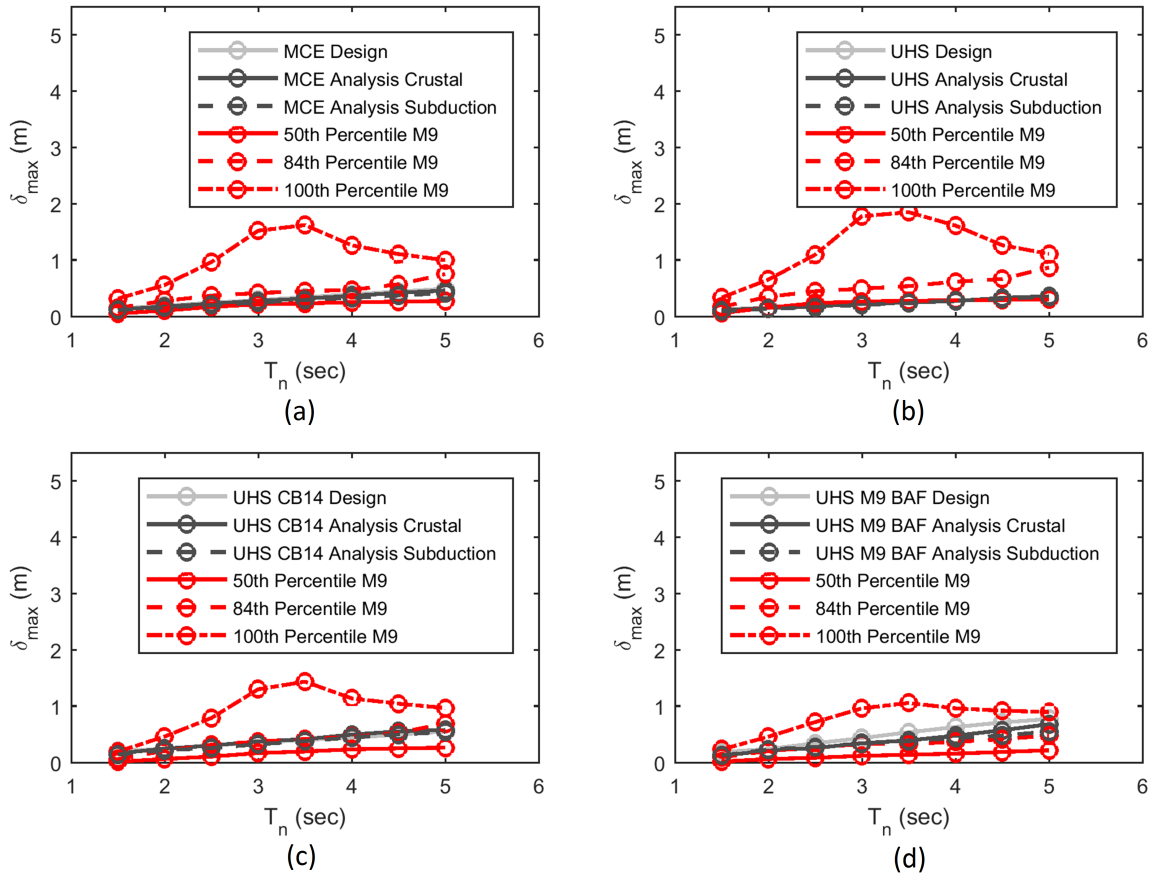

Figure 5.3: Design period versus maximum displacement for (a) MCE; (b) UHS; (c) UHS CB14; (d) UHS M9 BAF.

approximately 10% for the considered period range (for all four considered design spectra). However, when comparing the response with compatible return periods (i.e. 84_{th} percentile maximum displacement from simulated M9) with the design displacement demands based on MCE or UHS without basin amplification factors, the 84th percentile maximum displacement responses from the simulated M9 motions have displacement demands increase of 1%, 8.6%, 12.6%, 12.6%, 10.5%, 8%, 12.9%, 26%, and 4%, 20%, 25.2%, 27.5%, 28.2%, 33.7%, 34.7%, 52.3%, respectively, for periods ranging from 1.5 to 5.0 seconds with an increment of 0.5 seconds.

In contrast, when designed based on UHS with CB14 amplification factors, the 84_{th} percentile curve from M9 is approximately on top of the design displacement curve. When designed with UHS with M9 BAF, the 84_{th} percentile curve from M9 falls below the design displacement curve and have an average decrease of demands of 17.2%.

To analyze the results for each period in more detail, the probability of the maximum displacement exceeding certain displacement values for each period were plotted from Fig. 5.4 to Fig. 5.7. It is shown that when the isolation systems are designed based on UHS with either CB14 or M9 amplification factors, the probability of the maximum displacement from the M9 motions exceeding certain displacement values are almost always lower than the probability of the maximum displacement from the design spectra-matching motions exceeding the same displacement values. However, when designed based on MCE or UHS without basin amplification factors, the probability of the maximum displacement from the M9 motions exceeding certain displacement values are sometimes higher than those obtained from the design spectra-matching motions, indicating the displacement demand obtained from the design spectra would not be able to perform well during the simulated M9 earthquake.

Finally, as shown in Fig. 5.3, while the relationships between the displacement demand and the fundamental period for the design spectra are approximately linear, the 100_{th} percentile maximum displacement from the simulated M9 motions indicates a particularly large displacement demand for effective periods between 2.5 to 4.0 seconds. This results match with what was found by Marafi et al. [2019].

5.4 Chapter Conclusions

This chapter presents the investigation of the performance of base isolated structures, in particular, FPSs and DCFP systems with symmetric geometric and frictional properties, under the effect of Cascadia Subduction Zone M9 earthquakes. A large set of SDOF structures were designed based on MCE_R level design spectra and evaluated with the simulated physics-based simulated M9 motions. The considered design spectra includes risk-targeted MCE_R design spectrum from NEHRP 2015, UHS without any basin amplification factors,

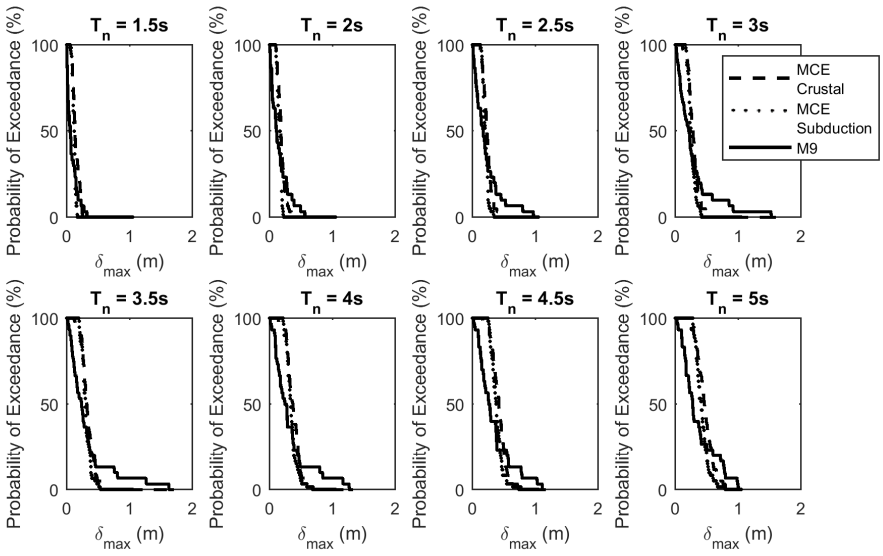

Figure 5.4: Probability of exceedance of the maximum displacement value for each design period using MCE spectrum.

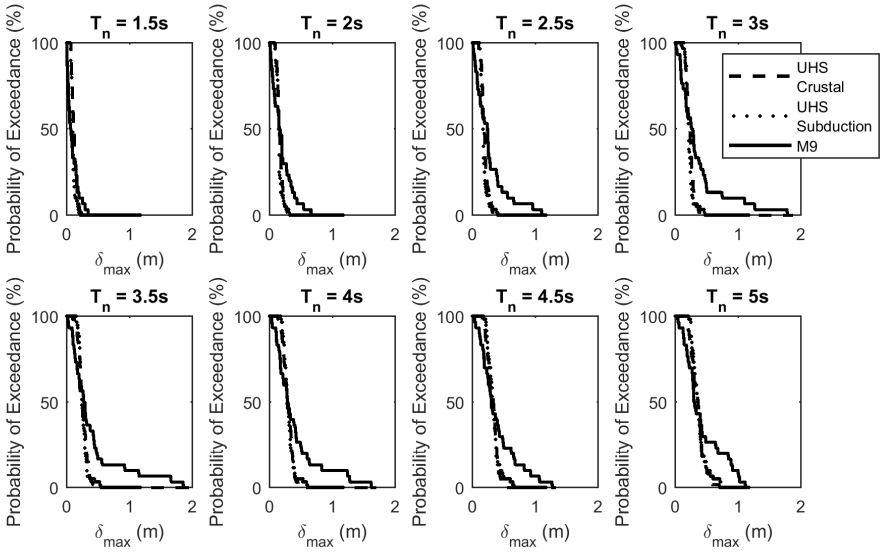

Figure 5.5: Probability of exceedance of the maximum displacement value for each design period using UHS without any basin amplification factors.

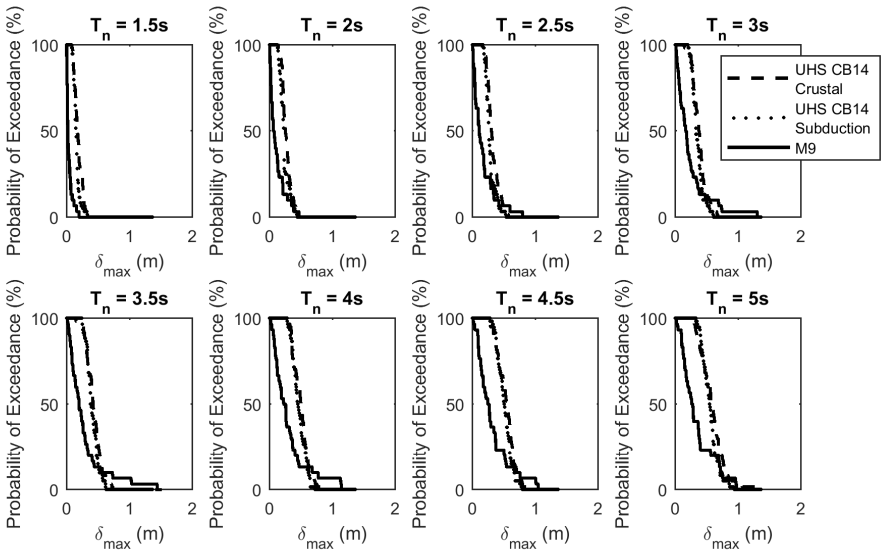

Figure 5.6: Probability of exceedance of the maximum displacement value for each design period using UHS CB14.

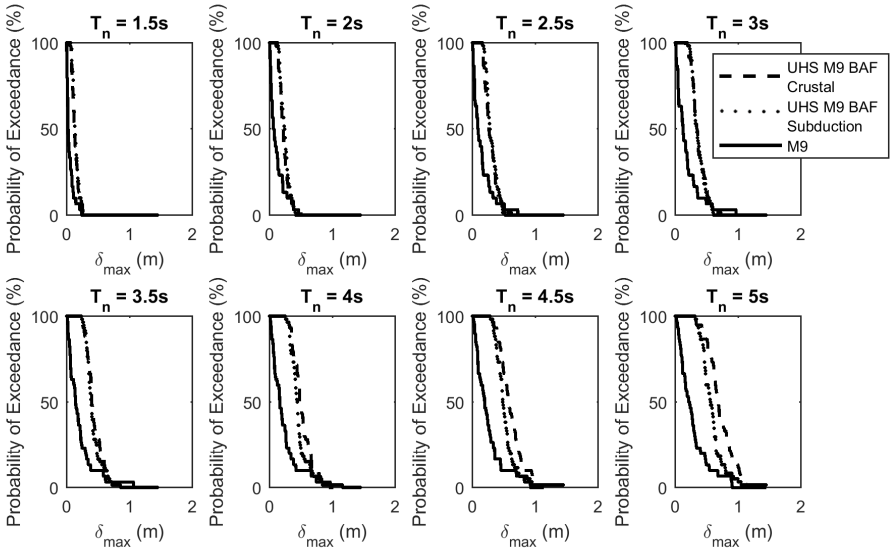

Figure 5.7: Probability of exceedance of the maximum displacement value for each design period using UHS M9 BAF.

UHS with CB14 amplification factors, and UHS with M9 basin amplification factors. It was found that, when comparing the 84^{th} percentile maximum displacement values (which has approximately the same return period as the MCE level earthquakes) with the design displacement demands, the first two groups (without basin amplification factors) exceed the demands, and the last two groups (with basin amplification factors) did not. Within the 30 pairs of the simulated M9 motions, a small subset of the motions were found to be particularly damaging. The reasons requires further investigation.

Chapter 6

ACCOUNTING FOR SPECTRAL SHAPE IN A SIMPLIFIED METHOD OF ANALYZING FRICTION PENDULUM SYSTEMS

Note: This chapter is a reproduction of Yang et al. [2020]

The previous chapter focused on the performance of Friction Pendulum Systems during the simulated M9 motions when designed using the current code design spectrum or design spectra amplified with basin amplification factors based on previous studies. However, it did not address how the simulated M9 motion affect the current analysis method of such systems. This chapter aims to shed light on the accuracy of using simplified method to analyze Friction Pendulum Systems considering the simulated M9 motions. It also presents a newly proposed displacement-spectrum shape correction factor that improves the accuracy of the simplified method, by taking account the "irregularity" of the seismic input (expressed in the form of an elastic displacement spectrum).

6.1 Chapter Introduction

Simplified methods of analyzing an equivalent single-degree-of-freedom system are often adopted in modern building codes for analyzing Friction Pendulum Systems (FPSs) for seismic isolation (e.g. ASCE [ASCE, 2017] and Eurocode 8 [EC8, 2004]). These simplified methods also provide a lower bound for the force values that should be used in place of values obtained from dynamic time-history analysis [ASCE, 2017]. Thus the accuracy of such methods is of great importance.

These simplified methods analyze base-isolated systems with single degree of freedom systems with equivalent linear elastic and viscous damping properties. These methods can

be applied to the design of not only FPSs, but also other inelastic structural systems with well-characterized hysteretic behavior. The accuracy of such methods has been studied by numerous researchers [Kircher and Lashkari, 1989; Winters and Constantinou, 1993; Tsopelas et al., 1997; Miranda and Ruiz-Garcia, 2002; Guyader and Iwan, 2006].These studies have shown that the simplified methods are able to reasonably predict the mean maximum displacement from nonlinear time history analyses for a suite of ground motions, however, there is often large standard deviations [Tsopelas et al., 1997]. Moreover, these studies have largely considered strong ground motion recordings from crustal earthquakes recorded on stiff-soil site or medium-soil site conditions. To further explore the accuracy and limitations of simplified methods, work in Pavlou and Constantinou [2004] considered near-field and soft-soil ground motions. Nonetheless, the accuracy of these methods has never been assessed considering ground motions generated from subduction zones or amplified by basin effects, which modify the characteristics of response spectra [Graves et al., 1998; Frankel et al., 2009; Marafi et al., 2017].

The simplified method evaluated herein is the effective stiffness and damping method that is described in design code provisions for base-isolated structures (e.g. ASCE [ASCE, 2017] and Eurocode 8 [EC8, 2004]). To shed light on the accuracy of using this method for FPSs with subduction zone motions or motions amplified due to basin effects, this paper presents:

- Information on four sets of ground motions considered in this study, which include both crustal and subduction zone ground motions, with and without basin effects.

- A comparison between the average values of displacement reduction factors, as defined in Section 6.2, obtained through analyses with considered ground motion datasets and the values calculated based on empirical equations provided by different code provisions.

- Results of maximum absolute displacement from nonlinear time history analysis in

comparison to design displacement computed from the simplified method.

- A newly proposed displacement-spectrum shape correction factor that improves the accuracy of the simplified method for FPSs, by taking into account the "irregularity" of the seismic input (expressed in the form of an elastic displacement spectrum). This correction factor depends on the effective period and effective damping ratio of the isolation system at design displacement.

6.2 Overview of Current Design Procedures

With minor differences between them, the simplified methods adopted in modern design code provisions (e.g. ASCE [2017]; EC8 [2004]) for base-isolated structures are based on displacement-based design principles. The simplified method involves the following steps: (a) select the design displacement of the structure, (b) construct the hysteretic loop of the isolator at the design displacement level, (c) estimate the equivalent SDOF system's effective stiffness and effective damping ratio, (d) calculate a displacement reduction factor based on effective damping ratio, (e) obtain the seismic input in the form of displacement response spectrum at 5% damping ratio, (f) apply displacement reduction factor to the 5% damped displacement response spectrum to obtain reduced displacement spectrum corresponding to the effective damping ratio of the isolation system, (g) estimate the effective period of vibration of the system, (h) obtain displacement demand from the reduced displacement spectrum given the effective period of vibration, and (i) repeat steps (b) to (h) until the difference between design displacement and displacement demand is sufficiently close. With a converged design displacement value, the base shear demand can be calculated from the hysteretic loop of the isolation system and is then distributed over the height of the superstructure.

The main difference between the different code provisions is in the way the displacement reduction factor is calculated. The displacement reduction factor (i.e., damping reduction factor) is defined as the spectral displacement ratios at different damping levels normalized to the 5% damped displacement spectrum. As a function of the equivalent damping ratio

of the isolation system at the design displacement, displacement reduction factors aim to account for the effect of hysteretic damping on the force and displacement response of the building.

Figure 6.1 shows a comparison from various building codes between the displacement reduction factors, η, versus the damping ratio, ζ, for ASCE 7-16 [ASCE, 2017], and Eurocode 8 (1994) [EC8, 1994] and (2004) [EC8, 2004]. It should be noted that ASCE 7-16 provides a table of damping reduction factors given several damping ratios (other values are linearly extrapolated), while Eurocode 8 (1994) and (2004) use equations of $\sqrt{7/(2+\zeta)}$ and $\sqrt{10/(5+\zeta)}$, respectively. These three cases were chosen here because the Eurocode 8 (1994) equation is recommended for Direct Displacement Based Design method [Priestley et al., 2007], the other two are the current design provisions in the United States and Europe, respectively. A more thorough review can be found in Lin and Chang [2003]. Compared to the other codes the Eurocode 8-1994 provides the most unconservative results (i.e. greater reduction factor given a damping ratio), and the ASCE 7-16 provides the most conservative one.

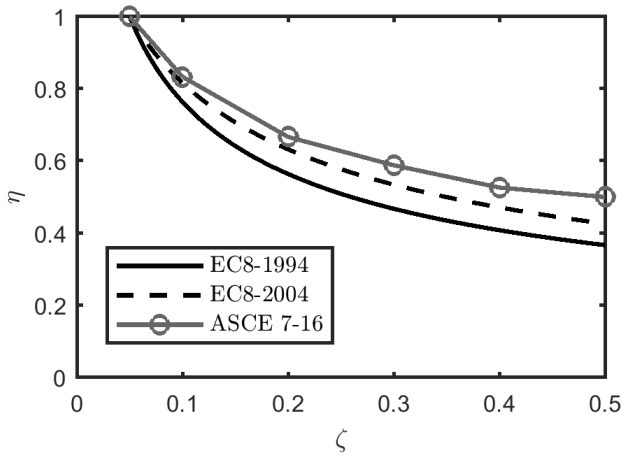

Figure 6.1: A Comparison of the displacement reduction factor with respect to damping ratio for Eurocode 8 (1994)[EC8, 1994], Eurocode 8 (2004)[EC8, 2004], and ASCE 7-16 [ASCE, 2017].

While these equations provide different levels of displacement reduction for a given damping ratio, they are all period independent. Numerous researchers have studied the accuracy of these equations [Lin and Chang, 2003; Bommer and Mendis, 2005; Lin and Chang, 2004]. Lin and Chang [2003] focused on the application of damping reduction factors on the acceleration spectrum, velocity spectrum, and displacement spectrum, while Bommer and Mendis [2005] and Lin and Chang [2004] investigated the accuracy of these equations for varying site classes, earthquake magnitude, site-to-source distances, and duration. Near source directivity effects were also considered by Bommer and Mendis [2005], however, subduction zone earthquakes or basin amplified ground motions were not included in any of these previous studies.

6.3 Evaluation of Current Simplified Method under Ground Motions with Different Characteristics

6.3.1 Description of the ground motion datasets used

To evaluate the accuracy of the simplified method on FPSs with subduction zone motions and basin amplified motions, four sets of ground motions were considered:

- 60 ground motions were selected from the NGA-WEST2 database [PEER, 2010] and scaled to match the MCE_R design spectrum for Seattle (Site Class C) based on NEHRP 2015 [NEHRP, 2015]. First, all ground motions from NGA-WEST2 were screened based on the following criteria: (1) an unscaled peak ground acceleration of at least 0.05 g, (2) a source-to-site (Joyner-Boore) distance between 5 to 100 km, (3) no pulse-like characteristics. To select the ground motions providing the best spectral match, each ground motion in the database was scaled to have a minimum square-root-the-sum-of-squares of the log error compared to the design spectrum for a period range of 1 to 6 seconds. This period range was chosen because it was deemed appropriate for typical equivalent periods of FPS-isolated structures. Finally, 60 ground motions with the least square-root-the-sum-of-squares of the log errors were selected with scale factors

limited between 0.2 and 5. This set of ground motions is a benchmark for the study given that it represents strong crustal earthquakes as studied by previous researchers [Kircher and Lashkari, 1989; Winters and Constantinou, 1993; Tsopelas et al., 1997; Miranda and Ruiz-Garcia, 2002; Guyader and Iwan, 2006]. A comparison between the design spectrum and the average scaled spectrum is shown in Figure 6.2(a). The median 5-95% significant duration was approximately 26 seconds with a coefficient of variation of 130%. This set of motions is denoted as "Crustal" in the following discussion.

- The second set of motion is the simulated M9 Cascadia Subduction Zone motions described in Chapter 5. This set of motions is denoted as "M9" in the following discussion.

- The last two sets of motions were developed by Chandramohan et al. [2016a]. Each of these two sets have 73 ground-motion pairs (X and Y component) and were aimed at evaluating the influence of ground motion duration on structural collapse capacity. One set of ground motions was chosen from subduction zone earthquakes and the other from crustal earthquakes. Each individual record in the Crustal motion dataset was chosen to have a spectrally equivalent record in the subduction zone motion dataset, thus the primary difference between the two sets is the significant duration of the motion. These two sets of motions are denoted as "SE - Long" and "SE - Short" respectively in the following discussion.

6.3.2 Numerical analysis procedure

To evaluate the accuracy of using the simplified method to analyze FPSs when subjected to ground motions with different characteristics, single-degree-of-freedom systems that characterize the hysteretic behavior of FPSs were designed and analyzed. A design was completed for each ground motion individually using the simplified method described above and for a

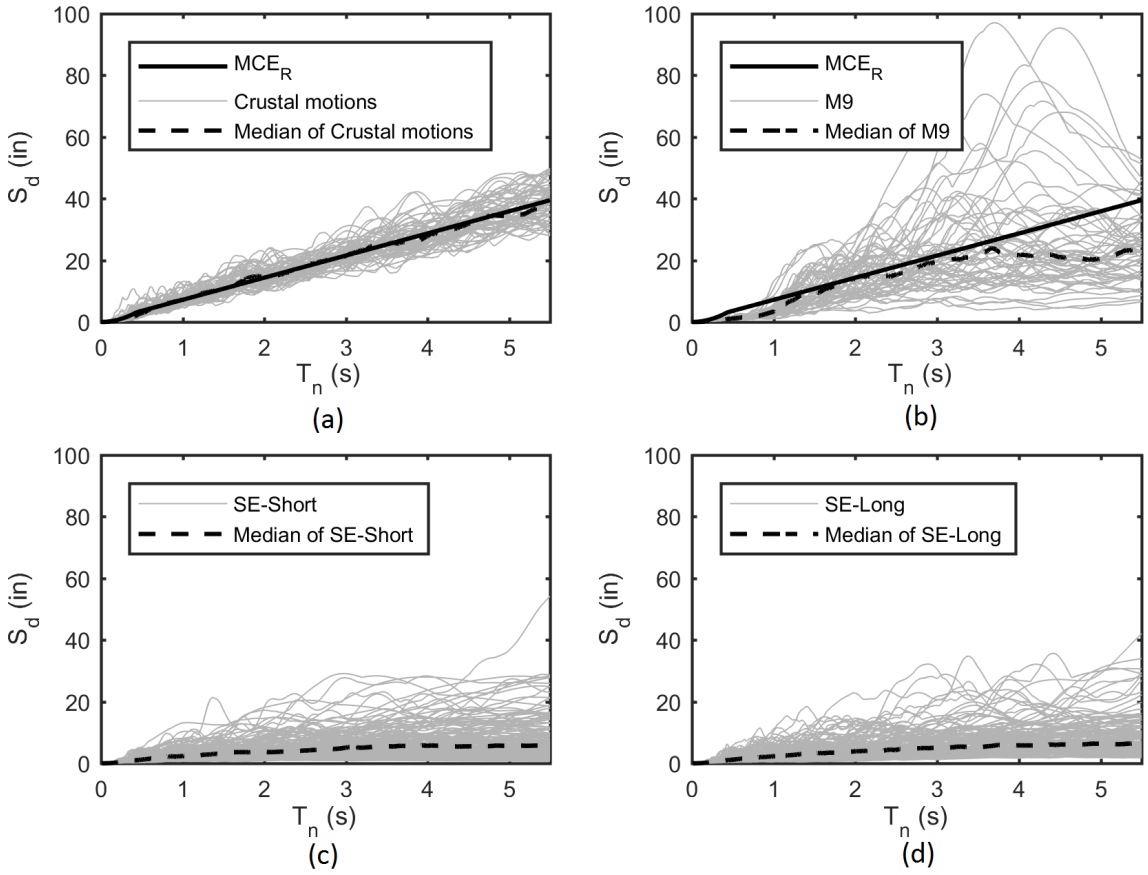

Figure 6.2: Spectral displacement with respect to period for (a) NGA-West-2 motions scaled to the MCE$_R$ design spectrum from NEHRP, (b) simulated magnitude-9 CSZ earthquake in Seattle, (c) and (d) spectrally equivalent motions with short and long significant durations, respectively, developed by Chandramohan et al. [2016a].

range of FPS properties (period and damping) as described below. Then, nonlinear response history analysis was performed in OpenSees [McKenna, 1997] for each designed FPS and ground motion, in which the FPS was modeled using the Single Friction Pendulum Bearing Element [Mosqueda et al., 2004]. The resulting maximum displacements were recorded to compare with the displacement predicted using the simplified method.

The equivalent lateral force procedure, ASCE 7-16 [ASCE, 2017] requires that "the effective period of the isolated structure is greater than three times the elastic, fixed-base period

of the structure above the isolation system" and "the effective period of the isolated structure at the maximum displacement is less than or equal to 5.0 s". Thus for each ground motion considered, FPSs with equivalent natural periods from 1.5 to 5.0 s (with an increment of 0.5 s) were considered in this study.

For the design of FPSs, the method described in [Calvi et al., 2016b] was followed. This method follows the direct displacement-based design method proposed by Priestley et al. [2007]. The only difference between this method and the one described in Section 6.2 is that the procedure becomes non-iterative by introducing a parameter α (which is equal to the ratio between the designed base shear and force required to activate the slider). By selecting an α value, the effective damping ratio can be calculated using Equation (6.1):

$$\zeta = 2/\alpha\pi \tag{6.1}$$

The displacement reduction factor can then be calculated using the equations or tables that generated the curves in Figure 6.1, depending on the code provisions used. In this study, all three cases presented in Figure 6.1 were considered. Finally, the design displacement can be obtained either from a predetermined effective period (or vice-versa) using reduced displacement spectrum.

An α range of 2 to 4 (with an increment of 0.5) was chosen for this study to represent FPSs with different effective damping ratios. These are realistic α values based on Calvi and Calvi [2018]. In addition, this range of α is equivalent to an effective damping ratio range from 16% to 32%. The upper bound of the damping ratio was set to be approximately equal to 30%, which was selected because it is the limit for using the equivalent lateral force procedure in ASCE 7-16 [ASCE, 2017].

6.3.3 Numerical results

For brevity, only detailed results associated with using the displacement reduction equation provided by Eurocode 8 (1994) [EC8, 1994] are presented in this section. While only the final

outcome is reported for the other two cases, detailed results can be found in Appendix C.

Figure 6.3 shows the boxplots of the analysis-to-design ratios for all analyses with respect to the equivalent natural period of the isolation systems (T_n) for the four ground-motion sets previously described. For each T_n the extent of the box represents the 25^{th} and 75^{th} percentile, the horizontal line within the box represents the 50^{th} percentile, and the extent of the whiskers corresponds to the minimum and maximum observed values. For brevity, only the results pertaining to α equals to 3 are presented here. Similar trends were observed for all the other α values considered. Appendix C presents the results for other α values.

Figure 6.3(a) shows that the analysis-to-design ratios considering the Crustal ground motion set have median values that are approximately equal to 1.0 (ranging from 0.82 to 1.04) at all period values. However, within each period there is variability in analysis-to-design ratios. This variability can be quantified using the coefficient of variation of the analysis-to-design ratios (plotted in Figure 6.5(a)) which ranges from 0.09 to 0.23 for the Crustal ground-motion set. This large variability indicates that even when the median ratio is approximately 1.0, the general prediction is not sufficiently accurate. Thus, the simplified method works well in an average sense, however, when considering all individual analyses, the accuracy of the method could be improved.

Figure 6.3(b) shows that the analysis-to-design ratios using the M9 ground-motion set have median values mostly smaller than 1.0 (ranging from 0.51 to 1.16). An analysis-to-design ratio less than 1.0 means that the design is conservative. It is worth mentioning that the applied simplified method incorporated the most unconservative damping reduction equation, when other existing equations were used (e.g., Eurocode 8 (2004) or ASCE 7-16), the final results were more conservative. However, these differences would not account for the apparent period dependency in the analysis-to-design ratio (Figure 6.3(b)). For example, 1.5-second oscillators had a median analysis-to-design ratio of 0.51 whereas this ratio was around 1.16 for oscillator periods around 5.0 seconds. This period dependence is likely due to ground-motion characteristics [Marafi et al., 2019] not currently accounted for in the displacement reduction factor estimate. The coefficient of variation of the analysis-to-design

ratios (plotted in Figure 6.5(b)) ranges from 0.14 to 0.31, which is greater than those from the Crustal set.

For the SE - Short and SE - Long datasets, similar results were observed in terms of accuracy. Figure 6.4 shows the analysis-to-design ratio with respect to (5%-95%) significant duration. The least squares linear regression line is also shown in the plot. An R squared value of 0.01 means that significant duration does not affect the accuracy of the simplified method. In general, for this study, the median analysis-to-design ratios are slightly above 1.0, ranging from 1.1 to 1.4 for SE-Short and 1.0 to 1.2 for SE-Long. This was be due to the design decision of adopting the least conservative displacement reduction factor (i.e., Eurocode 8-1994 [EC8, 1994]).

6.4 A Proposed Solution: the Displacement-Spectrum Shape Correction Factor

The results discussed thus far show that the accuracy of the simplified method is greatly compromised in presence of simulated M9 CSZ motions. For the crustal and subduction zone earthquakes without basin effects, even though the median analysis-to-design ratios show a good match, the overall performance evaluated in terms of COV indicates that the accuracy of the design is also not ideal. However, it should be noted that the variability is partially due to the non-smoothness of the individual displacement spectrum. To improve the accuracy of the simplified method, a displacement-spectrum shape correction factor, SCF, is proposed in this section.

The development of SCF was motivated by several factors as discussed here.

First, according to the equivalent lateral force procedure outlined in ASCE 7-16 [ASCE, 2017], the maximum displacement of the isolation system (i.e. design displacement) should be calculated using:

$$D_M = \frac{gS_{M1}}{4\pi^2 B_M} T_M \tag{6.2}$$

where g is the acceleration of gravity, S_{M1} represents the MCE$_R$ 5% damped spectral

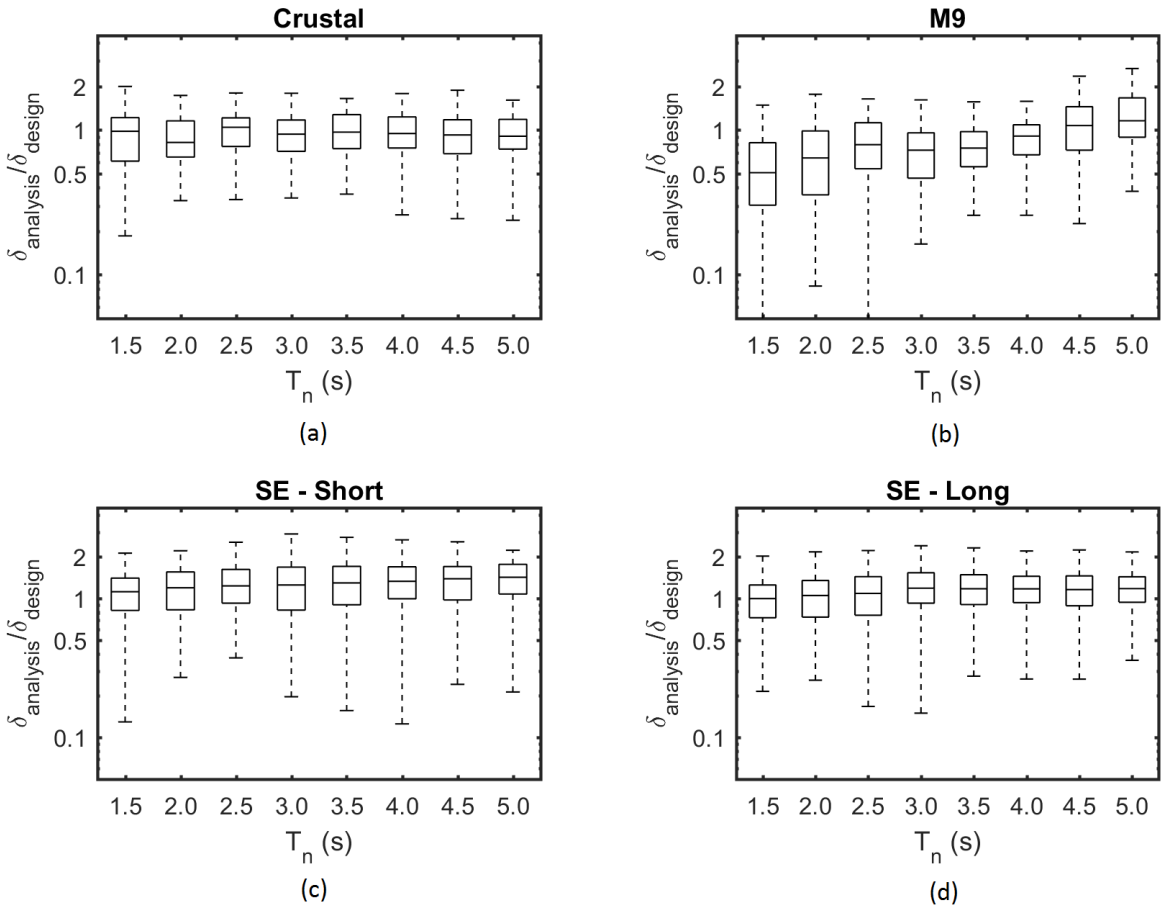

Figure 6.3: Numerical results (for α equals to 3) of the ratio (in log-scale) between maximum absolute displacement from NLTHA and design displacement varying by design period for each ground motion dataset.

acceleration parameter at 1-s period in units of g-sec, T_M represents the effective natural period and B_M is the numerical coefficients for the effective damping ratio of the isolation system at design displacement (i.e., inverse of the displacement reduction factor). This equation implies that the long-period branch of the displacement response spectrum is linear in period. Figure 6.2(a) shows that the displacement spectra for Crustal motions are approximately linear with respect to period, whereas the displacement spectra for the simulated M9 motions are highly nonlinear with respect to period.

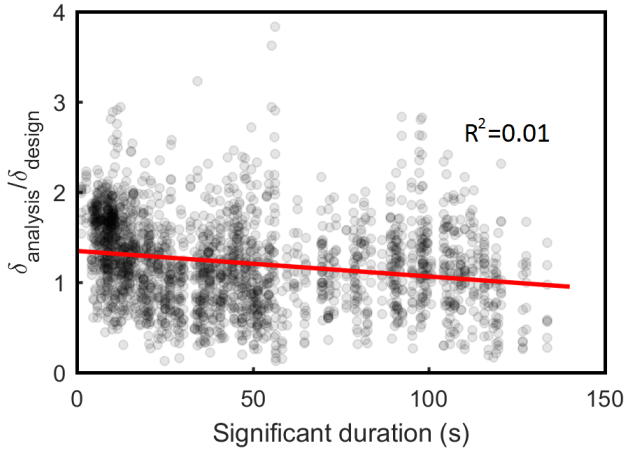

Figure 6.4: Design-to-analysis ratio with respect to (5%-95%) significant duration including results from SE-Short and SE-Long ground-motion sets.

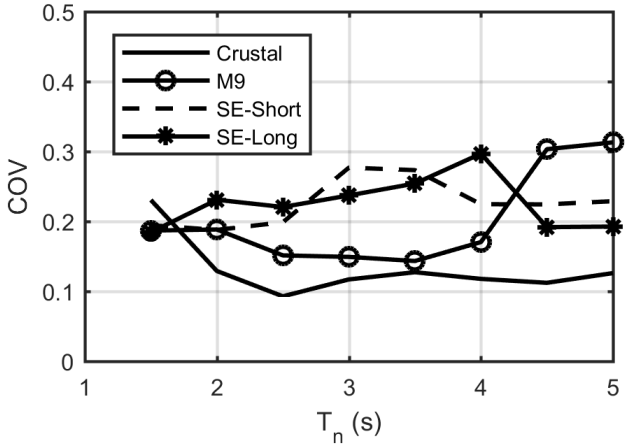

Figure 6.5: Numerical results (for α equals to 3) of the coefficient of variance (COV) of the analysis-to-design ratio versus design period for each ground motions dataset.

One of the key assumptions in the current design procedure is that the displacement reduction factor remains constant for a given damping ratio. To evaluate the accuracy of this assumption, the elastic displacement response spectrum at different damping ratios (10%, 20%, 30%, and 50%) were developed for all motions in all datasets. The obtained displacement spectra were then divided by the elastic displacement response spectrum at 5%

damping ratio to calculate the displacement reduction factor for each ground motion.

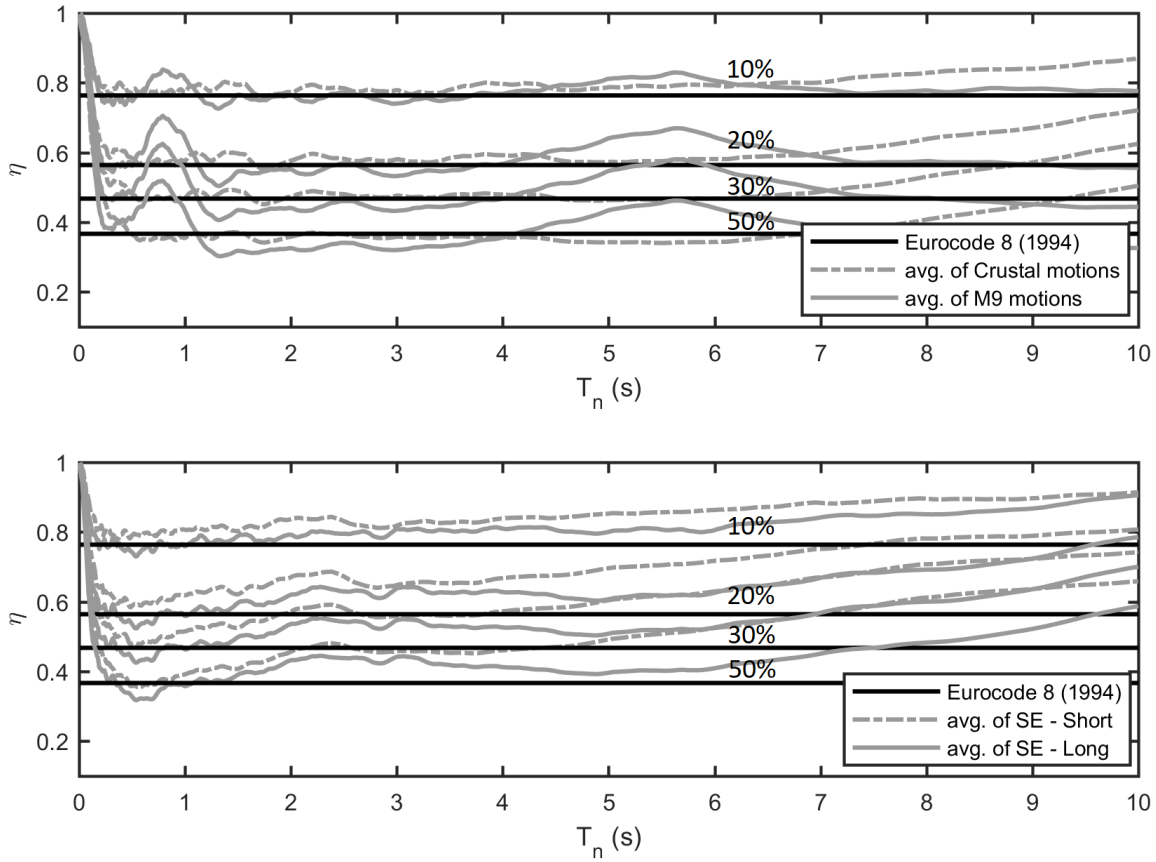

Figure 6.6: Mean displacement reduction factors for (a) Crustal and M9 ground motions dataset and (b) SE - Short and SE - Long ground motion dataset. Mean displacement reduction factors predicted by Eurocode 8 (1994) [EC8, 1994] are also shown as black solid lines.

Figure 6.6 shows the comparison between the code displacement reduction factor from Eurocode 8-1994, and the average displacement reduction factor at different damping levels for each ground motion dataset. The average displacement reduction factor for the Crustal motion dataset between 1.5 to 5.0 s periods can be well approximated by a constant. This observation is consistent with the notion that the displacement reduction factor is period independent, as used in the code equations. The SE - short and SE - Long dataset also yield

an approximately constant reduction factor, however it is more conservative than equation used in Eurocode 8 (1994). This observation is consistent with the results that, when a more conservative displacement reduction equation was used, the accuracy of the results for SE - Short and SE - Long was improved, as shown in Appendix C. For the M9 motion dataset, significant period dependency can be observed near periods of 1.0 s and 5.0 s.

Based on the above observations, a period-dependent displacement-spectrum shape factor is proposed as a measure of the level of "linearity" of the displacement spectrum.

6.4.1 Displacement-spectrum shape factor

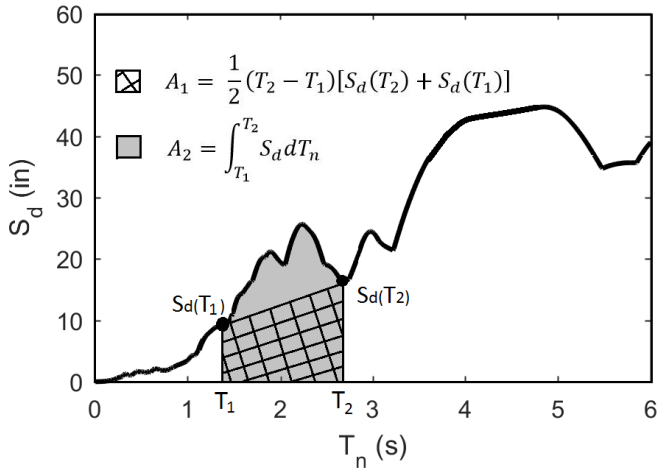

Figure 6.7: Schematic illustration of calculating SS_d.

To quantify the linearity of a displacement spectrum, a displacement-spectrum shape factor, SS_d, based on the elastic displacement spectrum at 5% damping is proposed and can be calculated as the area of region A_1 divided by the area of region A_2, which is shown in Figure 6.7. It should be noted that this shape factor is unaffected by the scaling of the ground motion as both areas increase linearly with scale factors.

6.4.2 Displacement-spectrum shape correction factor

The correlation between the analysis-to-design ratios (Figure 6.3) and their corresponding SS_d values is shown in Equation (6.3) and Figure 6.8 for α equal to 3.0, corresponding to $T_2 = T_n$, and $T_1 = 0$. A line-of-best-fit is computed using regression analysis (using ordinary least squares) and found to have an R^2 of 0.55. Similar trends were found for all values of α, where the R^2 value was found to be equal to 0.55, 0.55, 0.54, and 0.54 for α values of 2.0, 2.5, 3.5, and 4.0, respectively.

$$ln(\delta_{analysis}/\delta_{design}) = p1 \cdot SS_d + p2 \tag{6.3}$$

A critical input of the calculation of SS_d is the period range of evaluating the linearity of the displacement spectrum. To examine this, a parametric study on the period range for calculating SS_d was performed. The considered range of T_1 and T_2 were, respectively, from 0 to $0.8T_n$, and from $0.8T_n$ to $2T_n$. As shown in Figure 6.9, the R^2 from linear regression analysis suggested that when T_1 equals 0 and $T_2 = T_n$, the correlation between the analysis-to-design displacement ratio and SS_d can be best represented by a linear function. This implies that the linearity of displacement spectrum from 0 up to the equivalent natural period of the analyzed isolation system is significant to the accuracy of the simplified method.

6.4.3 Relationship between damping ratio and linear regression coefficients for spectral shape

The same analysis was performed considering all the other α values (from 2.0 to 4.0 with increments of 0.5). It was found that for different α values (i.e., damping ratios), the linear regression coefficients for the displacement-spectrum shape correction factor, SCF, are different. As shown in Figure 6.10, the coefficients p1 and p2 vary linearly with α and they can be calculated using Equation (6.4) and Equation (6.5).

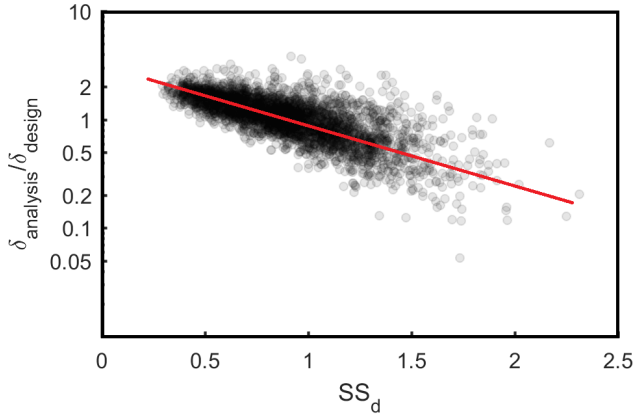

Figure 6.8: Linear regression analysis between analysis-to-design displacement ratio and SS_d for all data points (α equals to 3) in four ground motion datasets.

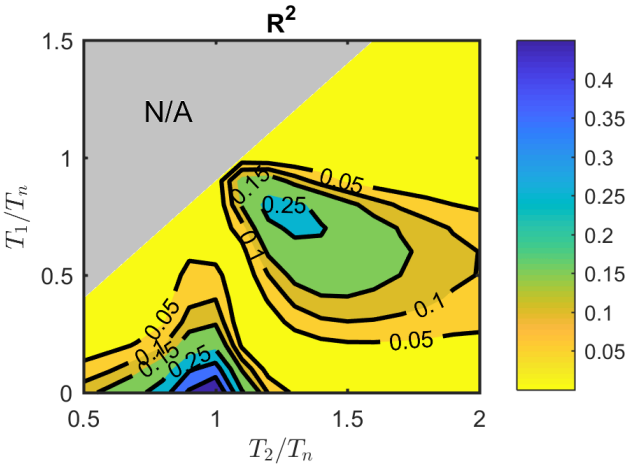

Figure 6.9: R^2 for linear regression analysis varying the period range for calculating SS_d.

$$p1 = 0.27\alpha - 2 \tag{6.4}$$

$$p2 = -0.27\alpha + 2 \tag{6.5}$$

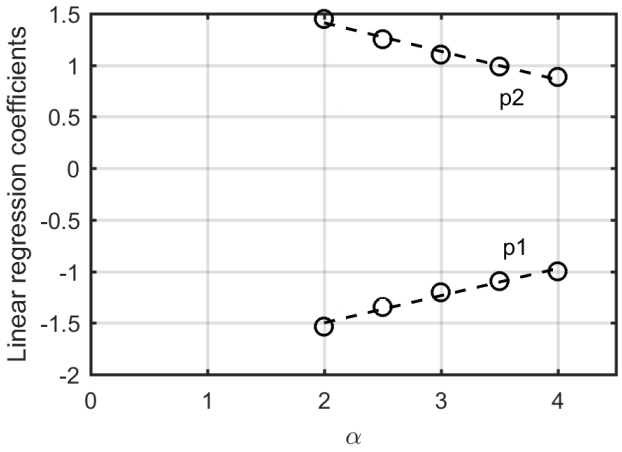

Figure 6.10: Relationship between α and the linear regression coefficients in displacement-spectrum shape correction factor.

6.4.4 Correction factor and corrected results

Using Equations 6.3 to 6.5 above, the design-to-analysis displacement demand ratio can be related to the SS_d using Equation (6.6):

$$\delta_{design}/\delta_{analysis} = e^{(0.27\alpha-2)(SS_d+1)} \tag{6.6}$$

The resulting displacement-spectrum shape correction factor, SCF, can thus be calculated using Equation (6.7):

$$\delta_{analysis} = \delta_{design} \cdot SCF = \delta_{design} \cdot e^{-(0.27\alpha-2)(SS_d+1)} \tag{6.7}$$

where SS_d is calculated as illustrated in Figure 6.7 using $T_1 = 0$ and $T_2 = T_n$. The corrected displacement demand can be obtained by multiplying the design displacement demand (δ_{design}) by SCF. Figure 6.11 shows how the design and analysis displacement demands are related without and with SCF applied for all periods and ground-motion sets. As expected, the correlation coefficient between the design and analysis displacement increased from 0.58 (Figure 6.11(a)) to 0.75 (Figure 6.11(b)) when applying SCF to the design displacement.

Table 1 shows the median and coefficient of variation values for each group motion dataset with and without SCF.

Figure 6.12 shows the comparison of analysis-to-design ratios with and without the SCF applied with respect to period for each ground-motion set. It can be observed that after applying SCF, the median ratios of all groups are approximately one (summarized in Table 1). The overall variability in the analysis-to-design ratio was significantly improved as quantified using the coefficient of variation. Figure 6.13 shows the comparison of COV of analysis-to-design ratios with and without the SCF applied with respect to period for each ground-motion set. The figure and Table 1 show that the COV reduced by approximately 20% in all ground motion sets. It is worth mentioning that the COV of the analysis-to-design ratio for M9 motion dataset increased at periods 1.5 s and 2.0 s. While the reasons remain unclear, it should be noted that FPS-isolated systems typically have equivalent natural period values above 2.0 s. Thus this increase in COV at low periods do not affect practical design of FPS-isolated systems.

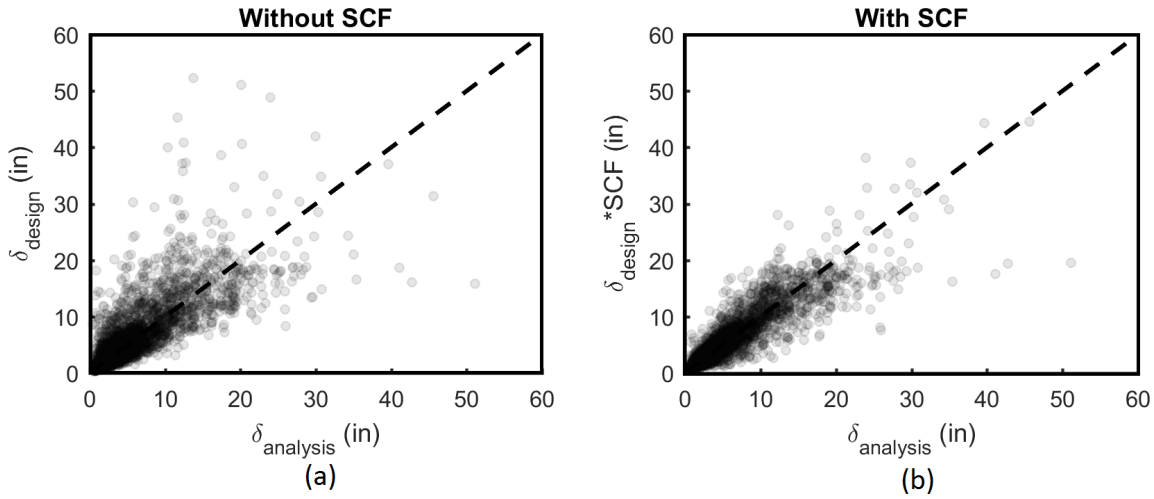

Figure 6.11: Comparison of maximum absolute displacement from analysis and design displacement for all periods and ground-motion sets (α equals to 3) (Crustal, M9, SE - Short, SE - Long) (a) without applying SCF and (b) with applying SCF.

Table 6.1: Median and coefficient of variance comparison before and after applying SCF for each ground motion dataset.

GM	Crustal		M9		SE-Short		SE-Long	
	w/o SCF	w/SCF	w/o SCF	w/SCF	w/o SCF	w/SCF	w/o SCF	w/SCF
$50^{th}per.$	0.93	1.01	0.81	0.90	1.26	1.04	1.13	0.97
COV	0.13	0.10	0.24	0.19	0.23	0.16	0.23	0.18

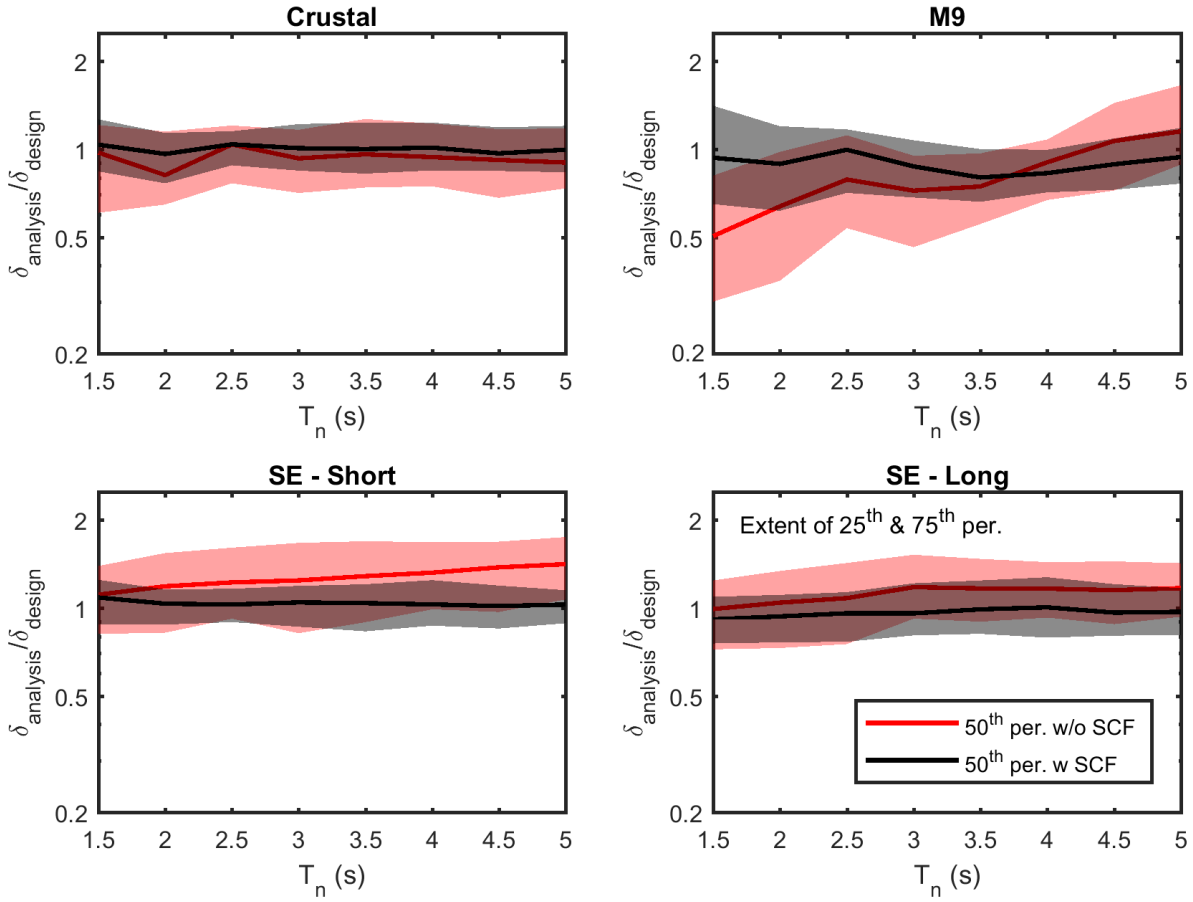

Figure 6.12: Boxplot comparison before and after applying displacement-spectrum shape correction factor (for α equals to 3), varying by equivalent natural period and ground motion dataset.

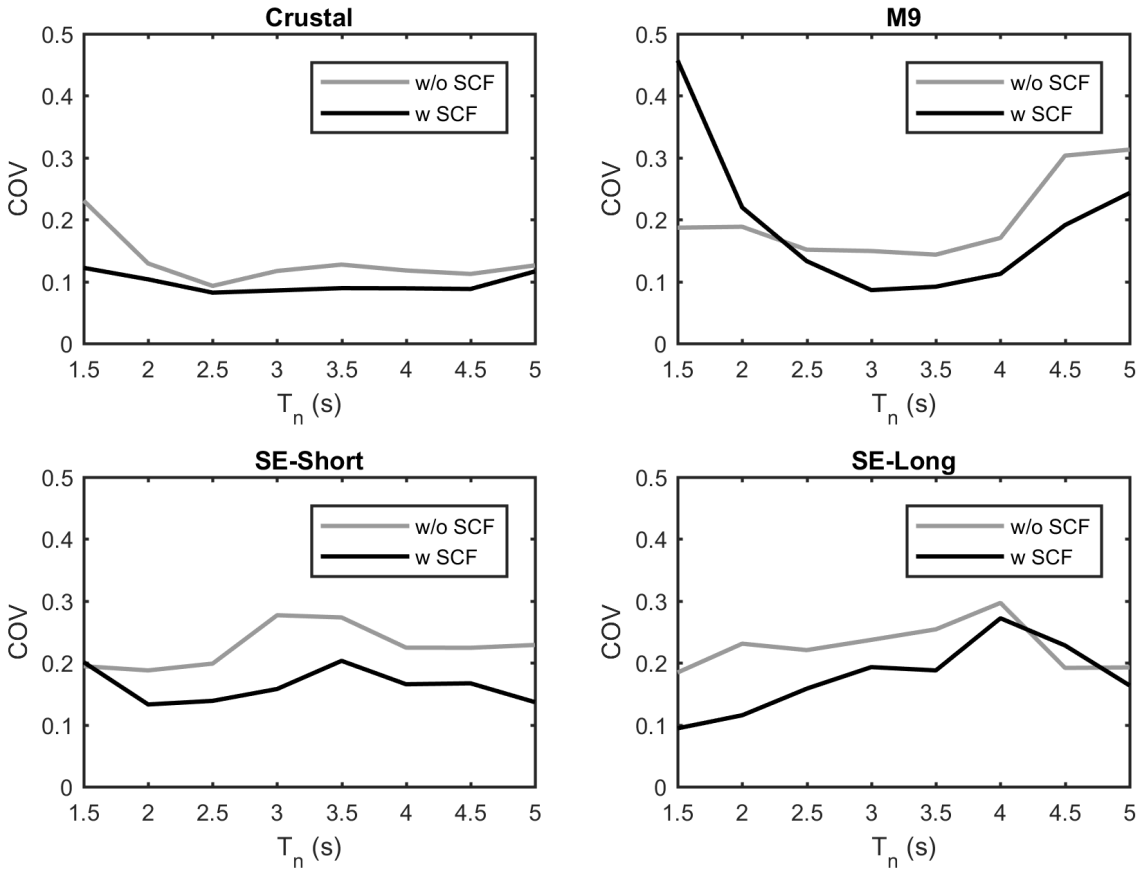

Figure 6.13: Coefficient of variance (COV) comparison before and after applying displacement spectrum shape correction factor, varying by equivalent natural period and ground motion dataset.

The same numerical analyses procedure were also performed using the displacement reduction equation/table provided by Eurocode 8 (2004) [EC8, 2004], and ASCE 7-16 [ASCE, 2017]. As mentioned, only the final outcome is shown in this chapter, detailed results can be found in Appendix C. The calibrated SCFs are shown in Equation 6.8 and Equation 6.9. They yielded similar extent of improvement as those outlined in previous sections, pertaining to systems designed using the displacement reduction equation provided by Eurocode 9 (1994) [EC8, 1994].

$$SCF_{EC8-2004} = e^{-(0.33\alpha-2.44)SS_d+0.30\alpha-2.02} \tag{6.8}$$

$$SCF_{ASCE7-16} = e^{-(0.41\alpha-2.82)SS_d+0.32\alpha-2.07} \tag{6.9}$$

It should be noted that the presented SCF can also be implemented into the iterative procedure outlined in Section 6.2. One could use SCF at the end of each iteration to correct the displacement demand. This corrected value can then be compared with the displacement demand value from the previous iteration. The final displacement demand is determined when it converges to the previous iteration.

6.5 Chapter Conclusions

This chapter evaluated the accuracy of the simplified design method for seismic isolation systems that is the basis for many international code provisions in the context of Friction Pendulum Systems subjected to subduction zone and basin amplified ground motions. The results showed that the simplified method predicts the maximum displacement observed from analysis with insufficient accuracy, producing estimates of peak displacement that are reasonable on-average but with significant scatter. A new correction parameter (i.e. displacement-spectrum shape correction factor) was introduced that improved the accuracy of the simplified design method.

In the current simplified design method, the displacement demand is estimated by linearizing the isolation system characterized by the effective stiffness and the effective damping ratio at the design displacement. The accuracy of this method was evaluated using non-linear time history analyses of FPSs with equivalent natural periods ranging from 1.5 to 5.0 s and equivalent damping ratios ranging from 16% to 32%. These analyses were run for four sets of ground motions from (1) Crustal earthquakes, (2) simulated magnitude-9 earthquakes from the Cascadia Subduction Zone which include deep sedimentary basin effects, (3 & 4) and spectrally equivalent pairs from crustal and subduction zones. Three displacement re-

duction equations/table were considered in this study: (1) Eurocode 8 (1994), which is the same equation recommended by Priestley et al. [2007], (2) Eurocode 8 (2004), and (3) ASCE 7-16. For each of the nonlinear time-history analysis, the ratio between the peak displacement recorded from the analysis and the design displacement was computed. The following conclusions can be drawn from the results of this study:

- For all three considered displacement reduction equations, the simplified method provided good approximations of the median of the maximum displacement when Crustal motion dataset and spectrally equivalent (SE - Long and SE - Short) dataset were used. Of the three displacement reduction equations, for Crustal motion dataset, Eurocode 8 (1994) provided the most accurate results, with a median analysis-to-design ratio of approximately 1.0 for all the equivalent natural periods and damping ratios considered. Eurocode 8 (2004) and ASCE 7-16 yielded conservative results, with median analysis-to-design ratios of 0.85 and 0.78, respectively. For spectrally equivalent dataset, Eurocode 8 (2004) provided the most accurate results, with a median analysis-to-design ratio of approximately 1.0. Eurocude 8 (1994) and ASCE 7-16 had median analysis-to-design ratios of 1.2 and 0.9, respectively.

- The median maximum displacement values from the analyses did not match the design displacement values from nonlinear analysis for the M9 motion dataset for all considered displacement reduction equations/table. For lower equivalent natural periods, the design was overly conservative. In contrast, the simplified method provided unconservative displacement demands at long periods (i.e. 4.5 s and above).

- For all datasets, the overall performance of the simplified method was not sufficient because of the large observed variance in the analysis-to-design ratios (coefficient of variation ranged from 13% to 24%).

To improve the accuracy of the simplified method, a displacement-spectrum shape correction factor was introduced. This shape correction factor takes into account the nonlinearity

of the elastic displacement spectrum at 5% damping ratio, and the effective period and effective damping ratio of the FPS at design displacement. Applying the shape correction factor resulted in analysis-to-design ratios median of 0.99 (from 1.1) and a coefficient of variation of 16% (from 24%), for all considered ground motion datasets.

While the results of this study are intended for use with FPS isolated structures, they may be applicable to other systems characterized by bi-linear hysteresis such as lead-rubber bearings. However, until this is verified as part of future research, the conclusions presented in this paper should be limited to Friction Pendulum Systems.

It should be noted that the modelling methodology for the friction coefficient used in this study does not consider the effect of velocity, pressure, and temperature [Kumar et al., 2015]. Future work shall consider the effectiveness of the proposed shape correction factor in NLTHA with models that account for the effects of velocity, pressure, and temperature.

Chapter 7

CONCLUSIONS

There are several knowledge gaps that are limiting the implementation of friction-type seismic isolation systems. Two were identified and investigated in this dissertation: the first knowledge gap is the uncertain performance of the recently proposed Variable Friction Systems and its application as passive adaptive devices. The second knowledge gap is the unknown impact that ground motions with different characteristics have on friction-type seismic isolation systems, in particular, the Cascadia Subduction Zone (CSZ) Magnitude-9 (M9) ground motion with basin effect.

To address the aforementioned knowledge gaps, this dissertation presented: (i) the development, implementation of Variable Friction Systems; (ii) the performance of Variable Friction Systems as passive adaptive devices; (iii) the evaluation of the impact of ground motions with different characteristics (including the CSZ M9 motions) on the performance and analysis of friction-type base isolation systems.

7.1 Development and Implementation of VFSs

The formulation and implementation of a 3D VF element into OpenSees were presented in Chapter 2. This element is capable of capturing the full static and dynamic responses of VFSs. In order to validate the numerical model, a full-scale VFS prototype was tested in the EUCENTRE under one-directional shaking. The numerical results showed good agreement with the experimental data.

Preliminary 2D and 3D numerical analyses of a 5-story 1-bay case study structure selected from the OpenSees library of examples were performed. The case study structures were isolated using the newly implemented VF element. These analyses served primarily to

demonstrate the use of the new element in the context of NLTH analyses, and to confirm the correct implementation of the element into OpenSees. Furthermore, the results collected showed that, when designed to have the same backbone curve with FPSs, VFSs were able to reduce maximum displacement and maximum base shear demand due to its superior energy dissipation capacity.

7.2 Performance of AVFSs

Chapter 3 introduced AVFSs as passive adaptive devices. It investigated the effect of various design parameters of AVFSs on the demands on the superstructure at different hazard levels through an extensive parametric study.

Both stiff and flexible superstructures (three- and nine-story steel concentrically braced frame building) were considered in this study, each with moderate/long period (3 and 4 s) and high/low damping (25% and 10%) isolation systems.

For all considered cases, the investigated isolation systems were designed to have the same effective isolation properties (T_n and ζ_{eff}). In comparison to FPSs, AVFSs are capable of improving the superstructure performances (reducing PISD and PFA) for frequent earthquakes (both SLE and DBE), while maintaining similar performance during rare events (MCE).

For AVFS-isolated structures, when α_2 increased, the PISD and PFA during frequent earthquakes decreased. However, a large α_2 could result in increased PISD and PFA during rare events. The other design parameter, γ, showed little effect on superstructure performance.

While the results demonstrated the capability of AVFSs to improve the demands on the superstructure. There was a trade-off between maximum isolator displacement and superstructure performance (i.e., peak interstory drift and peak floor acceleration) under different hazard levels. In practice, it would be the building owner's choice on a case-by-case basis to evaluate and mitigate the damage in buildings over a wide range of seismic hazard levels. This study aimed to provide a base isolation system (AVFS) whose performance can

be designed under multiple hazard levels, and to shed light on how the performance are affected by its design parameters.

7.3 Modeling CSS devices with VF element

Another application of the VF element is to model the extra-stroke behavior of Curved Surface Slider (CSS) devices. A recent experimental program [Furinghetti et al., 2020] showed that, for CSS with restraining rims, when the sliding pad traveled beyond the design displacement, it exhibited higher energy dissipation capacity. In fact, the CSS device serendipitously became a Variable Friction System. When the sliding pad traveled across the rim, it essentially was travelling on a high-friction ring zone.

Chapter 4 summarized the experimental results and numerical modeling of CSS under extreme loading conditions. Quasi-static tests and dynamic tests were conducted on several full-scale devices. It was verified that, reaching design displacement did not represent the failure condition of the CSS devices. Extra displacement capacity may be considered when designing/assessing these devices, depending on both the actual size of the sliding pads and the number of sliding surfaces.

When the stainless steel sliding surface was installed with a counterbore gap, a force increase (attributed to higher friction) was seen as the sliding pad exceeds the design displacement. It was possible to model the extra displacement behavior with the VF element described in Chapter 2, which captured the higher friction coefficient that arose when the design displacement was exceeded.

7.4 Impact of the CSZ M9 Motions on the Performance of FPSs

To investigate the impact of the CSZ M9 motions on the performance of FPSs, a large set of SDOF systems were designed based on MCE_R level design spectra and evaluated with the simulated M9 motions. The considered design spectra included: (i) risk-targeted MCE_R design spectrum obtained from NEHRP 2015; (ii) UHS without any basin amplification factors; (iii) UHS with CB14 amplification factors; and (iv) UHS with M9 basin amplification

factors. It was found that, when comparing the 84^{th} percentile maximum displacement values (which has approximately the same return period as the MCE_R level earthquake) with the design displacement demands, group (i) and (ii) (without any basin amplification factors) exceeded the demands. Group (iii) and (iv) (with basin amplification factors) did not.

7.5 Simplified method of analyzing FPSs

In the current simplified method, the displacement demand of FPSs is estimated by linearizing the isolation system using the effective stiffness and the effective damping ratio at design displacement. The accuracy of this method was evaluated using NLTHA of FPSs with equivalent natural periods ranging from 1.5 to 5.0 s and equivalent damping ratios ranging from 16% to 32%. These analyses were run for four sets of ground motions from (1) Crustal earthquakes, (2) simulated magnitude-9 earthquakes from the Cascadia Subduction Zone which include deep sedimentary basin effects, (3 & 4) and spectrally equivalent pairs from crustal and subduction zones. Three displacement reduction equations/table were considered in this study: (1) Eurocode 8 (1994), which is the same equation recommended by Priestley et al. [2007], (2) Eurocode 8 (2004), and (3) ASCE 7-16. For each analysis, the ratio between the peak displacement recorded from the analysis and the design displacement was recorded.

It was found that, from the median analysis-to-design ratio, the simplified method provides a good approximation for group (i), (iii), and (iv). However, it did not work well for group (ii), the simulated M9 motions. For lower equivalent natural period systems, the design was overly conservative. In contrast, at longer periods (4.5 s and above), the simplified method provided unconservative displacement demand. In addition, for all datasets, the overall performance of the simplified method was not sufficient because of the large observed variance in the analysis-to-design ratios (coefficient of variation ranged from 13% to 24%)

To improve the accuracy of the simplified method, a displacement-spectrum shape correction factor was introduced. This shape correction factor takes into account the nonlinearity of the elastic displacement spectrum at 5% damping ratio, and the effective period and effective damping ratio of the FPS at design displacement. Applying the shape correction factor

significantly improved the accuracy of the simplified method for the simulated M9 motions. It also reduced the coefficient of variation for each group by over 20%.

Appendix A

OVERVIEW OF MULTIPLE FRICTION PENDULUM SYSTEMS

Stemming from the desire to limit the size of the device for the friction pendulum while increasing the displacement capacity, Tsai et al. [2003a], Tsai et al. [2003b], Tsai et al. [2004] proposed the spherical double concave friction pendulum system (DCFP) named multiple friction pendulum system. Analytical behavior of DCFP was proposed, and was validated experimentally. However, the proposed analytical model was limited to the condition that the top and bottom surface have the same radius of curvature and same frictional properties, implying that the slider simultaneously slides on both concave surfaces when the sliding motion is activated. Fenz and Constantinou [2006] developed a more general theoretical model for DCFP accounting for: (1) unequal radii of curvature and/or coefficients of friction of the two sliding surface; (2) the effect of the height of the articulated slider; (c) the effect of friction in the rotational part of the articulated slider on the hysteretic behavior. As shown in Figure A.1, the effective radius of curvature taking into account the effect of the height of the articulated slider becomes $R_i - h_i$ instead of just the radius of curvature of the sliding surface. It is worth noting that in the special case mentioned above when the top and bottom sliding surface have the same properties (i.e. $R_1 = R_2 = R$ and $h_2 = h_1 = h$), the hysteretic behavior of the DCFP can be represented by that of a Friction Pendulum system with effective radius of curvature equals to $2(R - h)$. Bearing tests were conducted to validate the proposed theoretical model. However, the bearing tests were conducted under relatively low velocity (peak velocity equals to 63 mm/s).

By adding another set of surfaces on the top and the bottom of DCFP, Fenz and Constantinou [2008d], Fenz and Constantinou [2008c] proposed the triple friction pendulum

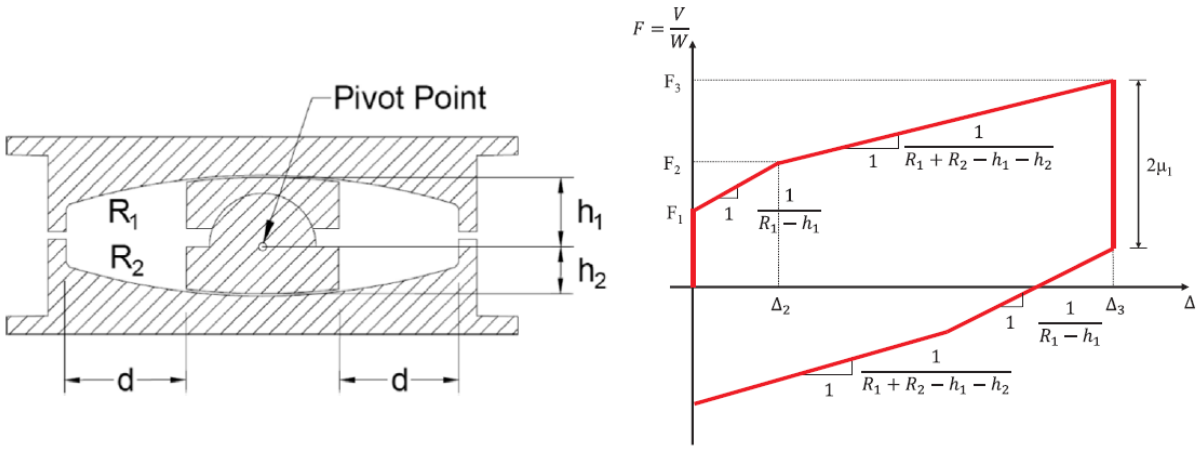

Figure A.1: Schematic drawing of a double concave friction pendulum and its typical hysteretic behavior. Picture retrieved from [Calvi and Calvi, 2018]

(TFP). The TPS is a passive adaptive device that is capable of having optimized behavior for multiple performance objectives under multiple intensities of ground motion. Based on Kelly [1999] and Hall [1999], an optimal adaptive device should exhibit: (1) very stiff response with low damping at low-level of shaking; (2) softer response with increasing damping at the design basis earthquake (DBE); (3) further stiffness reduction with increasing damping in the maximum considered event (MCE), and (4) high stiffness as the MCE demand is exceeded. The force displacement relationship of a TFP that exhibits such behaviors is shown in Figure A.2. It should be noted that this adaptive hysteretic behavior can only be achieved setting specific relationships between the geometric properties and frictional properties of the four sliding surfaces (detailed requirements can be found in [Fenz and Constantinou, 2008d]).

To enable the numerical investigation of TFP bearings and TFP base isolated structures, in the context of non-linear time history analysis, Fenz and Constantinou [2008b] proposed a model to represent the hysteresis of TFP. More recently, Dao et al. [2013] implemented this model into OpenSees as a single 3D TFP bearing, which improved the numerical convergence of the algorithm. It also includes a circular gap formulation that improved its accuracy and a variable friction formulation that takes into account the simultaneous influence of

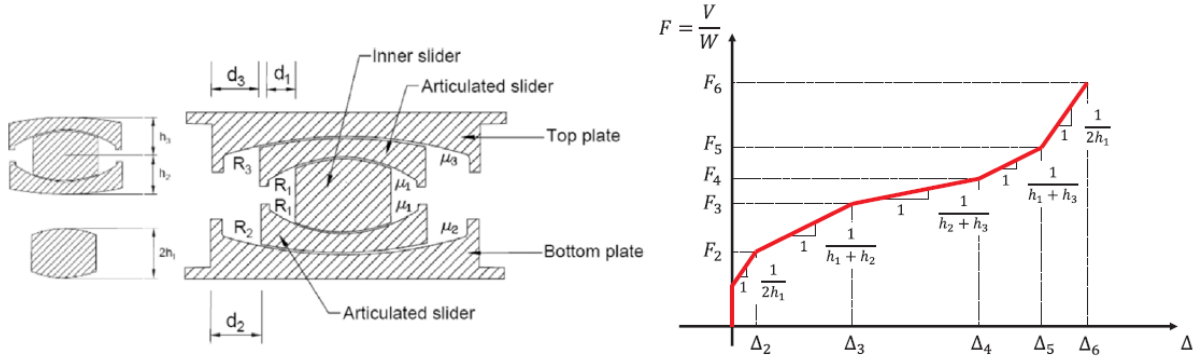

Figure A.2: Schematic drawing of a triple friction pendulum and its typical hysteretic behavior. Picture retrieved from [Calvi and Calvi, 2018]

velocity and axial force on the coefficient of friction. However, this model does not track the movement of the individual components of the TFP, thus it is challenging to iterate friction forces between each sliding surfaces based on the instant velocity of each individual component. To attempt to tackle this issue, Dao et al. [2013] back-calculated the sliding velocities of each component and proposed a friction model specific for TFP. Becker and Mahin [2012] developed a non-linear kinematic model that can simulate the response of TFP without restraints on the geometric or friction properties. The model is also able to track the motion of each component of the TFP instead of only being able to track the overall displacement of the top surface. The model was slightly modified in [Becker and Mahin, 2013b] by adding the capability to account for the rotation of the internal components of TFP. However, all the existing models were developed based on the assumption that the resultant force of the contact pressure acts at the center of each sliding surface. Sarlis and Constantinou [2016] revised the model such that no assumptions are made on the location of the resultant forces at each sliding surface.

It is worth noting that all the analytical/numerical models described, through proper setting of the various parameters, can be used to simulate the response of DCFP and FPS as well.

Besides the analytical and numerical studies, a few experimental programs have been conducted to study the response and characterize the behavior of TFPs. Bearing tests were first conducted by Fenz and Constantinou [2008c]. While most tests were conducted at very low speed (peak velocity equals to 6.3 mm/s), there were a few under high speed (peak velocity up to 400 mm/s). However, the hysteretic loops under high speed tests were somewhat different from what was expected due to the velocity dependence of coefficients of friction, which tends to mask the transitions in stiffness. Fenz and Constantinou [2008a] conducted shake table testing of a quarter-scale, 6-story steel structure isolated with TFP. The outcome of the experimental program demonstrated that the use of TFP systems can significantly enhance the structural performance. In addition, the test results served as a validation of the TFP numerical models previously proposed. However, nontrivial discrepancies between numerical predictions and experimental observations were observed with respect to the floor accelerations. Morgan and Mahin [2011] tested a small three-story concentrically braced steel frame building isolated with TFPs subjected to simple harmonic excitation. The results showed good agreement between the numerical predictions and the experimental outcome. Becker and Mahin [2012], Becker et al. [2012] conducted an extensive experimental program on TFP with a mass placed on top of the bearing using controlled-displacement orbits to investigate the behavior of TFPs; a study on the effect of mass offset on the torsional response in TFP was also included. Ponzo et al. [2014] conducted a shake table test of a 1/3-scaled steel framed structure with one-story and one-bay isolated with DCFP with equal properties of the concave sliding surfaces. The test results showed that the dynamic behavior of DCFP bearings was both reliable over many input motions and repeatable even when initial slider offsets are present. In 2011, a full-scale 5-story steel moment frame building was tested at E-Defense with three different support configurations (TFP; lead-rubber bearing in combination with cross linear bearings; and in a fixed-base condition). Non-structural components and content were installed on the fourth and fifth floors. Ryan et al. [2012] presented the detailed information about the test program. A three-dimensional numerical model was built and the effect of different modeling assumptions on the behavior of the numerical predic-

tion in comparison with the experimental results are presented in [Dao and Ryan, 2014]. In particular, the influence of the vertical component of ground acceleration on the horizontal response of the structure was investigated both analytically and numerically in [Ryan and Dao, 2016]. More recently, Becker et al. [2017] investigated the extreme behavior of TFP through a shake table test of a 1/3-scaled 2-story and 2-bay steel structure. The numerical model they previously proposed was revised to incorporate the effects of impact loads and bearing uplift phenomena. Some experimental evidence on the impact force was collected. However, the focus of the experiments was to investigate the failure mode of TFP isolated structures.

While most of the study on multiple friction pendulum systems were focused on the investigation of TFP isolated structures, relatively few have been done on the DCFP. It should be noted that when using different frictional properties and geometric properties (including the displacement capacity, i.e. radius of the sliding plate) of the top and bottom sliding surfaces, DCFP can be used to achieve adaptive behavior. Fenz and Constantinou [2008c] conducted a few bearing tests of DCFP with different radii of curvature and coefficients of friction under very low speed cyclic loading. Kim and Yun [2007] investigated the seismic response characteristics of bridges using DCFP with adaptive behavior and found that the base shear on the pier were consistently smaller than DCFP without adaptive behavior characteristics, particularly under moderate to frequent earthquakes. Malekzadeh and Taghikhany [2010] further explored the response of adaptive DCFPs with respect to that of traditional FPSs. A one-story structure was modeled numerically and subjected to ground motions at SLE, DBE, and MCE levels. The results showed that when a DCFP is designed to experience the same median isolator displacement as its FPS counterpart under MCE hazard level, higher performance can be achieved. In particular, the use of DCFP resulted in a reduction of the peak floor acceleration and peak inter-story drift at SLE and DBE hazard levels.

Appendix B

COMPLETE NUMERICAL RESULTS FOR CHAPTER 3

This appendix provides the complete numerical results for Chapter 3.

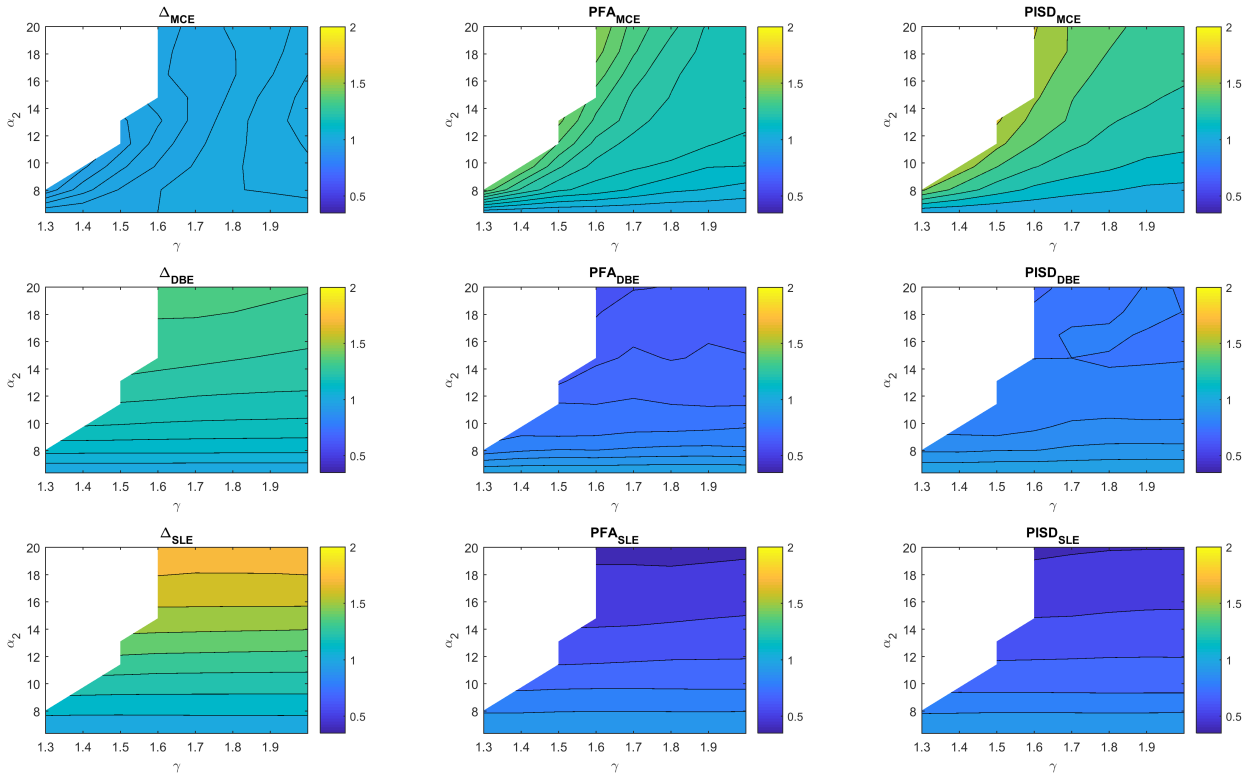

Figure B.1: Mean demand (of three hazard levels) for Δ_{iso} (left), PFA (center), PISD (right) for three-story isolated buildings with isolation systems that have $T_n = 4$ sec and $\zeta = 10\%$.

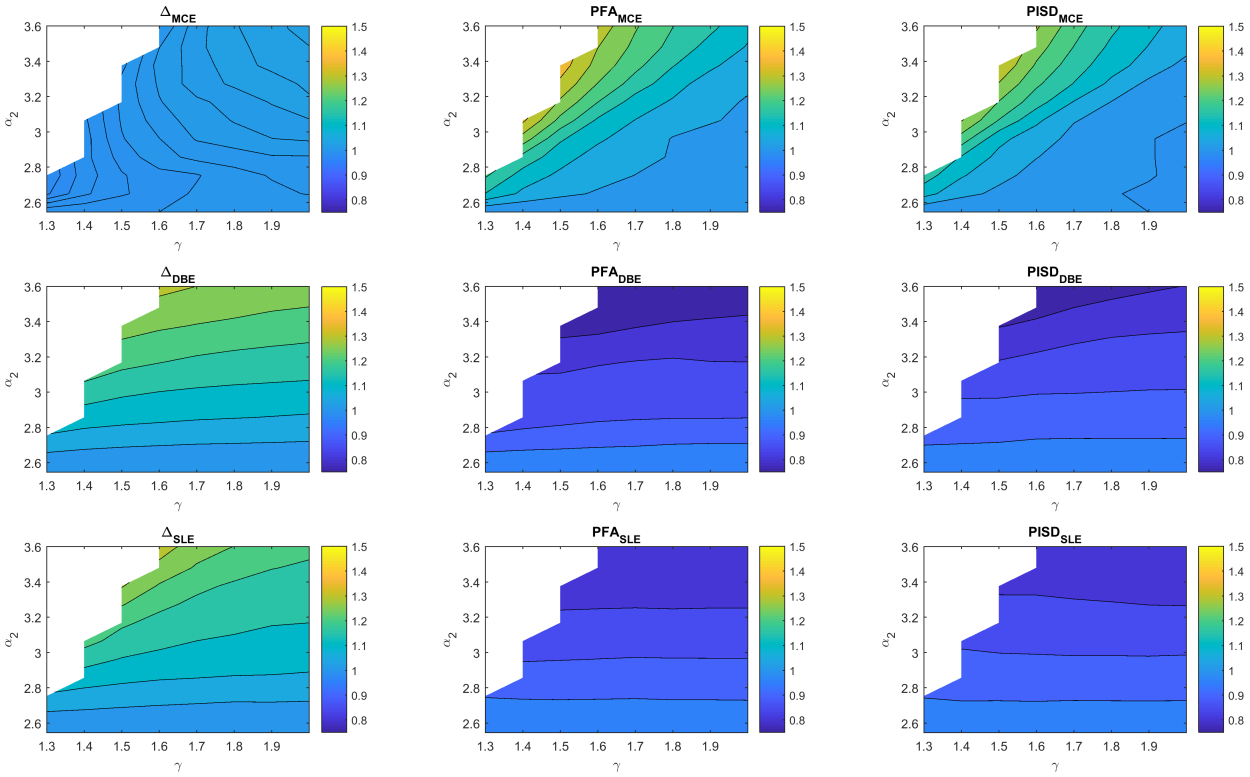

Figure B.2: Mean demand (of three hazard levels) for Δ_{iso} (left), PFA (center), PISD (right) for three-story isolated buildings with isolation systems that have $T_n = 4$ sec and $\zeta = 25\%$.

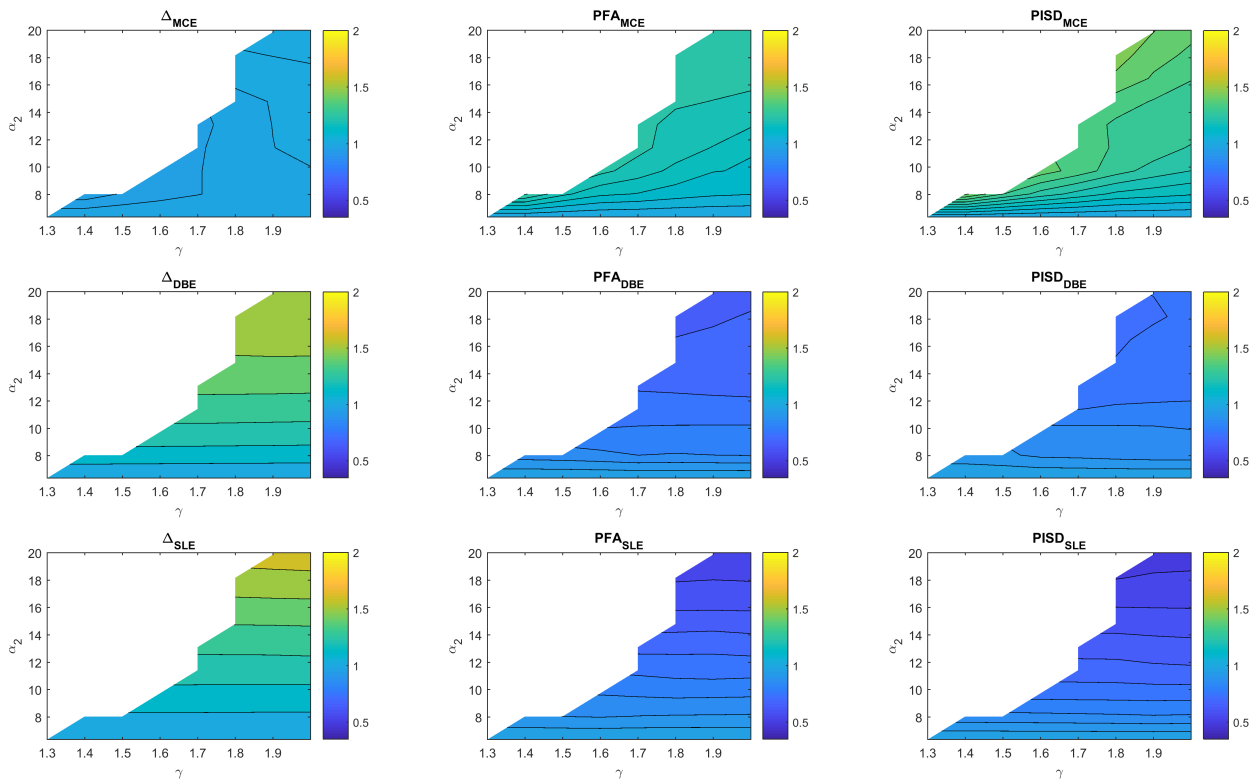

Figure B.3: Mean demand (of three hazard levels) for Δ_{iso} (left), PFA (center), PISD (right) for nine-story isolated buildings with isolation systems that have $T_n = 3$ sec and $\zeta = 10\%$.

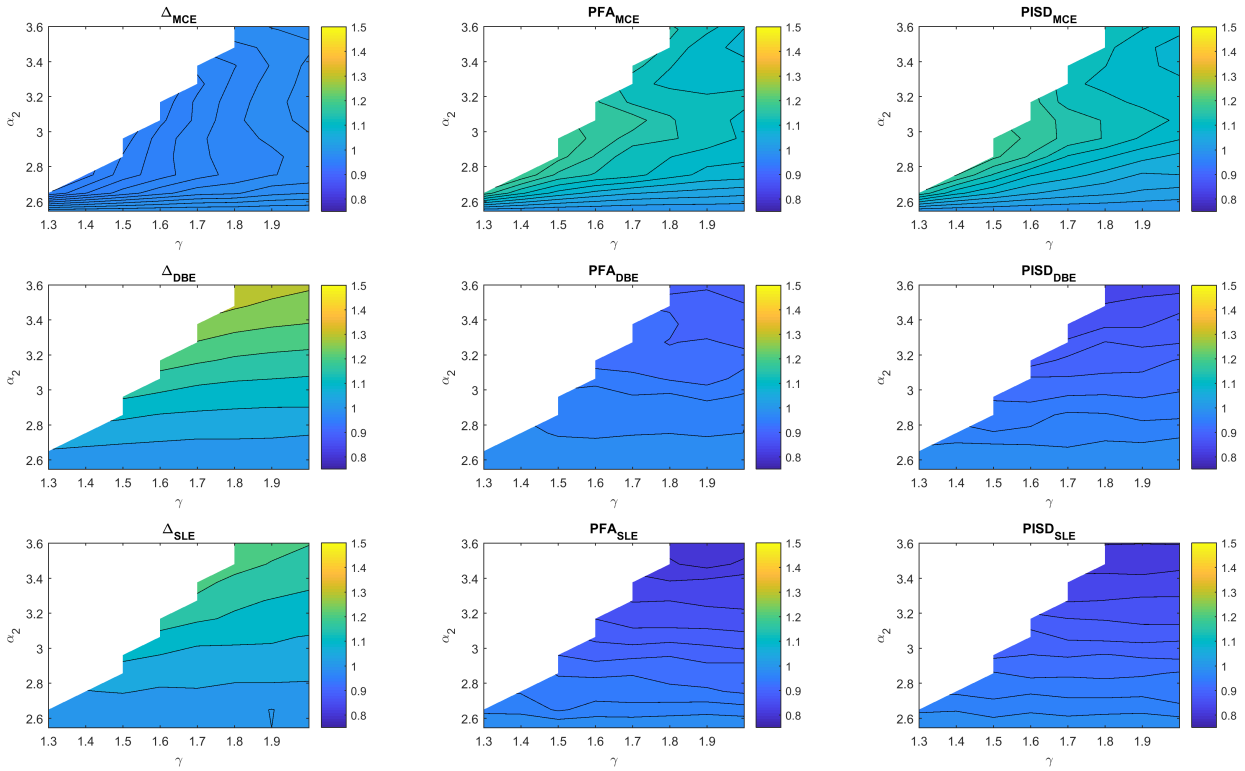

Figure B.4: Mean demand (of three hazard levels) for Δ_{iso} (left), PFA (center), PISD (right) for nine-story isolated buildings with isolation systems that have $T_n = 3$ sec and $\zeta = 25\%$.

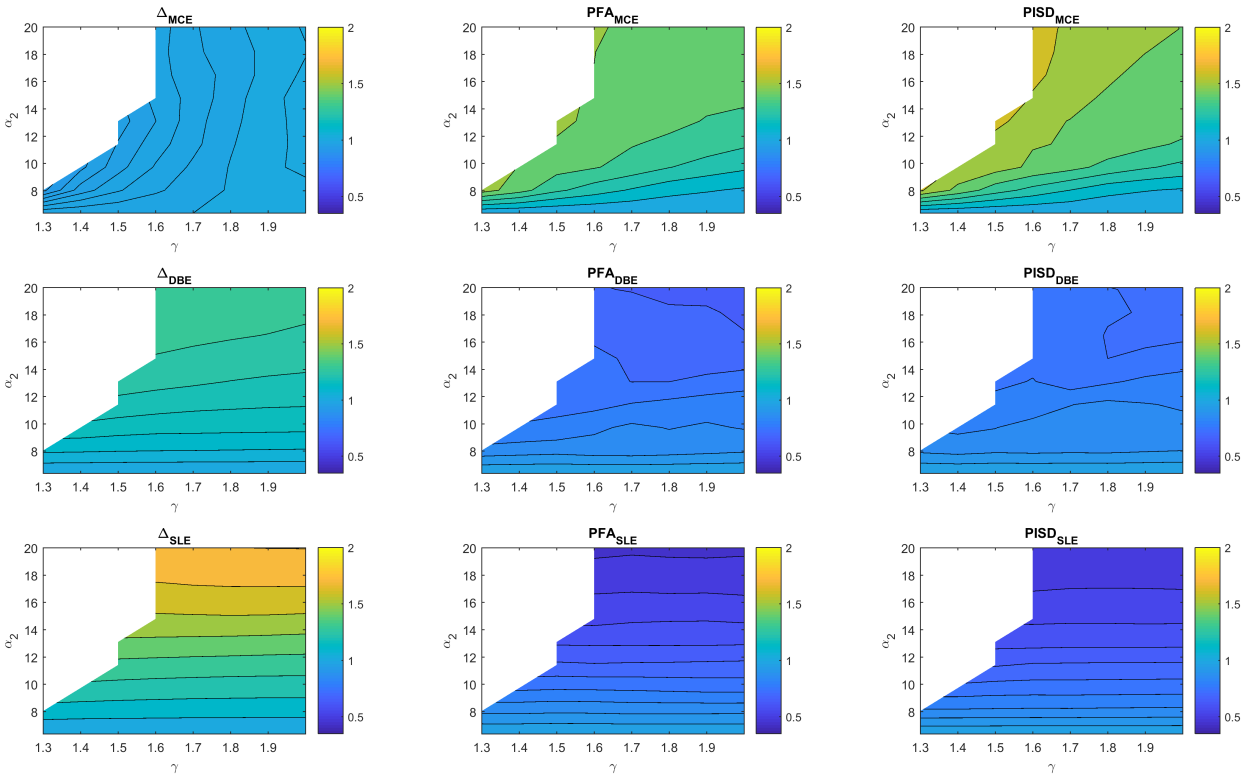

Figure B.5: Mean demand (of three hazard levels) for Δ_{iso} (left), PFA (center), PISD (right) for nine-story isolated buildings with isolation systems that have $T_n = 4$ sec and $\zeta = 10\%$.

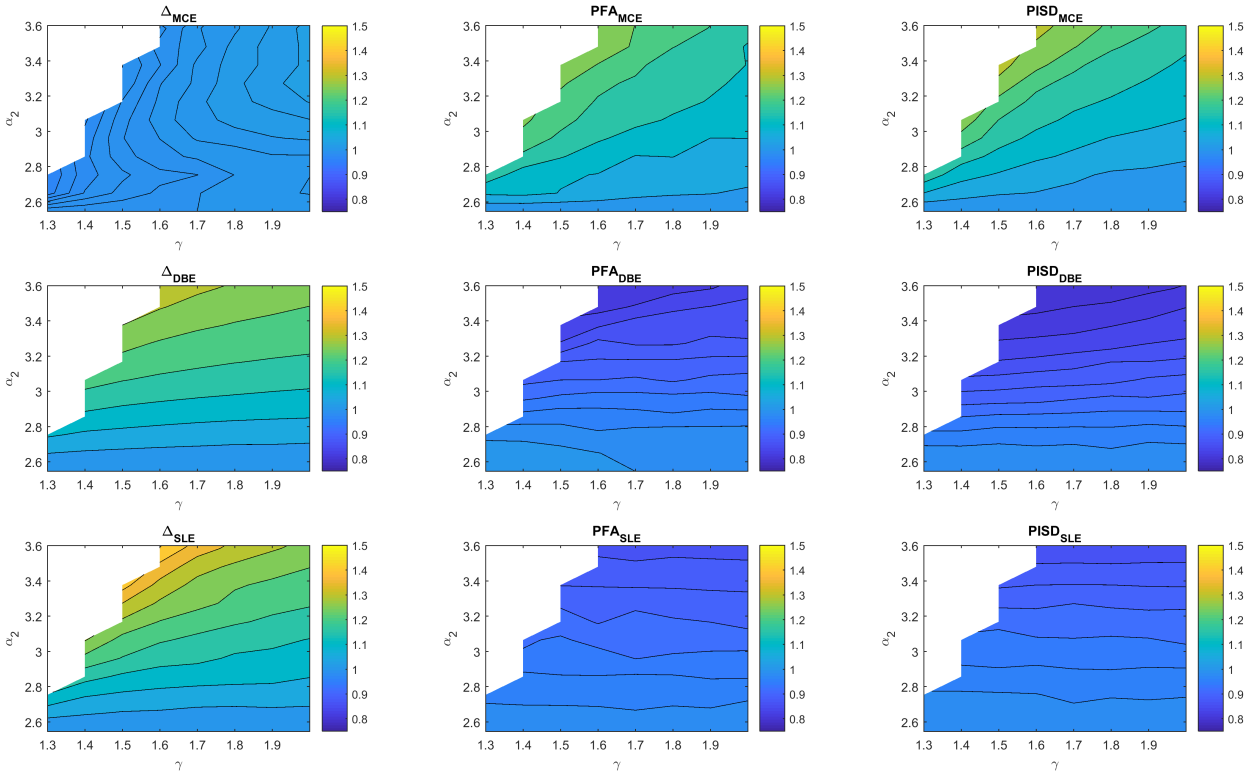

Figure B.6: Mean demand (of three hazard levels) for Δ_{iso} (left), PFA (center), PISD (right) for nine-story isolated buildings with isolation systems that have $T_n = 4$ sec and $\zeta = 25\%$.

Appendix C

COMPLETE NUMERICAL RESULTS FOR CHAPTER 6

This appendix provides the numerical results for Chapter 6. Figure C.1 to Figure C.12 present the numerical results pertaining to α equals to 2, 2.5, 3.5, and 4 when the displacement reduction equation from Eurocode 8 (1994) is used.

For brevity, only the plots (Figure C.13 to Figure C.24) for linear regression coefficients and the final results comparison are shown here pertaining to numerical analyses with displacement reduction equation/table provided by Eurocode 8 (2004) and ASCE 7-16.

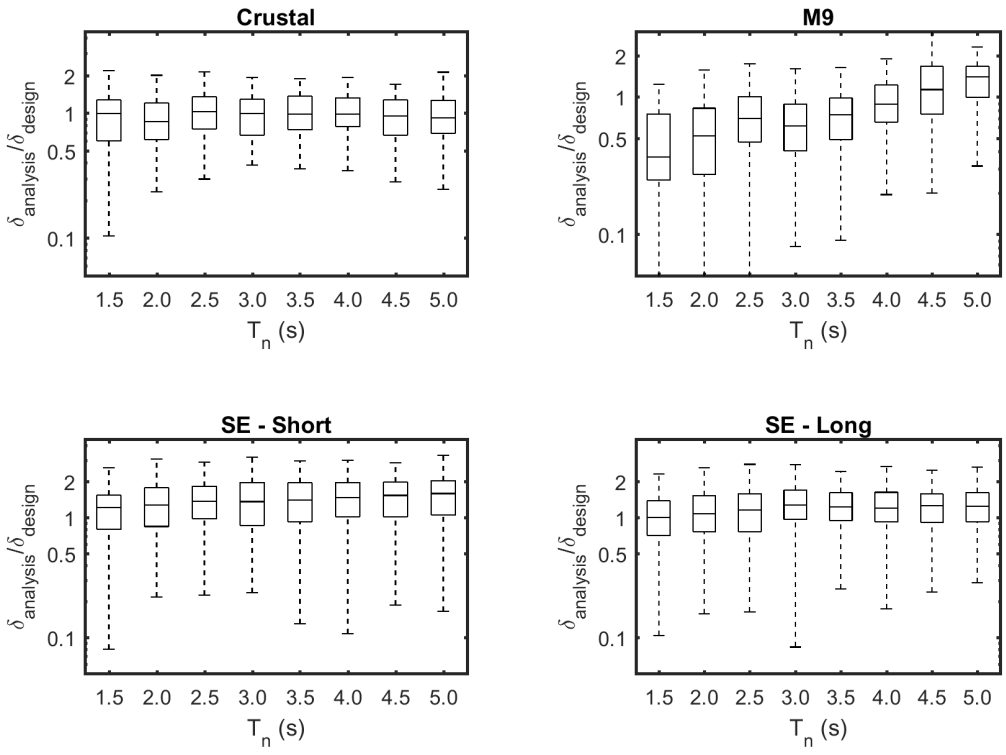

Figure C.1: Numerical results (for α equals to 2) of the ratio (in log-scale) between maximum absolute displacement from NLTHA and design displacement varying by design period for each ground motion dataset.

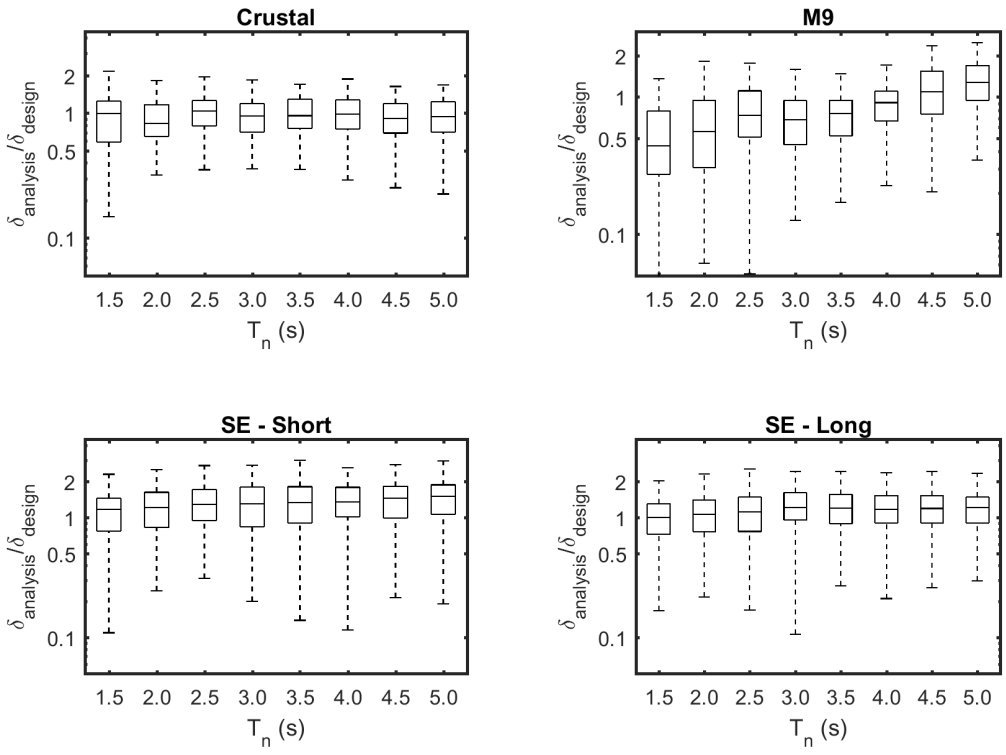

Figure C.2: Numerical results (for α equals to 2.5) of the ratio (in log-scale) between maximum absolute displacement from NLTHA and design displacement varying by design period for each ground motion dataset.

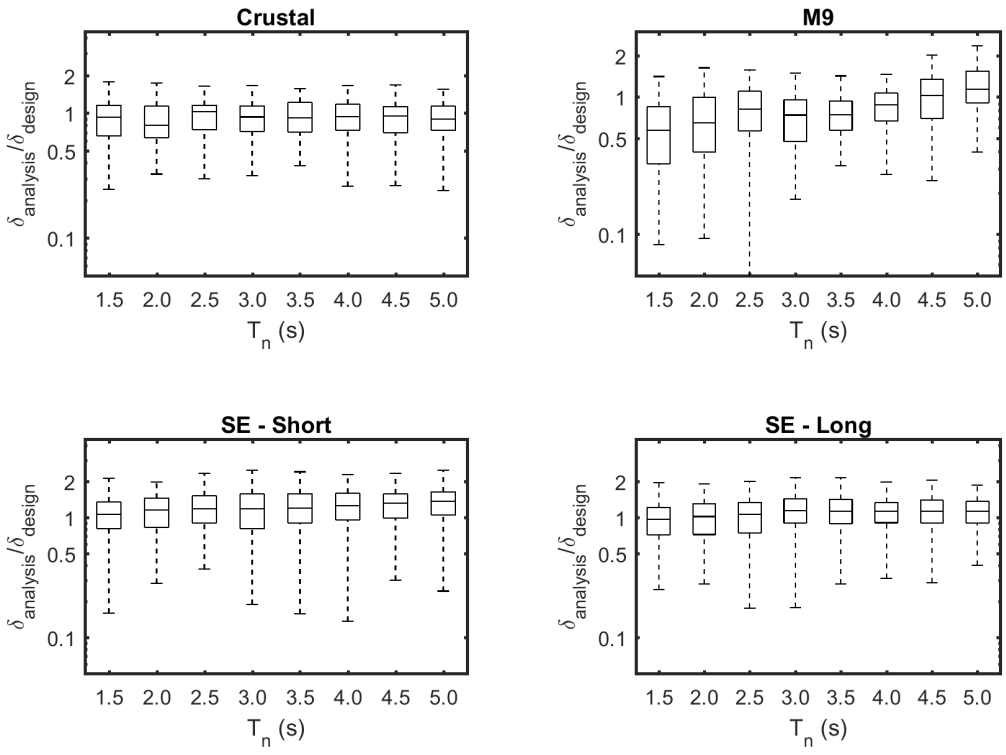

Figure C.3: Numerical results (for α equals to 3.5) of the ratio (in log-scale) between maximum absolute displacement from NLTHA and design displacement varying by design period for each ground motion dataset.

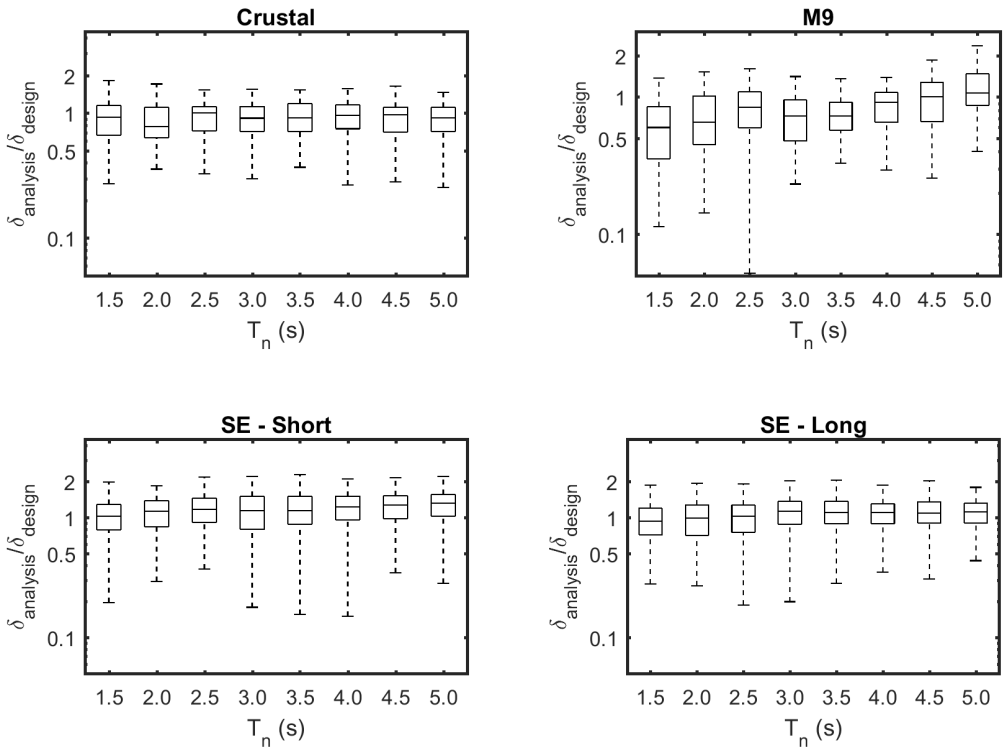

Figure C.4: Numerical results (for α equals to 4) of the ratio (in log-scale) between maximum absolute displacement from NLTHA and design displacement varying by design period for each ground motion dataset.

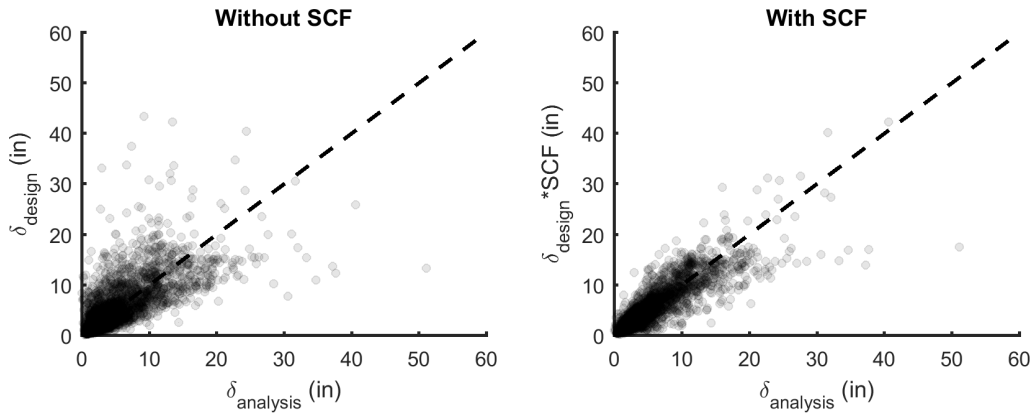

Figure C.5: Comparison of maximum absolute displacement from analysis and design displacement for all periods and ground-motion sets (α equals to 2) (Crustal, M9, SE - Short, SE - Long) (a) without applying SCF and (b) with applying SCF.

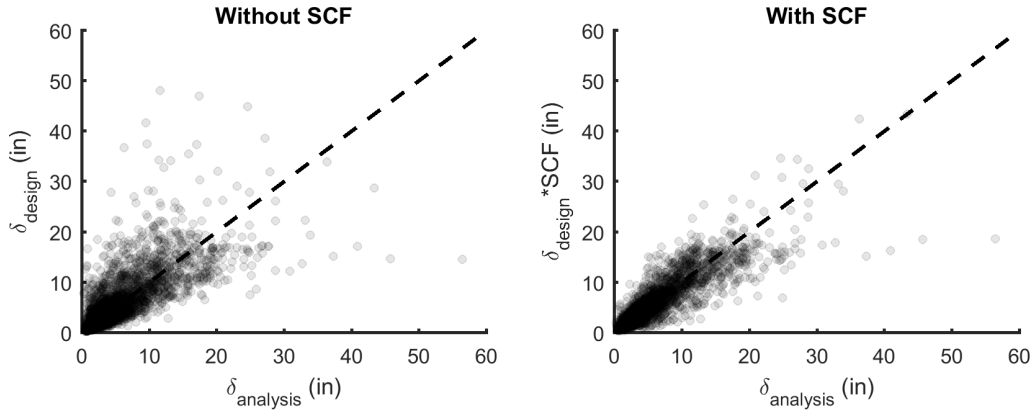

Figure C.6: Comparison of maximum absolute displacement from analysis and design displacement for all periods and ground-motion sets (α equals to 2.5) (Crustal, M9, SE - Short, SE - Long) (a) without applying SCF and (b) with applying SCF.

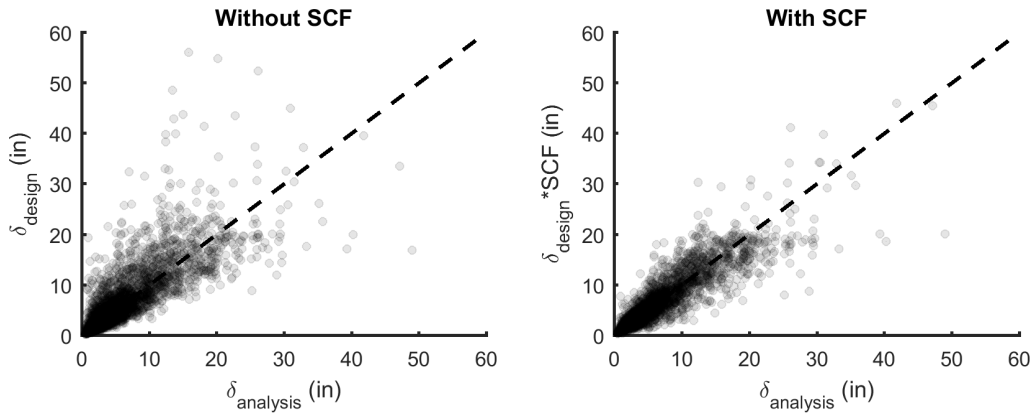

Figure C.7: Comparison of maximum absolute displacement from analysis and design displacement for all periods and ground-motion sets (α equals to 3.5) (Crustal, M9, SE - Short, SE - Long) (a) without applying SCF and (b) with applying SCF.

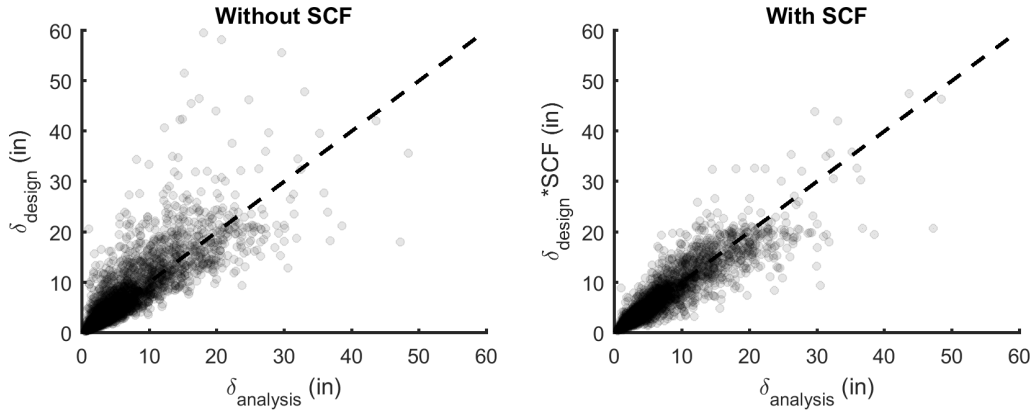

Figure C.8: Comparison of maximum absolute displacement from analysis and design displacement for all periods and ground-motion sets (α equals to 4) (Crustal, M9, SE - Short, SE - Long) (a) without applying SCF and (b) with applying SCF.

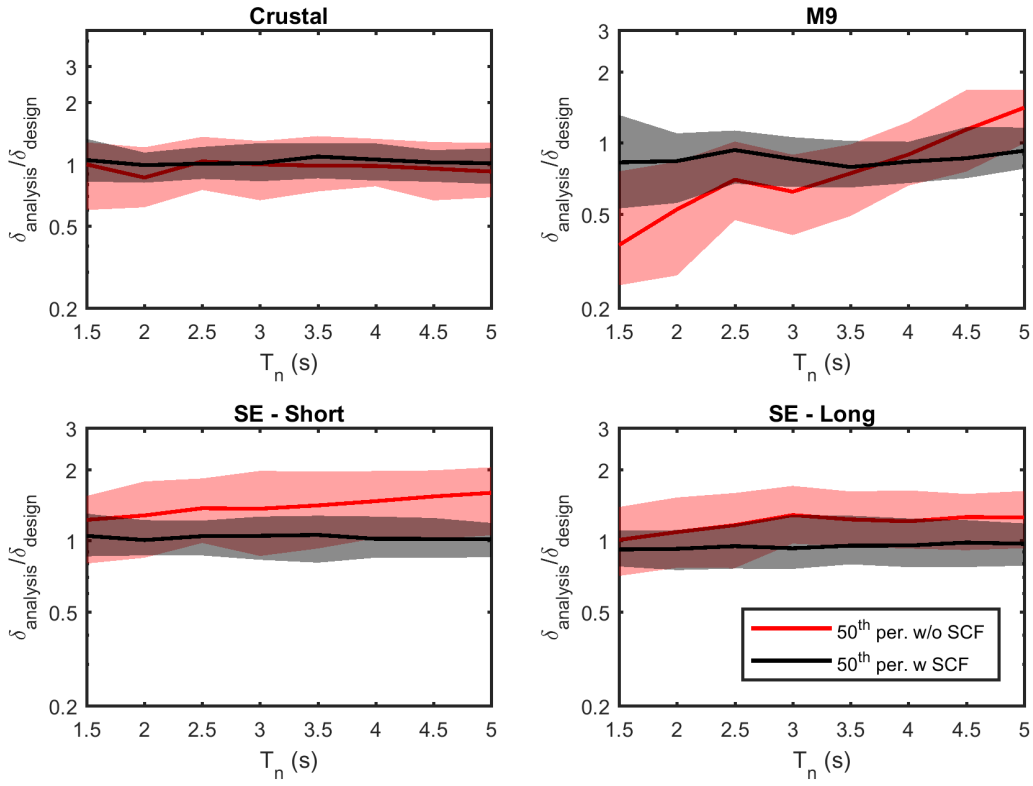

Figure C.9: Boxplot comparison before and after applying displacement-spectrum shape correction factor (for α equals to 2), varying by equivalent natural period and ground motion dataset.

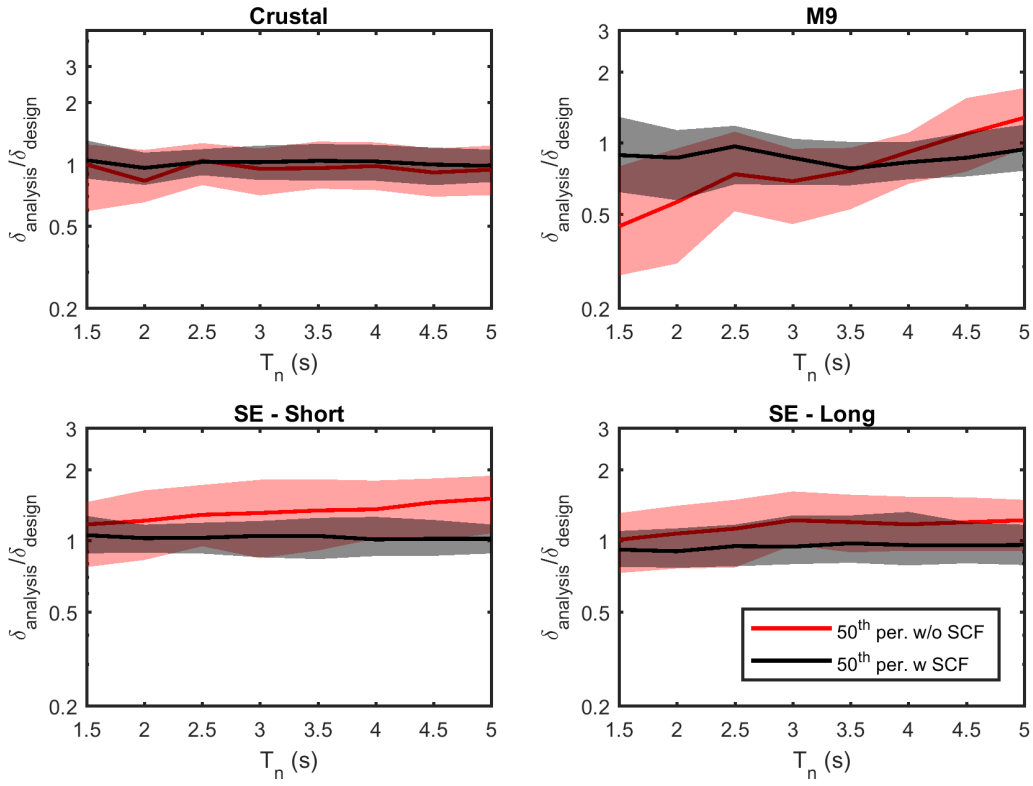

Figure C.10: Boxplot comparison before and after applying displacement-spectrum shape correction factor (for α equals to 2.5), varying by equivalent natural period and ground motion dataset.

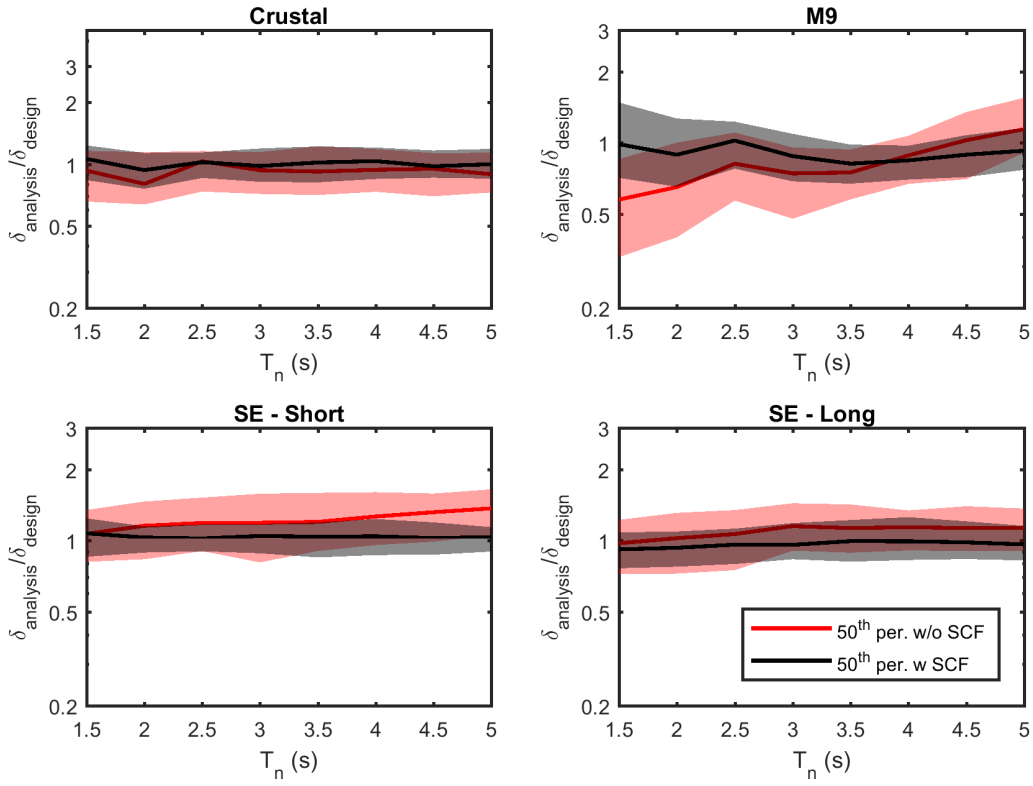

Figure C.11: Boxplot comparison before and after applying displacement-spectrum shape correction factor (for α equals to 3.5), varying by equivalent natural period and ground motion dataset.

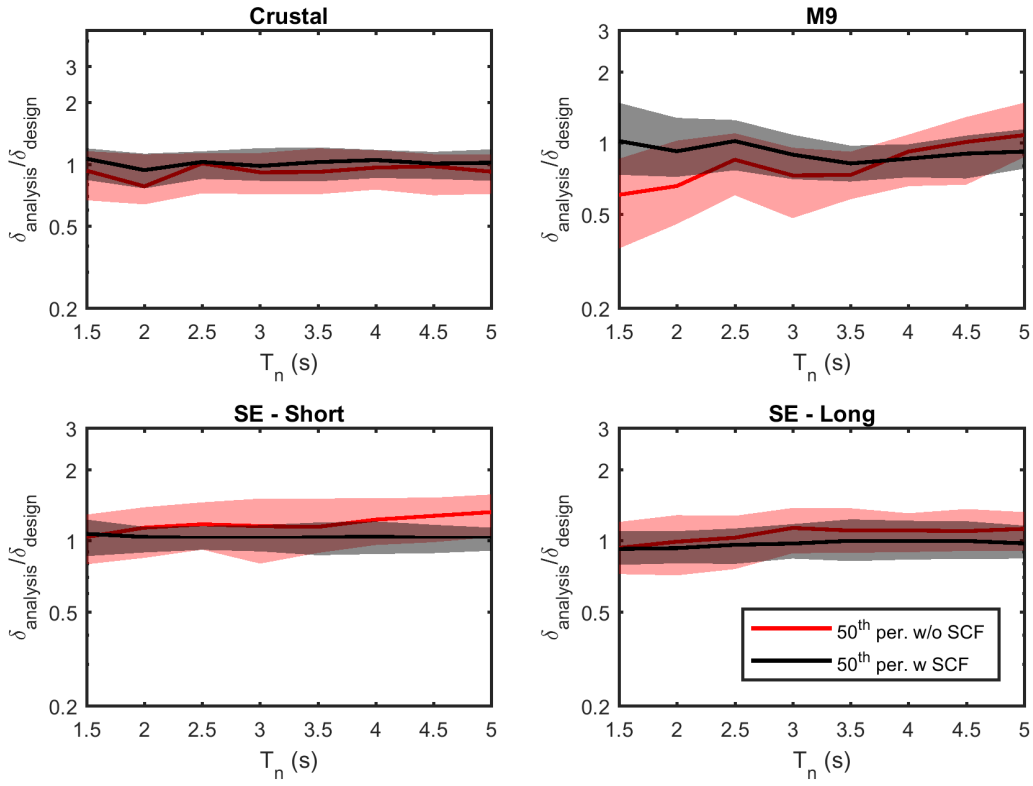

Figure C.12: Boxplot comparison before and after applying displacement-spectrum shape correction factor (for α equals to 4), varying by equivalent natural period and ground motion dataset.

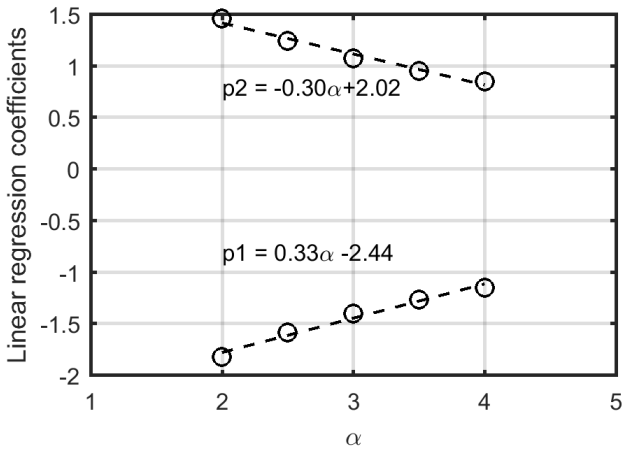

Figure C.13: Relationship between α and the linear regression coefficients for Eurocode 8 (2004)

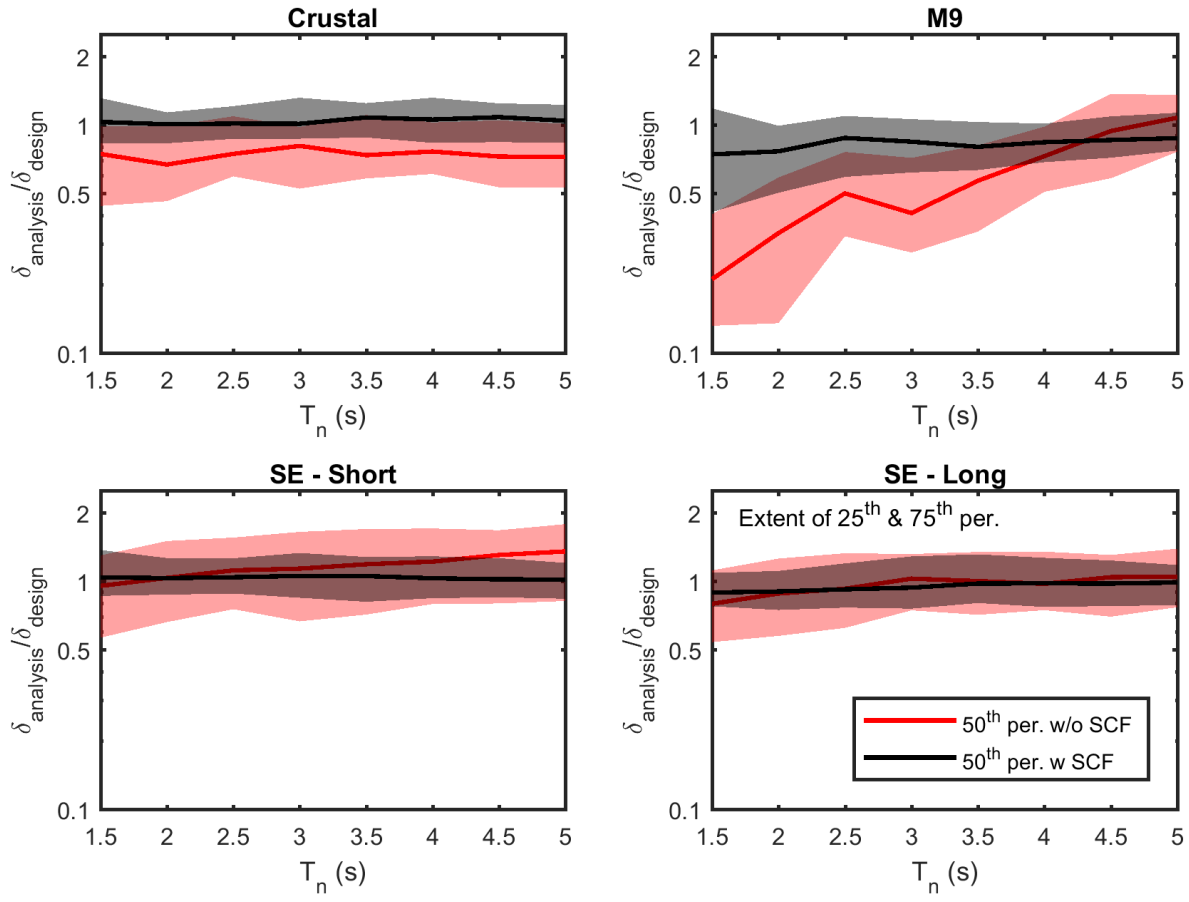

Figure C.14: Boxplot comparison before and after applying displacement-spectrum shape correction factor (α equals to 2) for Eurocode 8 (2004)

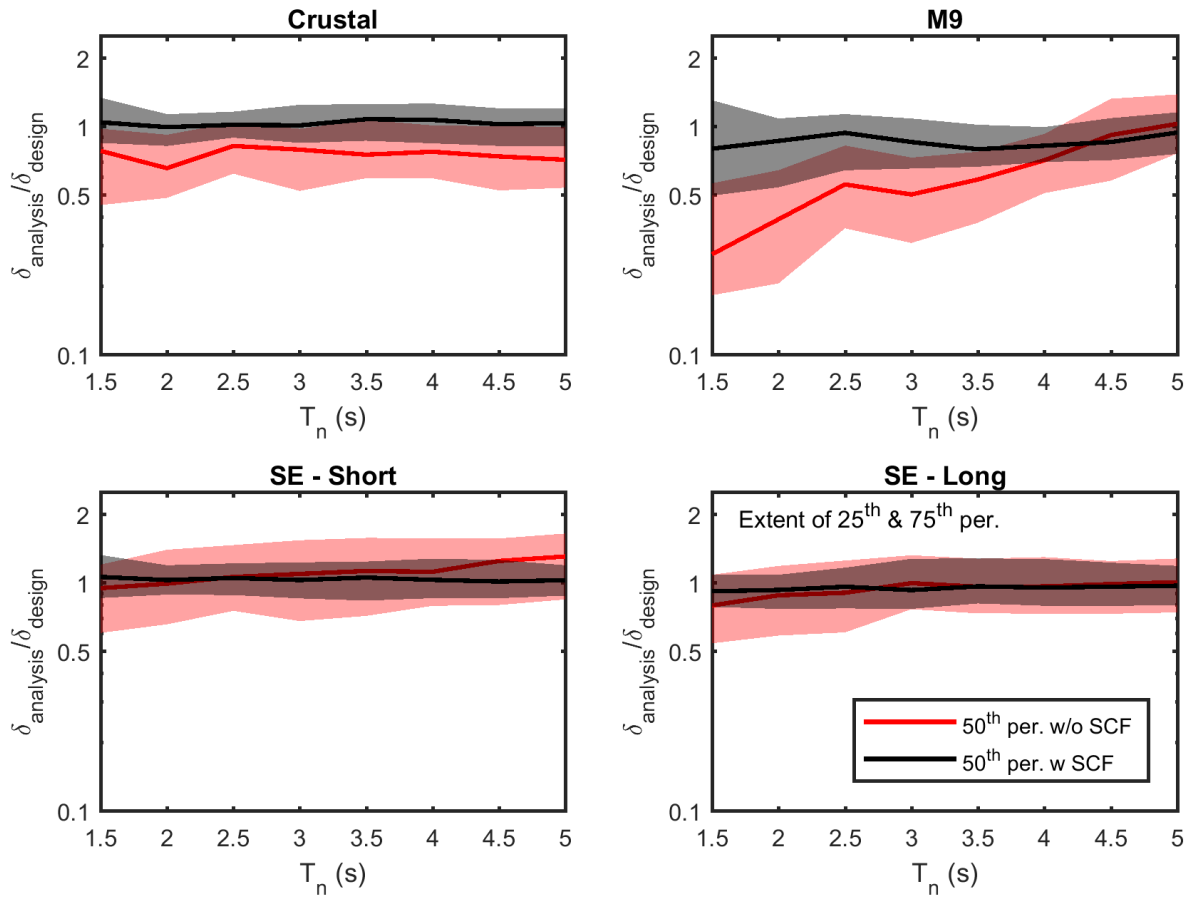

Figure C.15: Boxplot comparison before and after applying displacement-spectrum shape correction factor (α equals to 2.5) for Eurocode 8 (2004)

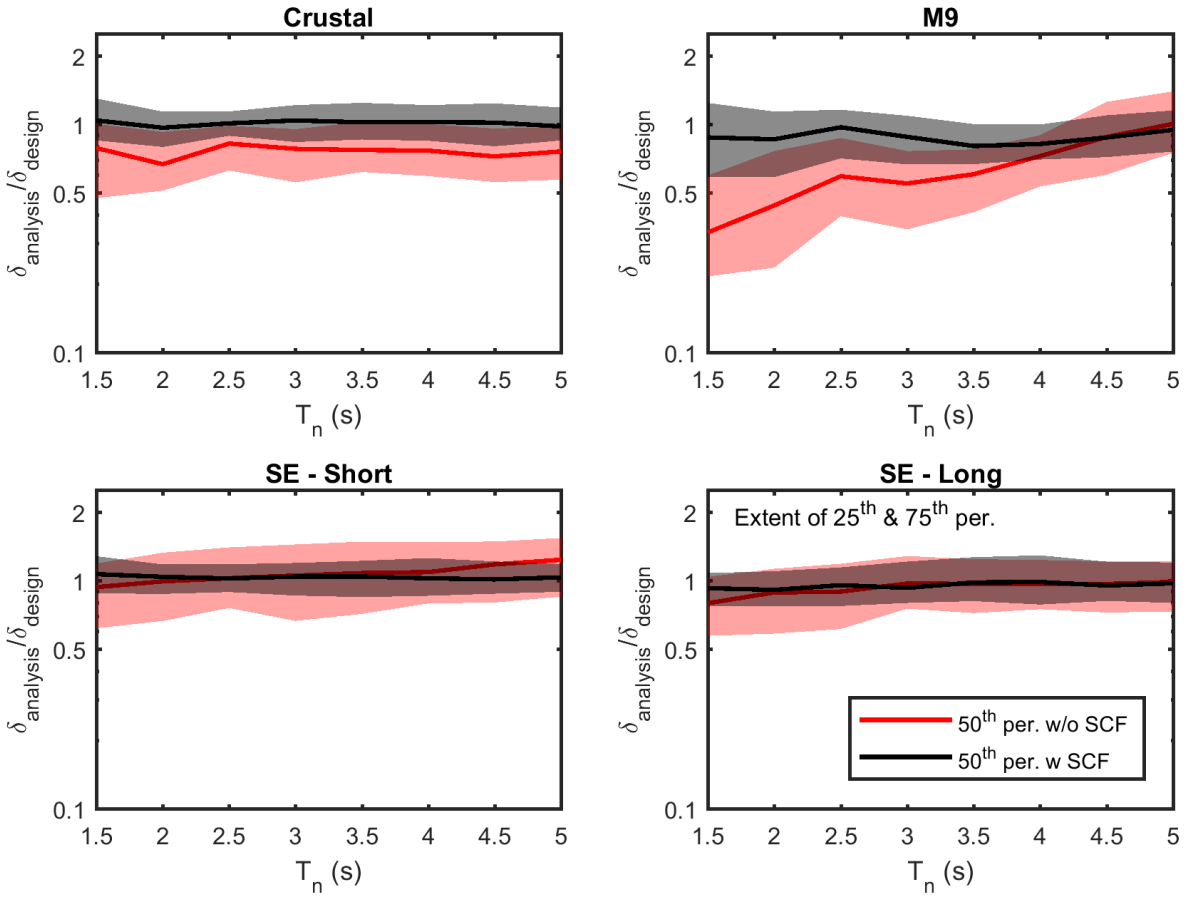

Figure C.16: Boxplot comparison before and after applying displacement-spectrum shape correction factor (α equals to 3) for Eurocode 8 (2004)

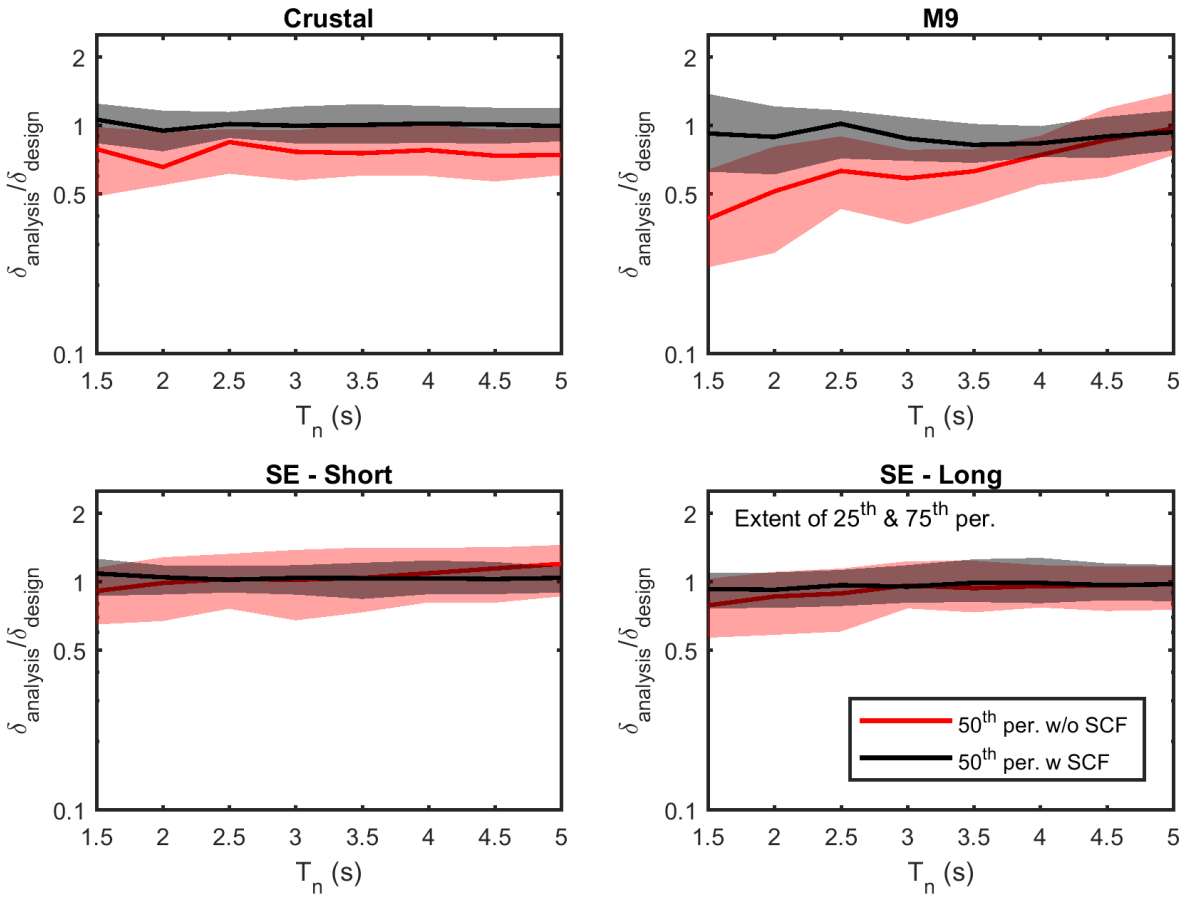

Figure C.17: Boxplot comparison before and after applying displacement-spectrum shape correction factor (α equals to 3.5) for Eurocode 8 (2004)

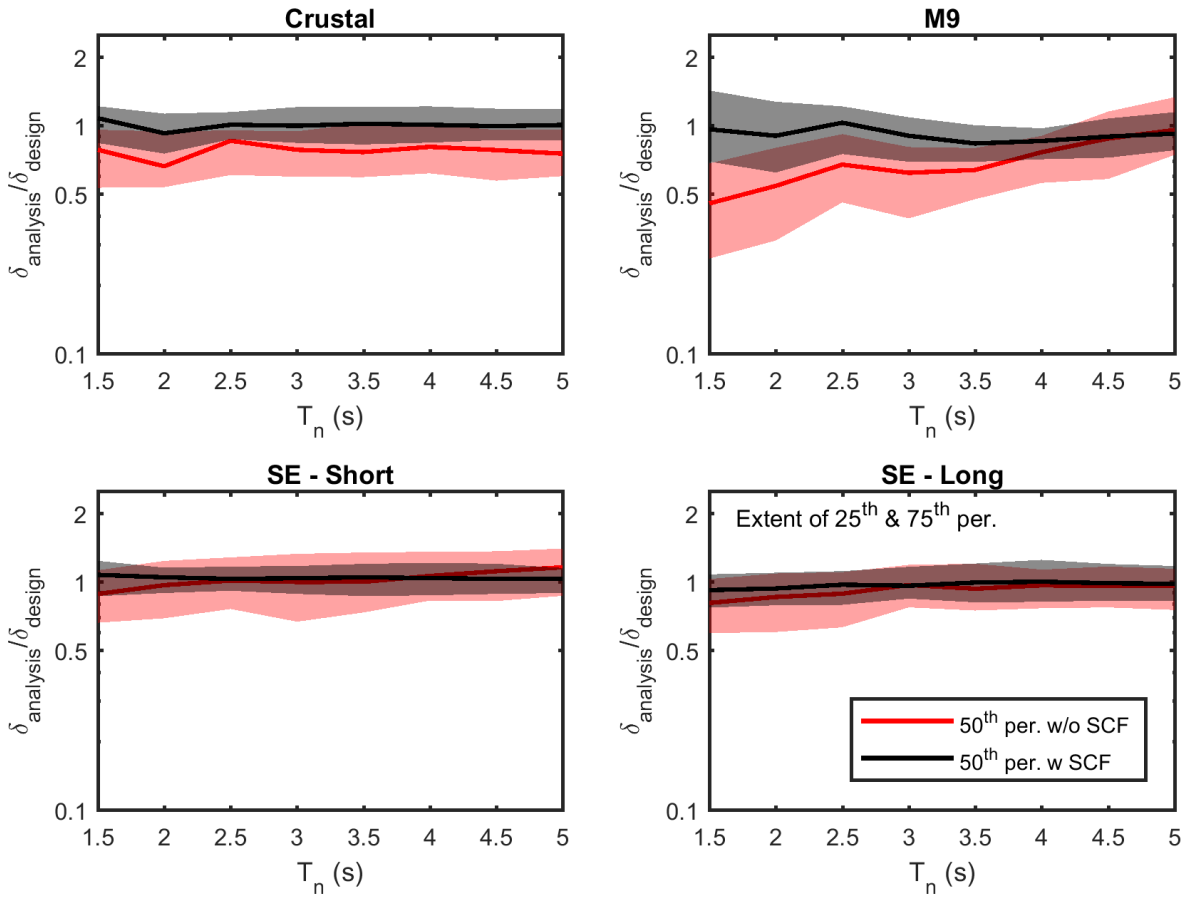

Figure C.18: Boxplot comparison before and after applying displacement-spectrum shape correction factor (α equals to 4) for Eurocode 8 (2004)

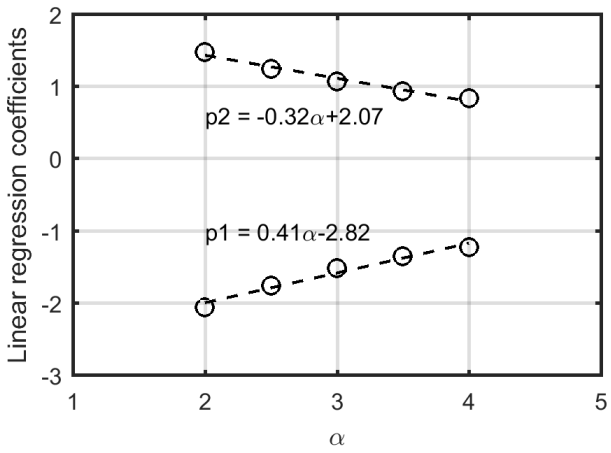

Figure C.19: Relationship between α and the linear regression coefficients for ASCE 7-16

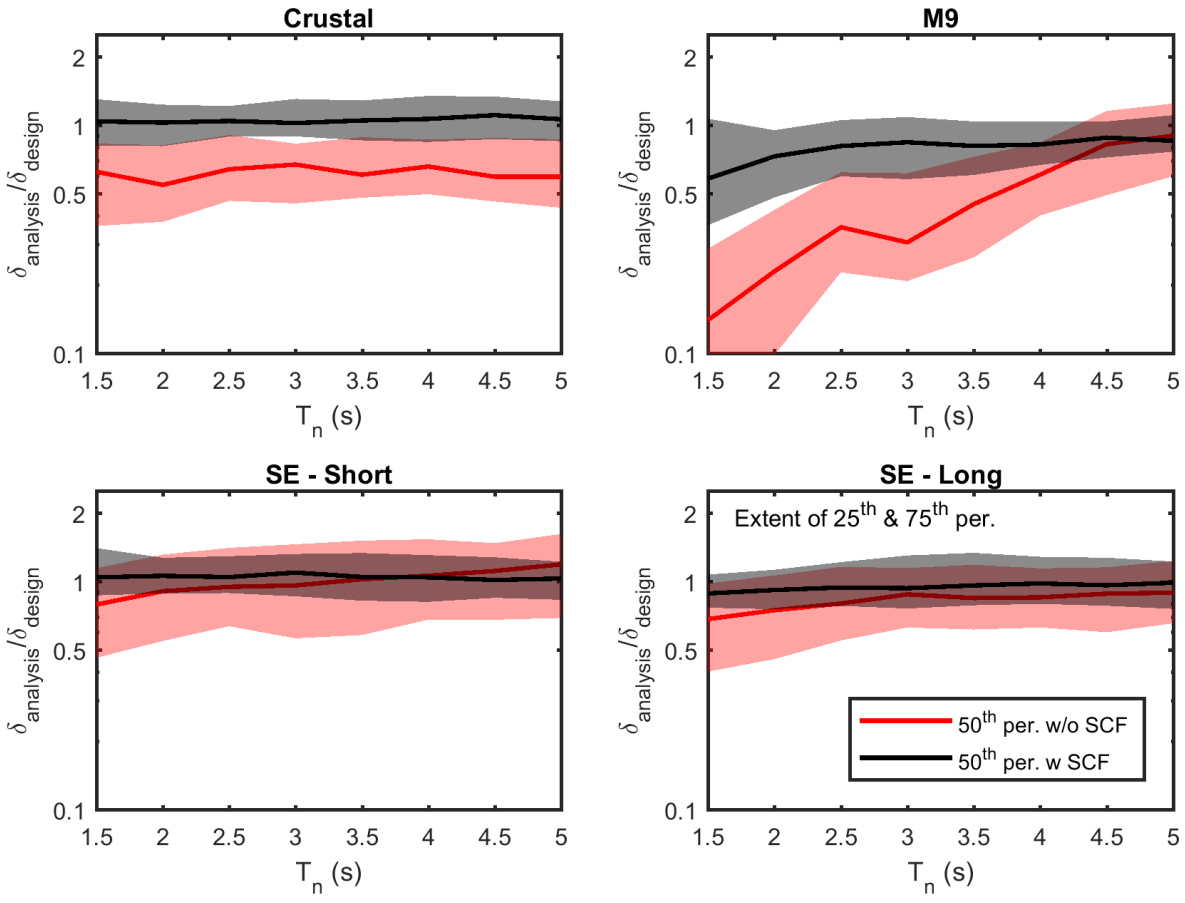

Figure C.20: Boxplot comparison before and after applying displacement-spectrum shape correction factor (α equals to 2) for ASCE 7-16

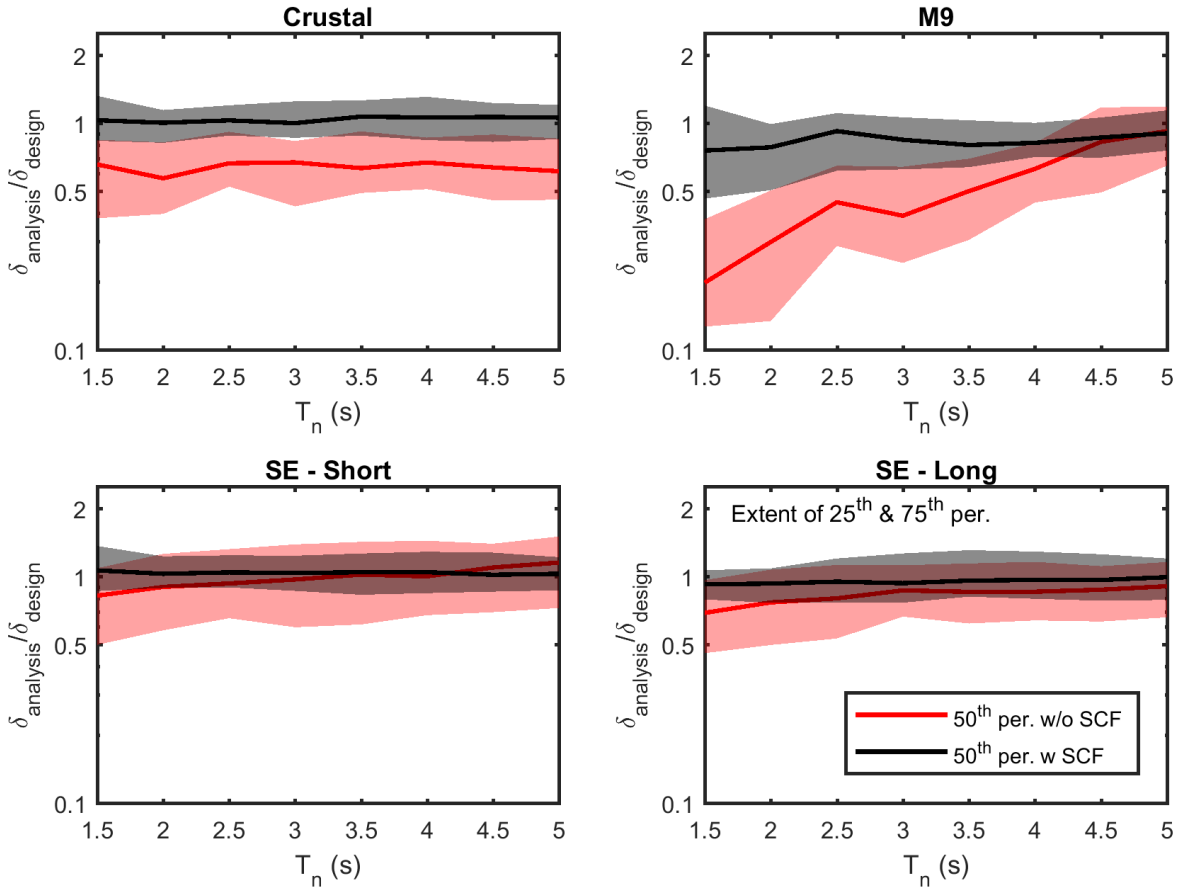

Figure C.21: Boxplot comparison before and after applying displacement-spectrum shape correction factor (α equals to 2.5) for ASCE 7-16

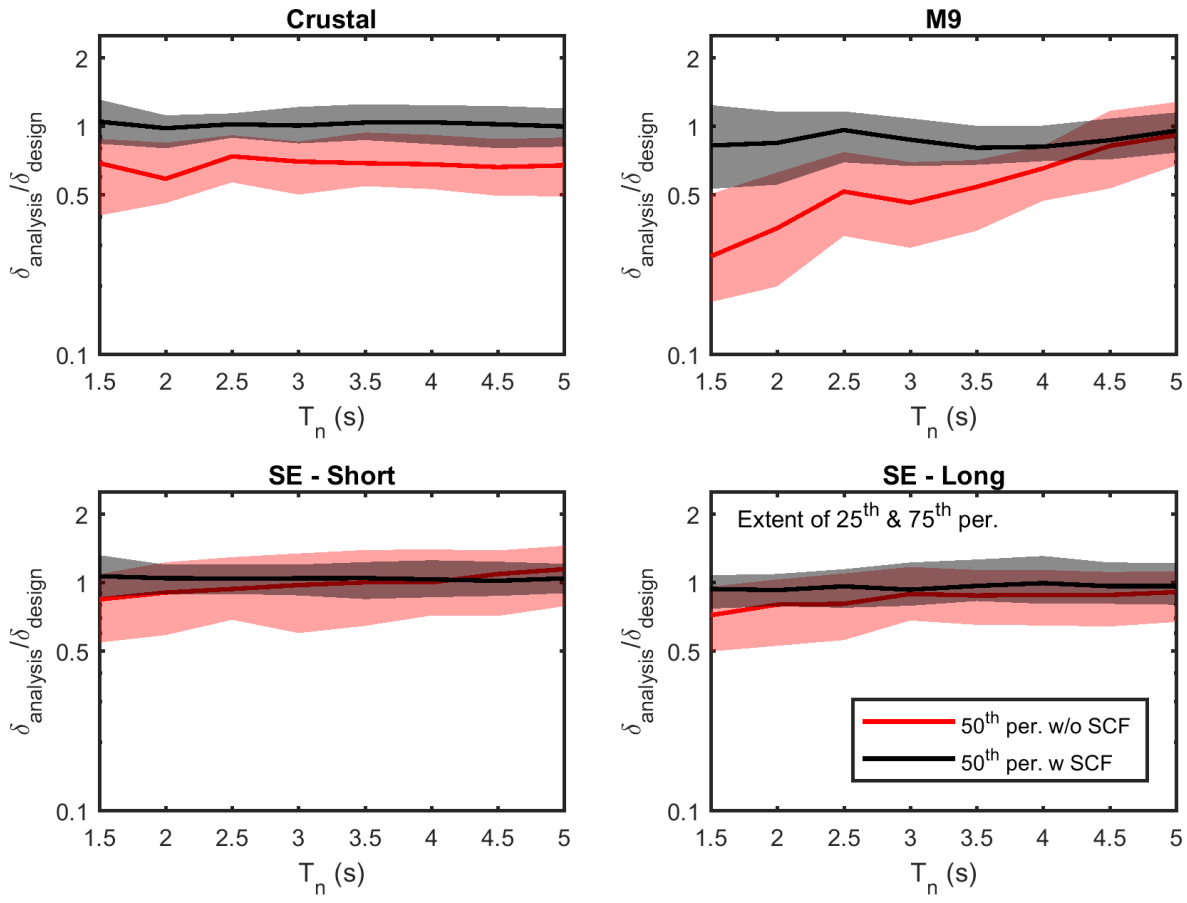

Figure C.22: Boxplot comparison before and after applying displacement-spectrum shape correction factor (α equals to 3) for ASCE 7-16

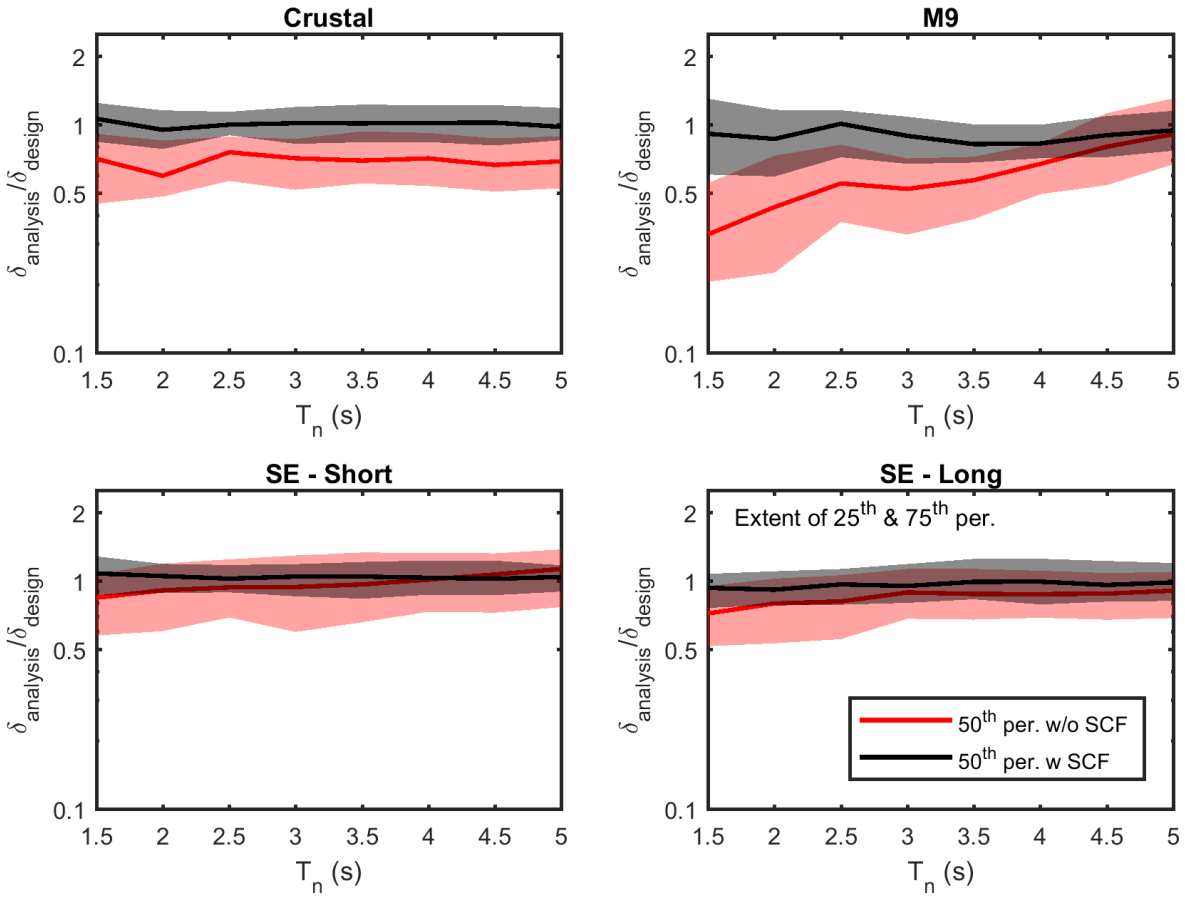

Figure C.23: Boxplot comparison before and after applying displacement-spectrum shape correction factor (α equals to 3.5) for ASCE 7-16

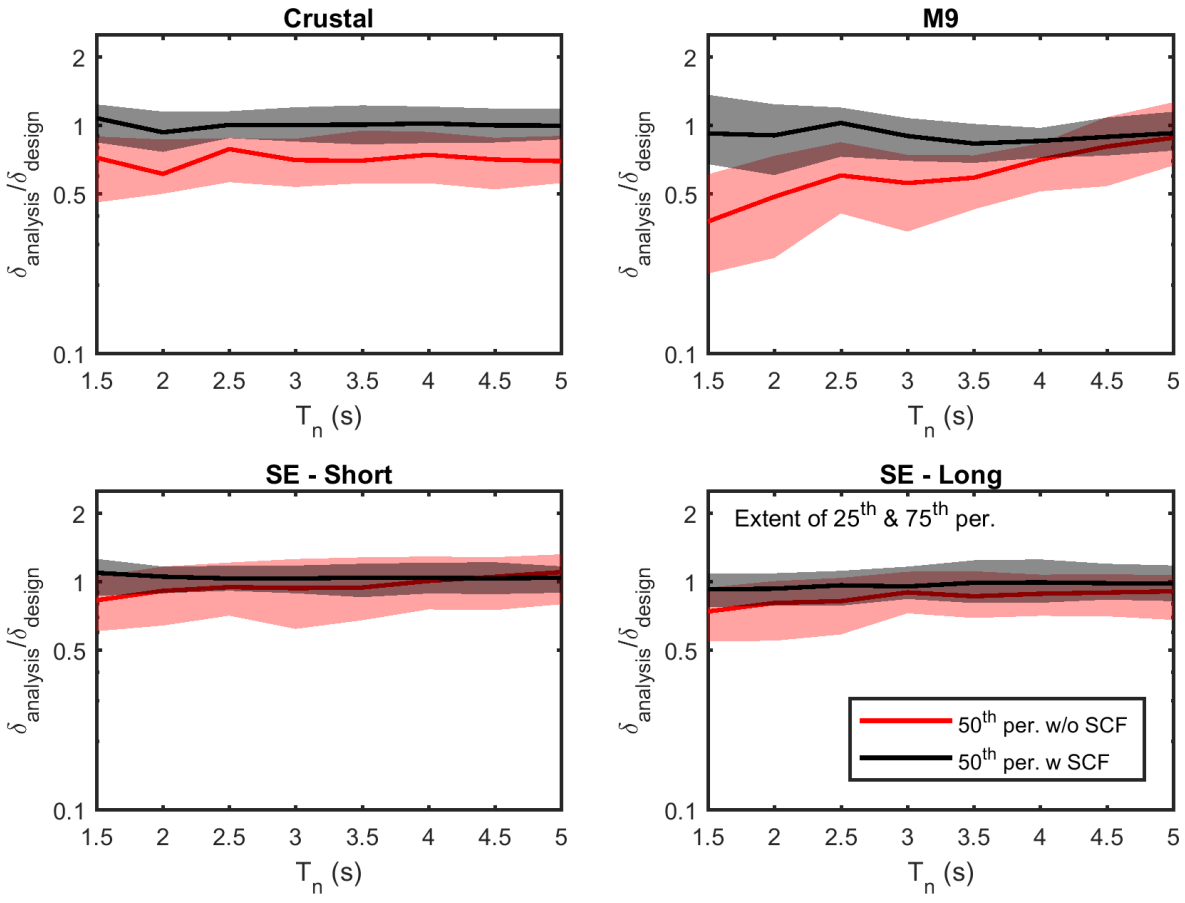

Figure C.24: Boxplot comparison before and after applying displacement-spectrum shape correction factor (α equals to 4) for ASCE 7-16

REFERENCES

318, A. C. (2014). *Building Code Requirements for Structural Concrete - ACI 318-14*. American Concrete Institute.

Ahmadi, G. (1983). "Stochastic earthquake response of structures on sliding foundation." *International Journal of Engineering Science*, 21(2).

Al-Hussaini, T. M., Constantinou, M. C., and Zayas, V. A. (1994). *Seismic isolation of multi-story frame structures using spherical sliding isolation systems*. National Center for earthquake engineering research.

Aragaw, L. F. (2017). "Floor response spectra in hybrid base-rocking and reinforced concrete wall buildings." M.S. thesis, University of Washington, University of Washington.

ASCE (2010). "Asce 7-10. minimum design loads for buildings and other structures.." American Society of Civil Engineers (ASCE). Reston, Virginia.

ASCE (2017). "Asce/sei 7-16: Minimum design loads and associated criteria for buildings and other structures.

Aslam, M., Scalise, D. T., and Godden, W. G. (1980). "Earthquake rocking response of rigid bodies." *J Struct Division*, 106(2), 377–392.

Aslani, H. and Miranda, E. (2005). "Probablistic earthquake loss estimation and loss disaggregation in buildings." *Report no.*, John A. Blume Earthquake Engineering Center, Stanford University, Palo Alto, CA. Report No. 157.

Atwater, B., Nelson, A., Clague, J., Carver, G. A., Yamaguchi, D. K., Bobrowsky, P. T., Bourgeois, J., Darienzo, M. E., Grant, W. C., Hemphill-Haley, E., Kelsey, H., Jacoby,

G. C., Nishenko, S., Palmer, S. P., Peterson, C. D., and Reinhart, M. A. (1995). "Summary of coastal geologic evidence for past great earthquakes at the cascadia subduction zone." *Earthquake Spectra*, 11(1), 1–18.

Bao, Y., Becker, T. C., and Hamaguchi, H. (2017). "Failure of double friction pendulum bearings under pulse-type motions." *Earthquake Engineering & Structural Dynamics*, 46(5), 715–732.

Barone, S., Calvi, G. M., and Pavese, A. (2019). "Experimental dynamic response of spherical friction-based isolation devices." *Journal of Earthquake Engineering*, 23(9), 1465–1484.

Becker, T. C., Bao, Y., and Mahin, S. A. (2017). "Extreme behavior in a triple friction pendulum isolated frame." *Earthquake Engineering & Structural Dynamics*, 46(15), 2683–2698.

Becker, T. C., Keldrauk, E. S., Mieler, M. W., Mahin, S. A., and Stojadinovic, B. (2012). "Effect of mass offset on the torsional response in friction pendulum isolated structures." *15th World Conference on Earthquake Engineering*, Lisbon, Portugal (September 24-28).

Becker, T. C. and Mahin, S. A. (2012). "Experimental and analytical study of the bi-directional behavior of the triple friction pendulum isolator." *Earthquake Engineering & Structural Dynamics*, 41(3), 355–373.

Becker, T. C. and Mahin, S. A. (2013a). "Approximating peak responses in seismically isolated buildings using generalized modal analysis." *Earthquake Engineering & Structural Dynamics*, 42(12), 1807–1825.

Becker, T. C. and Mahin, S. A. (2013b). "Correct treatment of rotation of sliding surfaces in a kinematic model of the triple friction pendulum bearing." *Earthquake Engineering & Structural Dynamics*, 42(2), 311–317.

Bergquist, S., Calvi, P. M., and Wiebe, R. (2019). "Introducing adaptive variable friction base isolation system." *12th Canadian Conference on Earthquake Engineering, June 17-20, 2019, Quebec, QC, Canada.*

Bommer, J. and Mendis, R. (2005). "Scaling of spectral displacement ordinates with damping ratios." *Earthquake Engineering and Structural Dynamics*, 34(2), 145–165.

Buckle, I. G. and Mayes, R. L. (1990). "Seismic isolation: history, application, and performance - a world view." *Earthquake Spectra*, 6(2), 161–201.

Calvi, P. M. and Calvi, G. M. (2018). "Historical development of friction-based seismic isolation systems." *Soil Dynamics and Earthquake Engineering*, 106, 14–30.

Calvi, P. M., Moratti, M., and Calvi, G. M. (2016a). "Seismic isolation devices based on sliding between surfaces with variable friction coefficient." *Earthquake Spectra*, 32(4), 2291–2315.

Calvi, P. M., Moratti, M., and Calvi, G. M. (2016b). "Seismic isolation devices based on sliding between surfaces with variable friction coefficient." *Earthquake Spectra*, 32(4), 2291–2315.

Calvi, P. M. and Ruggiero, D. M. (2016). "Numerical modelling of variable friction sliding base isolators." *Bulletin of Earthquake Engineering*, 14(2), 549–568.

Calvi, P. M. and Timsina, S. (2017). "Numerical study of the seismic behavior of variable friction base isolation systems." *LABSE Symposium. Vancouver: International Association for Bridge and Structural Engineering.*, 2196–2203.

Campbell, K. W. and Bozorgnia, Y. (2014). "Nga west2 ground motion model for the average horizontal components of pga, pgv, and 5 percent damped linear acceleration response spectra." *Earthquake Spectra*, 30(3), 1087–1115.

Cardone, D., Conte, N., Dall'Asta, A., Cesare, A. D., Flora, A., Lamarucciola, F., Micozzi, F., Ponzo, F. C., and Ragni, L. (2019). "Rintc e project: the seismic risk of existing italian rc buildings retrofitted with seismic isolation." *Seventh ECCOMAS Thematic Conference on Computational Methods in Structural Dynamics and Earthquake Engineering, Crete, Greece*.

Chandramohan, R., Baker, J. W., and Deierlein, G. G. (2016a). "Quantifying the influence of ground motion duration on structural collapse capacity using spectrally equivalent records." *Earthquake Spectra*, 32(2), 927–950.

Chandramohan, R., Baker, J. W., and Deierlein, G. G. (2016b). "Quantifying the influence of ground motion duration on structural collapse capacity using spectrally equivalent records." *Earthquake Spectra*, 32(2), 927–950.

Chang, S. W., Frankel, A. D., and Weaver, C. S. (2014). "Report on workshop to incorporate basin response in the design of tall buildings in the puget sound region, washington. u.s.." *Report no.*, Geological Survey, pen-File Report 2014-1196.

Constantinou, M. C., Gazetas, G., and Tadjbakhsh, I. (1984). "Stochastic seismic sliding of rigid mass supported through non-symmetric friction." *Earthquake Engineering & Structural Dynamics*, 12(6), 777–794.

Constantinou, M. C., Mokha, A., and Reinhorn, A. M. (1990). "Teflon bearings in base isolation. ii: modeling." *Jounral of Structural Engineering*, 116(2), 455–474.

Constantinou, M. C., Tsopelas, P., Kasalanati, A., and Wolff, E. (1999). "Property modification factors for seismic isolation bearings." *Report No. 99-0012*, MCEER.

Crandall, S. H., Lee, S. S., and Williams, J. H. (1974). "Accumulated slip of a friction-controlled mass excited by earthquake motions." *Journal of Applied Mechanics*, 41(4), 1094–1098.

Dao, N. D. (2012). "Seismis response of a full-scale 5-story steel frame building isolated by triple pendulum bearings under 3d excitation." Ph.D. thesis, University of Nevada, Reno, University of Nevada, Reno.

Dao, N. D. and Ryan, K. L. (2014). "Computational simulation of a full-scale, fixed-base, and isolated-base steel moment frame building tested at e-defense." *Journal of Structural Engineering*, 140(8).

Dao, N. D., Ryan, K. L., Sato, E., and Sasaki, T. (2013). "Predicting the displacement of triple pendulum bearings in afull-scale shaking experiment using a three-dimensional element." *Earthquake Engineering & Structural Dynamics*, 42(11), 1677–1695.

Derham, C. J., Kelly, J. M., and Thomas, A. G. (1985). "Nonlinear natural rubber bearings for seismic isolation." *Nuclear Engineering and Design*, 84(3), 417–428.

Dolce, M., Cardone, D., and Croatto, F. (2005). "Frictional behavior of steel-ptfe interfaces for seismic isolation." *Bulletin of Earthquake Engineering*, 3, 75–99.

EC8 (1994). "Design of structures for earthquake resistance eurocode 8.

EC8 (2004). "Design of structures for earthquake resistance eurocode 8.." Commision of the European Communities.

Erduran, E. (2012). "Evaluation of rayleigh damping and its influence on engineering demand parameter estimates." *Earthquake Engineering & Structural Dynamics*, 41(14), 1905–1919.

Fadi, F. and Constantinou, M. C. (2010). "Evaluation of simplified methods of analysis for structures with triple friction pendulum isolators." *Earthquake Engineering & Structural Dynamics*, 39(1), 5–22.

Fajardo, K. C. M. and Papageorgiou, A. S. (2016). "Residual slip of sliding blocks induced by near-fault ground motions." *Earthquake Engineering & Structural Dynamics*, 46(7), 1203–1220.

Faramarz, K. and Montazar, R. (2016). "Seismic response of double concave friction pendulum base-isolated structures considering vertical component of earthquake." *Advances in Structural Engineering*, 13(1), 1–13.

Fenz, D. M. and Constantinou, M. C. (2006). "Behaviour of the double concave friction pendulum bearing." *Earthquake Engineering & Structural Dynamics*, 35(11), 1403–1424.

Fenz, D. M. and Constantinou, M. C. (2008a). "Development, implementation, and verification of dynamic analysis models for multi-spherical sliding bearings." *Report No. 08-0018*, MCEER (August).

Fenz, D. M. and Constantinou, M. C. (2008b). "Modelling triple friction pendulum bearings for response-history analysis." *Earthquake Spectra*, 24(4), 1011–1028.

Fenz, D. M. and Constantinou, M. C. (2008c). "Spherical sliding isolation bearings with adaptive behavior: Experimental verification." *Earthquake Engineering & Structural Dynamics*, 37(2), 185–205.

Fenz, D. M. and Constantinou, M. C. (2008d). "Spherical sliding isolation bearings with adaptive behavior: Theory." *Earthquake Engineering & Structural Dynamics*, 37(2), 163–183.

Filiatrault, A., Uang, C.-M., Folz, B., Christopoulos, C., and Gatto, K. (2001). "Reconnaissance report of the February 28, 2001 Nisqually (Seattle-Olympia) Earthquake. Report No. SSRP–2001/02, Structural Systems Research Project, University of California, San Diego; 2001.

Flaccus, G. (2017). "Oregon city approves permit for us' 1st all-wood high-rise." *The Seattle Times*.

Frankel, A., Stephenson, W., and Carver, D. (2009). "Sedimentary basin effects in seattle washington: ground-motion observations and 3d simulations." *Bulletin of the Seismological Society of America*, 99(3), 1579–1611.

Frankel, A. D., Wirth, E. A., Marafi, N. A., MVidale, J., and Stephenson, W. (2018). "Broadband synthetic seismograms for magnitude 9 earthquakes on the cascadia megathrust based on a 3d simulations and stochastic synthetics, part 1: methodology and overall results." *Bulletin of the Seismological Society of America*, 108(5A), 2347–2369.

Furinghetti, M. and Pavese, A. (2019). "Assessment of the seismic response of isolated bridges under extra-stroke displacement demands." *41th IABSE Symposium, Guimaraes, Portugal*.

Furinghetti, M., Pavese, A., Quaglini, V., and Dubini, P. (2019). "Experimental investigation of the cyclic response of double curved surface sliders subjected to radial and bidirectional sliding motions." *Soil Dynamics and Earthquake Engineering*, 117, 190–202.

Furinghetti, M., Yang, T., Calvi, P. M., and Pavese, A. (2020). "Dynamic response of curved surface slider devices under severe input motion." *17th World Conference on Earthquake Engineering, 17WCEE, Sendai, Japan*.

Ganey, R. S. (2015). "Seismic design and testing of rocking CLT walls." M.S. thesis, University of Washington, University of Washington.

Garini, E. and Gazetas, G. (2013). "Damage potential of near-fault records: sliding displacement against conventional "intensity measures"." *Bulletin of Earthquake Engineering*, 11(2), 455–480.

Gazetas, G., Garini, E., Anastasopoulos, I., and Georgarakos, T. (2009). "Effect of near-fault ground shaking on sliding systems." *Journal of Geotechnical and Geoenvironmental Engineering*, 135(12), 1906–1921.

Girish, M. and Pranesh, M. (2013). "Sliding isolation systems: State-of-the-art review." *Journal of Mechanical and Civil Engineering*, 6(63), 30–35.

Goldfinger, C., Nelson, C. H., Morey, A. E., Johnson, J. E., Patton, J. R., Karabanov, E. B., Gutierrez-Pastor, J., Eriksson, A. T., Gracia, E., Dunhill, G., Enkin, R. J., Dallimore, A.,

and Vallier, T. (2012). "Turbidite event history - methods and implications for holocene paleoseismicity of the cascadia subduction zone." *Report 1661*, U.S. Geological Survey, Reston, VA, USA.

Graves, R. W., Pitarka, A., and Somerville, P. G. (1998). "Ground-motion amplification in the santa monica area: Effects of shallow basin-edge structure." *Bulletin of the Seismological Society of America*, 88(5), 1224–1242.

Greenwood, D. T. (1997). *Classical Dynamics*. DOVER PUBN INC.

Gupta, A. and Krawinkler, H. (1999). "Prediction of seismic ddemand for smrfs with ductile connections and elements." *Report no.*, SAC Background Document, Tech. Rep. SAC/BD-99/06.

Guyader, A. C. and Iwan, W. D. (2006). "Determining equivalent linear parameters for use in a capacity spectrum method of analysis." *Journal of Structural Engineering (ASCE)*, 132(1), 59–67.

Hall, J. F. (1999). "Discussion of 'the role of damping in seismic isolation'." *Earthquake Engineering & Structural Dynamics*, 28(12), 1717–1720.

Hall, J. F. (2006). "Problems encountered from the use (or misuse) of rayleigh damping." *Earthquake Engineering & Structural Dynamics*, 35(5), 525–545.

Hancock, J. and Bommer, J. J. (2007). "Using spectral matched records to explore the influence of strong-motion duration on inelastic structural response." *Soil Dynamics and Earthquake Engineering*, 27(4), 291–299.

Henry, R. S., Brooke, N. J., Sritharan, S., and Ingham, J. M. (2012). "Defining concrete compressive strain in unbonded post-tensioned walls." *ACI Struct J 2012*.

Housner, G. W. (1963). "The behavior of inverted pendulum structures during earthquakes. Bull Seismol Soc Am 1963;53:403–417.

Iemura, H., Igarashai, A., and Takahashi, Y. (1999). "Substructured hybrid techniques for actuator loading and shake table tests." *First international conference on advances in structural engineering and mechanics, Seoul, South Korea*.

Jangid, R. S. (2008). "Stochastic response of bridges seismically isolated by friction pendulum system." *Journal of Bridge Engieering*, 13(4), 319–330.

Jangid, R. S. (2015). "Computational numerical models for seismic response of structures isolated by sliding systems." *The Journal of the International Association for Structural Control and Monitoring*, 12(1), 117–137.

Jankowski, R. (2005). "Non-linear viscoelastic modelling of earthquake-induced structural pounding." *Earthquake Engineering and Structural Dynamics*, 34, 595–611.

Jankowski, R. (2006). "Analytical experession between the impact damping ratio and the coefficient of restitution in the non-linear viscoelastic model of structural pounding." *Earthquake Engineering and Structural Dynamics*, 35, 517–524.

Jankowski, R. (2010). "Experimental study on earthquake-induced pounding between structural elements made of different building materials." *Earthquake Engineering and Structural Dynamics*, 39, 343–354.

K-NET and KIK-net (1996). "K-net and kik-net strong-motion seismograph networks, <http://www.kyoshin.bosai.go.jp/>.

Kawashima, K., MacRae, G. A., ichi Hoshikuma, J., and Nagaya, K. (1998). "Residual displacement response spectrum." *Journal of Structural Engineering*, 124(5), 523–530.

Kelly, J. M. (1986). "Asiesmic base isolation: review and bibliography." *Soil Dynamics and Earthquake Engineering*, 5(4), 202–216.

Kelly, J. M. (1999). "The role of damping in seismic isolation." *Earthquake Engineering & Structural Dynamics*, 28(1), 3–20.

Khoshnoudian, F. and T., A. H. (2014). "Impact of structures with double concave friction pendulum bearings on adjacent structures." *Structure and Buildings*, 167(SB1), 41–53.

Kim, Y.-S. and Yun, C.-B. (2007). "Seismic response characteristics of bridges using double concave friction pendulum bearings with tri-linear behavior." *Engineering Structures*, 29(11), 3082–3093.

Kircher, C. A. and Lashkari, B. (1989). "Statistical evaluation of nonlinear response of seismic isolation systems." *Report No. JBA 109-070*, Jack R. Benjamin and Associates, Inc., Mountain View, CA, USA.

Komodromos, P., Polycarpou, P. C., Papaloizou, L., and Phocas, M. C. (2007). "Repsonse of seismically isolated buildings considering poundings." *Earthquake Engineering and Structural Dynamics*, 36, 1605–1622.

Kumar, M., Whittaker, A. S., and Constantinou, M. C. (2015). "Characterizing friction in sliding isolation bearings." *Earthquake Engineering and Structural Dynamics*, 44(9), 1409–1425.

Kurama, Y., Pessiki, S., Sause, R., and Lu, L. W. (1999). "Seismic behavior and design of unbonded post-tensioned precast concrete walls." *PCI J 1999*.

Landi, L., Grazi, G., and Diotallevi, P. P. (2015). "Comparison of different models for friction pendulum isolators in structures subjected to horizontal and vertical ground motions." *Soil Dynamics and Earthquake Engineering*, 81, 75–83.

Lee, D. and Constantinou, M. C. (2016). "Quintuple friction pendulum isolator: behavior, modelling, and validation." *Earthquake Spectra*, 32(3), 1607–1626.

Lin, Y. Y. and Chang, K. C. (2003). "Study on damping reduction factor for buildings under earthquake ground motions." *Journal of Structural Engineering*, 129(2), 206–214.

Lin, Y. Y. and Chang, K. C. (2004). "Effects of site classes on damping reduction factors." *Journal of Structural Engineering*, 130(11), 1667–1675.

Macrae, G. A. and Kawashima, K. (1997). "Post-earthquake residual displacements of bilinear oscillators." *Earthquake Engineering & Structural Dynamics*, 26(7), 701–716.

Malekzadeh, M. and Taghikhany, T. (2010). "behavior behavior of double concave friction pendulum bearing and its advantages over friction pendulum systems." *Transaction A: Civil Engineering*, 17(2), 81–88.

Malhotra, P. (1997). "pounding of seismic impacts in base-isolated buildings." *Earthquake Engineering and Structural Dynamics*, 26, 797–813.

Marafi, N. A., Berman, J. W., and Eberhard, M. O. (2016). "Ductility-dependent intensity measure that accounts for ground-motion spectral shape and duration." *Earthquake Engineering & Structural Dynamics*, 45(4), 653–672.

Marafi, N. A., Eberhard, M. O., Berman, J. W., Wirth, E. A., and Frankel, A. (2019). "Impacts of m9 cascadia subduction zone earthquake on idealized systems." *Earthquake Spectra*, 35(3), 1261–1287.

Marafi, N. A., Eberhard, M. O., Berman, J. W., Wirth, E. A., and Frankel, A. D. (2017). "Effects of deep basins on structural collapse during large subduction earthquakes." *Earthquake Spectra*, 33(3), 963–997.

Masroor, A. and Mosqueda, G. (2012). "Experimental simulation of base-isolated buildings pounding against moat wall and effects on superstructure response." *Earthquake Engineering and Structural Dynamics*, 41(14), 2093–2109.

MATLAB (2017). *version 7.10.0 (R2010a)*. The MathWorks Inc., Natick, Massachusetts.

Mazza, F. and Mazza, M. (2017). "Sensitivity to modelling and design of curved surface

sliding bearings in the nonlinear seismic analysis of base-isolated r.c. framed buildings." *Soil Dynamics and Earthquake Engineering*, 79, 951–970.

McCrum, D. and Williams, M. (2016). "An overview of seismic hybrid testing of engineering structures." *Engineering Structures*, 118, 240–261.

McKenna, F. (1997). "Object-oriented finite element programming: Frameworks for analysis, algorithms and parallel computing." Ph.D. thesis, University of California, Berkeley, University of California, Berkeley.

Miranda, E. and Ruiz-Garcia, J. (2002). "Evaluation of approximate methods to estimate maximum inelastic displacement demands." *Earthquake Engineering and Structural Dynamics*, 31(3), 539–560.

Mokha, A., Constantinou, M. C., and Reinhorn, A. M. (1988). "Teflon bearings in aseismic base isolation: experimental studies and machematical modeling." *Report no.*, NCEER-88-0038, Buffalo, N.Y.

Mollaioli, F., Lucchini, A., Cheng, Y., and Monti, G. (2013). "Intensity meansures for the seismic response prediction of base-isolated buildings." *Bulletin of Earthquake Engineering*, 11(5), 1841–1866.

Morgan, T. A. and Mahin, S. A. (2008). "The optimization of multi-stage friction pendulum isolators for loss mitigation considering a range of seismic hazard." *The 14th World Conference on Earthquake Engineering*, Beijing, China (Octobor).

Morgan, T. A. and Mahin, S. A. (2010). "Achieving reliable seismic performance enhancement using multi-stage friction pendulum isolators." *Earthquake Engineering & Structural Dynamics*, 39(13), 1443–1461.

Morgan, T. A. and Mahin, S. A. (2011). "The use of base isolation systems to achieve complex seismic performance objectives." *Report no.*, Pacific Earthquake Engineering Research Center, College of Engineering, Univeristy of California Berkeley (July).

Mosqueda, G., Whittaker, A. S., and Fenves, G. L. (2004). "Characterization and modelling of friction pendulum bearings subjected to multiple components of excitation." *Jounral of Structural Engineering*, 130(3), 433–442.

Murnal, P. and Sinha, R. (2004). "Aseismic design of structure-equipment systems using variable frequency pendulum isolator." *Nuclear Engineering and Design*, 231(2), 129–139.

Muthukumar, S. and DesRoches, R. (2006). "A hertz contact model with non-linear damping for pounding simulation." *Earthquake Engineering and Structural Dynamics*, 35(7), 811–828.

Naeim, F. and Kelly, J. M. (1999). *Design of seismic isolated structures*. John Wiley & Sons, INC. New York, USA.

NEHRP (2015). "Nehrp recommended seismic provisions for new buildings and other structures. 2015 edition." National Earthquake Hazards Reduction Program - NEHRP.

Nikfar, F. and Konstantinidis, D. (2017). "Effect of the stick-slip phenomenon on the sliding response of objects subjected to pulse excitation." *Jounral of Engineering Mechanics*, 143(4).

Palermo, A., Pampanin, S., and Buchanan, A. H. (2006). "Experimental investigations on LVL seismic resistant wall and frame subassemblies." *First European Conference on Earthquake Engineering and Seismology* (01).

Panchal, V. R. and Jangid, R. S. (2008a). "Seismic behavior of variable frequency pendulum isolator." *Earthquake Engineering and Engineering Vibration*, 7(2), 193–205.

Panchal, V. R. and Jangid, R. S. (2008b). "Variable friction pendulum system for seismic isolation of liquid storage tanks." *Nuclear Engineering and Design*, 238(6), 1304–1315.

Panchal, V. R., Jangid, R. S., Soni, D. P., and Mistry, B. B. (2010). "Reponse of the

double variable frequency pendulum isolator under triaxial ground excitations." *Journal of Earthquake Engineering*, 14(4), 527–558.

Pant, D. R., Wijeyewickrema, A. C., and ElGawady, M. A. (2013). "Appropriate viscous damping for nonlinear time-history analysis of base-isolated reinforced concrete buildings." *Earthquake Engineering & Structural Dynamics*, 42(15), 2321–2339.

Pavese, A., Furinghetti, M., and Casarotti, C. (2018). "Experimental assessment of the cyclic response of friction-based isolators under bidirectional motions.." *Soil Dynamics and Earthquake Engineering*, 114, 1–11.

Pavlou, E. A. and Constantinou, M. C. (2004). "Response of elastic and inelastic structures with damping systems to near-field and soft-soil ground motions." *Engineering Structures*, 26(9), 1217–1230.

PEER (2010). "Pacific earthquake engineering research center, next generation attenuation (nga) - west2, <https://peer.berkeley.edu/research/nga-west-2>.

Pei, S., van de Lindt, J., Barbosa, A., Berman, J. W., McDonnell, E., Dolan, J. D., Blomgren, H., Zimmerman, R. B., Huang, D., and Wichman, S. (2018). "Experimental seismic response of a resilient two-story mass timber building with post-tensioned rocking walls." *J Struct Eng*.

Peloso, S., Pavese, A., and Casarotti, C. (2012). "Eucentre trees lab: Laboratory for training and research in earthquake engineering and seismology." *Geotechnical, Geological and Earthquake Engineering*, 20, 65–81.

Perez, F. J., Pessiki, S., Sause, R., and Lu, L. W. (2003). "Lateral load tests of unbonded post-tensioned precast concrete walls." *ACI Special Publication 2003*.

Petrini, L., Maggi, C., Priestley, M. J. N., and Calvi, G. M. (2008). "Experimental verification of viscous damping modeling for inelastic time history analyzes." *Journal of Earthquake Engineering*, 12(sup1), 125–145.

Petti, L., Polichetti, F., Lodato, A., and Palazzo, B. (2013). "Modelling and analysis of base isolated structures with friction pendulum system considering near fault events." *Open Journal of Civil Engineering*, 3(2), 86–93.

Ponzo, F. C., Cesare, A. D., Leccese, G., and Nigro, D. (2017). "Shake table testing on restoring capability of double concave friction pendulum seismic isolation systems." *Earthquake Engineering & Structural Dynamics*, 46(14), 2337–2353.

Ponzo, F. C., Cesare, A. D., Nigro, D., Simonetti, M., and Leccese, G. (2014). "Shaking table tests of a base isolated structure with double concave friction pendulums." *NZSEE Conference*, Aotea Centre, Auckland (March 21-23).

Priestley, M. J. N. (1998). "Displacement based approaches to rational limit states design of new structures." *Proceedings of the 11th European Conference on Earthquake Engineering, Paris.*

Priestley, M. J. N., Calvi, G. M., and Kowalsky, M. J. (2007). *Displacement based seismic design of structures.* IUSS Press, Pavia, Italy.

Ramallo, J., Johnson, E. A., and Spencer, B. (2002). "Smart base isolation systems." *Journal of Engineering Mechanics*, 128(10), 1088–1099.

Reinhorn, A. M., Sivaselvan, M. V., Liang, Z., and Shao, X. (2004). "Real-time dynamic hybrid testing of structural systems." *13th World Conference on Earthquake Engineering, Vancouver, B.C., Canada.*

Roussis, P. C. and Constantinou, M. C. (2006a). "Experimental and analytical studies of structures seismically isolated with an uplift-restraining friction pendulum bearing system." *Earthquake Engineering & Structural Dynamics*, 35(5), 595–611.

Roussis, P. C. and Constantinou, M. C. (2006b). "Uisolator-restraining friction pendulum seismic isolation system." *Earthquake Engineering & Structural Dynamics*, 35(5), 577–593.

Ryan, K. L. and Dao, N. D. (2016). "Influence of vertical ground shaking on horizontal response of seismically isolated buildings with friction bearings." *Journal of Structural Engineering*, 142(1).

Ryan, K. L., Dao, N. D., Sato, E., Sasaki, T., and Okazaki, T. (2012). "Aspects of isolation device behavior observed from full-scale testing of an isolated building at e-defense." *20th Analysis & Computation Specialty Conference*, Chicago, Illinois, USA (March 29-31).

Ryan, K. L. and Polanco, J. (2008). "Problems with rayleigh damping in base-isolated buildings." *Journal of Structural Engineering*, 134(11), 1780–1784.

Sarlis, A. A. and Constantinou, M. C. (2016). "A model of triple friction pendulum bearing for general geometric and frfriction parameters." *Earthquake Engineering & Structural Dynamics*, 45(11), 1837–1853.

Schellenberg, A. (2014). "Single friction pendulum bearing element, <http://opensees.berkeley.edu/wiki/>.

Simo, J. and Hughes, T. (1998). *Computational Inelasticity*. Springer, New York.

Smyrous, E., Priestley, M. J. N., and Carr, A. J. (2011). "Modeling of elastic damping in non-linear time-history analyses of catilever rc walls." *Bulletin of Earthquake Engineering*, 9(5), 1559–1578.

Somerville, P., Anderson, D., Sun, J., Punyamurthula, S., and Smith, N. (1998). "Generation of ground motion time histories for performance-based seismic engineering." *Proceedings of the Sixth National Earthquake Engineering Conference, Seattle, WA*.

Soni, D. P., Mistry, B. B., and Panchal, V. R. (2016). "Seismic isolation of bridges with double variable frequency pendulum isolator." *Advances in Structural Engineering*, 15(2), 185–203.

Stephenson, W. J., Reitman, N. G., and Angster, S. J. (2017). "P- and s-wave velocity models incorporating the cascadia subduction zone for 3d earthquake ground motion simulations." *Report 2017-1152*, U.S. Geological Survey, Reston, VA, USA.

Taniguchi, T. (2002). "Non-linear response analyses of rectangular rigid bodies subjected to horizontal and vertical ground motion." *Earthq Eng & Struct Dyn*, 31(8), 1481–1500.

Taniguchi, T. and Miwa, T. (2006). "A simple procedure to approximate slip displacement of freestanding rigid body subjected to earthquake motions." *Earthquake Engineering & Structural Dynamics*, 36(4), 481–501.

Taylor, A. W., Lin, A. N., and Martin, J. W. (1992). "Performance of elastomers in isolation bearings: a literature review." *Earthquake Spectra*, 8(2), 279–303.

Timsina, S. and Calvi, P. M. (2018). "Damping properties of variable friction base isolation systems." *16th European Conference of Earthquake ENgineering.*, Thessaloniki, Greece.

Tsai, C., Lin, Y. C., and Su, H. C. (2010). "Characterization and modeling of multiple friction pendulum isolation system with numerous sliding interfaces." *Earthquake Engineering & Structural Dynamics*, 39(13), 1463–1491.

Tsai, C. S., Chiang, T.-C., and Chen, B.-J. (2003a). "Seismic behavior of mfps isolated structure under near-fault sources and strong ground motions with long predominent periods." *ASME Pressure Vessels and Piping Conference*, Cleveland Ohio, USA (July 20-24).

Tsai, C. S., Chiang, T.-C., and Chen, B.-J. (2003b). "Shaking table tests of a full scale steel structure isolated with mfps." *ASME Pressure Vessels and Piping Conference*, Cleveland Ohio, USA (July 20-24).

Tsai, C. S., Chiang, T.-C., and Chen, B.-J. (2004). "Experimental study for multiple friction pendulum system." *13th World Conference on Earthquake Engineering*, Vancouver B.C., Canada (August 1-6).

Tsopelas, P., Constantinou, M. C., Kircher, C. A., and Whitaker, A. S. (1997). "Evaluation of simplified methods of analysis for yielding structures." *Report No. NCEER 97-0012*, National Center for Earthquake Engineering Research, University at Buffalo, State University of New York, Buffalo, NY, USA.

Twigden, K. M., Henry, R. S., and Ma, Q. T. (2012). "Dynamic testing of post-tensioned rocking walls." *Proceedings of the 15th World Conference on Earthquake Struct*, Department of Civil and Environmental Engineering, University of Auckland, New Zealand.

USGS (2018). "National seismic hazard mapping project (nshmp) code." United States Geological Survey (USGS), <https://github.com/usgs/nshmp-haz>.

Warn, G. P. and Ryan, K. L. (2012). "A review of seismic isolation for buildings: Historical development and research needs." *Buildings*, 2(3), 300 – 325.

Welch, D. P. (2016). "Non-structural element considerations for contemporary performance-based earthquake engineering." Ph.D. thesis, University of Pavia, University of Pavia.

Wichman, S. (2018). "Large-scale dynamic testing of rocking cross laminated timber walls." M.S. thesis, University of Washington, Seattle, WA, University of Washington, Seattle, WA.

Winters, C. W. and Constantinou, M. C. (1993). "Evaluation of static and response spectrum analysis procedures of seaoc/ubc for seismic isolated structures." *Report No. NCEER 93-0004*, National Center for Earthquake Engineering Research, University at Buffalo, State University of New York, Buffalo, NY, USA.

Yang, T., Calvi, P., and Wiebe, R. (2019a). "Numerical implementation of variable friction sliding base isolators and preliminary experimental results." *Earthquake Spectra*.

Yang, T., Marafi, N. A., Calvi, P. M., Wiebe, R., Eberhard, M. O., and Berman, J. W. (2019b). "Impact of simulated m9 cascadia subduction zone motions on base isolated structures." *Twelfth Canadian Conference on Earthquake Engineering. Quebec, QC.*

Yang, T., Marafi, N. A., Calvi, P. M., Wiebe, R., Eberhard, M. O., and Berman, J. W. (2020). "Accounting for spectral shape in simplified method of analyzing friction pendulum system." *Engineering Structures, under review.*

Yang, T., Ozcamur, U., Calvi, P. M., Wiebe, R., Bruschi, E., Quaglini, V., Sucuoglu, H., Lanese, L., and Pavese, A. (2019c). "Experimental investigation of the behavior of variable friction base isolation system." *Seventh ECCOMAS Thematic Conference on Computational Method in Structural Dynamics and Earthquake Engineering. Crete, Greece.*

Zayas, V. A., Low, S., and Mahin, S. A. (1987). "The fps earthquake resistant system." *Report No. UCB/EERC-87/01*, UC Berkeley.